Jordan Journal of Mechanical and Industrial Engineering (JJMIE)

JJMIE is a high-quality scientific journal devoted to fields of Mechanical and Industrial Engineering. It is published by The Jordanian Ministry of Higher Education and Scientific Research in corporation with the Hashemite University.

SUBMISSION ADDRESS:

Prof. **Mousa S. Mohsen**, Editor-in-Chief
Jordan Journal of Mechanical & Industrial Engineering,
Hashemite University,
PO Box 330127, Zarqa, 13133 , Jordan

E-mail: jjmie@hu.edu.jo

Hashemite Kingdom of Jordan

Hashemite University

Jordan Journal of Mechanical and Industrial Engineering

JJMIE

An International Peer-Reviewed Scientific Journal

http://jjmie.hu.edu.jo/

ISSN 1995-6665

Jordan Journal of Mechanical and Industrial Engineering (JJMIE)

JJMIE is a high-quality scientific journal devoted to fields of Mechanical and Industrial Engineering. It is published by The Jordanian Ministry of Higher Education and Scientific Research in corporation with the Hashemite University.

Intruduction: The Editorial Board is very committed to build the Journal as one of the leading international journals in mechanical and industrial engineering sciences in the next few years. With the support of the Ministry of Higher Education and Scientific Research and Jordanian Universities, it is expected that a heavy resource to be channeled into the Journal to establish its international reputation. The Journal's reputation will be enhanced from arrangements with several organizers of international conferences in publishing selected best papers of the conference proceedings.

Aims and Scope: Jordan Journal of Mechanical and Industrial Engineering (JJMIE) is a refereed international journal to be of interest and use to all those concerned with research in various fields of, or closely related to, mechanical and industrial engineering disciplines. Jordan Journal of Mechanical and Industrial Engineering aims to provide a highly readable and valuable addition to the literature which will serve as an indispensable reference tool for years to come. The coverage of the journal includes all new theoretical and experimental findings in the fields of mechanical and industrial engineering or any closely related fields. The journal also encourages the submission of critical review articles covering advances in recent research of such fields as well as technical notes.

Guide for Authors

Manuscript Submission

High-quality submissions to this new journal are welcome now and manuscripts may be either submitted online or mail.

Online: For online submission upload one copy of the full paper including graphics and all figures at the online submission site, accessed via E-mail: jjmie@hu.edu.jo. The manuscript must be written in MS Word Format. All correspondence, including notification of the Editor's decision and requests for revision, takes place by e-mail and via the Author's homepage, removing the need for a hard-copy paper trail.

By Mail: Manuscripts (1 original and 3 copies) accompanied by a covering letter may be sent to the Editor-in-Chief. However, a copy of the original manuscript, including original figures, and the electronic files should be sent to the Editor-in-Chief. Authors should also submit electronic files on disk (one disk for text material and a separate disk for graphics), retaining a backup copy for reference and safety.

Note that contributions may be either submitted online or sent by mail. Please do NOT submit via both routes. This will cause confusion and may lead to delay in article publication. Online submission is preferred.

Submission address and contact:

Prof. **Mousa S. Mohsen**, Editor-in-Chief
Jordan Journal of Mechanical & Industrial Engineering,
Hashemite University,
PO Box 330127, Zarqa, 13115 , Jordan
E-mail: jjmie@hu.edu.jo

Types of contributions: Original research papers

Corresponding author: Clearly indicate who is responsible for correspondence at all stages of refereeing and publication, including post-publication. Ensure that telephone and fax numbers (with country and area code) are provided in addition to the e-mail address and the complete postal address. Full postal addresses must be given for all co-authors.

Original material: Submission of an article implies that the work described has not been published previously (except in the form of an abstract or as part of a published lecture or academic thesis), that it is not under consideration for publication elsewhere, that its publication is approved by all authors and that, if accepted, it will not be published elsewhere in the same form, in English or in any other language, without the written consent of the Publisher. Authors found to be deliberately contravening the submission guidelines on originality and exclusivity shall not be considered for future publication in this journal.

Supplying Final Accepted Text on Disk: If online submission is not possible: Once the paper has been accepted by the editor, an electronic version of the text should be submitted together with the final hardcopy of the manuscript. The electronic version must match the hardcopy exactly. We accept MS Word format only. Always keep a backup copy of the electronic file for reference and safety. Label the disk with your name. Electronic files can be stored on CD.

Notification: Authors will be notified of the acceptance of their paper by the editor. The Publisher will also send a notification of receipt of the paper in production.

Copyright: All authors must sign the Transfer of Copyright agreement before the article can be published. This transfer agreement enables Jordan Journal of Mechanical and Industrial Engineering to protect the copyrighted material for the authors, but does not relinquish the authors' proprietary rights. The copyright transfer covers the exclusive rights to reproduce and distribute the article, including reprints, photographic reproductions, microfilm or any other reproductions of similar nature and translations.

PDF Proofs: One set of page proofs in PDF format will be sent by e-mail to the corresponding author, to be checked for typesetting/editing. The corrections should be returned within 48 hours. No changes in, or additions to, the accepted (and subsequently edited) manuscript will be allowed at this stage. Proofreading is solely the author's responsibility. Any queries should be answered in full. Please correct factual errors only, or errors introduced by typesetting. Please note that once your paper has been proofed we publish the identical paper online as in print.

Author Benefits

Page charge: Publication in this journal is free of charge.
Free off-prints: Three journal issues of which the article appears in along with twenty-five off-prints will be supplied free of charge to the corresponding author. Corresponding authors will be given the choice to buy extra off-prints before printing of the article.

Manuscript Preparation:

General: Editors reserve the right to adjust style to certain standards of uniformity. Original manuscripts are discarded after publication unless the Publisher is asked to return original material after use. If online submission is not possible, an electronic copy of the manuscript on disk should accompany the final accepted hardcopy version. Please use MS Word for the text of your manuscript.

Structure: Follow this order when typing manuscripts: Title, Authors, Affiliations, Abstract, Keywords, Introduction, Main text, Conclusions, Acknowledgements, Appendix, References, Figure Captions, Figures and then Tables. For submission in hardcopy, do not import figures into the text - see Illustrations. For online submission, please supply figures imported into the text AND also separately as original graphics files. Collate acknowledgements in a separate section at the end of the article and do not include them on the title page, as a footnote to the title or otherwise.

Text Layout: Use double spacing and wide (3 cm) margins. Ensure that each new paragraph is clearly indicated. Present tables and figure legends on separate pages at the end of the manuscript. If possible, consult a recent issue of the journal to become familiar with layout and conventions. All footnotes (except for table and corresponding author footnotes) should be identified with superscript Arabic numbers. To conserve space, authors are requested to mark the less important parts of the paper (such as records of experimental results) for printing in smaller type. For long papers (more that 4000 words) sections which could be deleted without destroying either the sense or the continuity of the paper should be indicated as a guide for the editor. Nomenclature should conform to that most frequently used in the scientific field concerned. Number all pages consecutively; use 12 or 10 pt font size and standard fonts. If submitting in hardcopy, print the entire manuscript on one side of the paper only.

Corresponding author: Clearly indicate who is responsible for correspondence at all stages of refereeing and publication, including post-publication. The corresponding author should be identified with an asterisk and footnote. Ensure that telephone and fax numbers (with country and area code) are provided in addition to the e-mail address and the complete postal address. Full postal addresses must be given for all co-authors. Please consult a recent journal paper for style if possible.

Abstract: A self-contained abstract outlining in a single paragraph the aims, scope and conclusions of the paper must be supplied.

Keywords: Immediately after the abstract, provide a maximum of six keywords (avoid, for example, 'and', 'of'). Be sparing with abbreviations: only abbreviations firmly established in the field may be eligible.

Symbols: All Greek letters and unusual symbols should be identified by name in the margin, the first time they are used.

Units: Follow internationally accepted rules and conventions: use the international system of units (SI). If other quantities are mentioned, give their equivalent in SI.

Maths: Number consecutively any equations that have to be displayed separately from the text (if referred to explicitly in the text).

References: All publications cited in the text should be presented in a list of references following the text of the manuscript.

Text: Indicate references by number(s) in square brackets in line with the text. The actual authors can be referred to, but the reference number(s) must always be given.

List: Number the references (numbers in square brackets) in the list in the order in which they appear in the text.

Examples:

Reference to a journal publication:

[1] M.S. Mohsen, B.A. Akash, “Evaluation of domestic solar water heating system in Jordan using analytic hierarchy process”. Energy Conversion & Management, Vol. 38, No. 9, 1997, 1815-1822.

Reference to a book:

[2] Strunk Jr W, White EB. The elements of style. 3rd ed. New York: Macmillan; 1979.

Reference to a conference proceeding:

[3] B. Akash, S. Odeh, S. Nijmeh, “Modeling of solar-assisted double-tube evaporator heat pump system under local climate conditions”. 5th Jordanian International Mechanical Engineering Conference, Amman, Jordan, 2004.

Reference to a chapter in an edited book:

[4] Mettam GR, Adams LB. How to prepare an electronic version of your article. In: Jones BS, Smith RZ, editors. Introduction to the electronic age, New York: E-Publishing Inc; 1999, p. 281-304

Free Online Color: If, together with your accepted article, you submit usable color and black/white figures then the journal will ensure that these figures will appear in color on the journal website electronic version.

Tables: Tables should be numbered consecutively and given suitable captions and each table should begin on a new page. No vertical rules should be used. Tables should not unnecessarily duplicate results presented elsewhere in the manuscript (for example, in graphs). Footnotes to tables should be typed below the table and should be referred to by superscript lowercase letters.

JJMIE
Jordan Journal of Mechanical and Industrial Engineering

JJMIE

Volume 1, Number 2, Dec. 2007
ISSN 1995-6665
Pages 69 - 77

Jordan Journal of Mechanical and Industrial Engineering

Effects of Condensate and Initial Formation of Thin Frost Layer on Evaporator Coil Performance of Room Air-Conditioners

Ahmed Hamza H. Ali *, Ibrahim M. Ismail

Department of Mechanical Engineering, Faculty of Engineering, Assiut University, Assiut 71516, Egypt.

Abstract

This study investigated experimentally and theoretically, how condensate and initial formation of a thin frost layer on the surface of the evaporator affects the evaporator performance of room air-conditioners compared to dry coil conditions. The theoretically obtained results were validated with the measured values in both wet and initial frost formation conditions and a good correlation was found. The results indicated that, at the same range of change in face velocity value, the total conductivity of a dry coil $(UA)_{dry}$ is increased by 38.8%. However, when it is combined with an increase in latent heat to the evaporator total cooling capacity ratio value (Q_{lat}/Q) of 10.6%, the total conductivity of wet coil $(UA)_{wet}$ is 45.4%. These results clearly indicate that the evaporator coil is characterized by higher performance under wet conditions compared to dry coil conditions. The results also show that the total conductivity after initial formation of a thin frost layer $(UA)_{Fr}$ has a higher value by about 8.2% than the dry coil condition. Moreover, the degradation in the evaporator coil performance under thin frost with a thickness up to one mm is only about 6.7%.

Keywords: Evaporator coil performance; Wet evaporator coil; Frosted evaporator coil; and Air dehumidifying;

Nomenclature

Alphabetic Symbols

A	: surface area, m^2
a'	: coefficient for fictitious enthalpy, J/kg
b'	: slope of i vs. T curve [31], J/kg K
c_p	: specific heat, J/kg K
d_o	: evaporator tube outer diameter, m
h	: heat transfer coefficient, $W/m^2 K$
i	: enthalpy, J/kg
k	: thermal conductivity, W/m K
L	: length, m
Le	: Lewis number, -
m	: fin perimeter, m^{-1}
$\dot{m}$	: mass flow rate, kg/s
q	: heat flux, W/m^2
Q	: total heat transfer rate, W
r	: radius, m
T	: temperature, K or ^oC
U	: overall heat transfer coefficient, $W/m^2.K$ or {$[W/m^2.K]/[J/kg]$}
V	: face velocity, m/s
W	: humidity ratio, $kg_{H2O}/kg_{dry\ air}$
x, y, z	: spatial co-ordinates, m

Greek symbols

ΔT_m	: logarithmic mean temperature difference, K
δ	: thickness, m
ϕ	: relative humidity
η	: fin efficiency, -

Subscripts

a	: air
avg	: average
c	: convection
cl	: cell
eff	: effective
eq	: equivalent
f	: saturated liquid
fin	: fin or fins
fr	: frost
g	: saturated vapor
I	: inner
in	: inlet
lat	: latent heat
m	: mean
o	: outer
out	: outlet
p	: pipe
r	: refrigerant

* Corresponding author. e-mail: ah-hamza@aun.edu.eg

s : saturation
sv : solid-vapor in sublimation
v : vapor
w : wet
wat : water
wb : wet-bulb

1. Introduction

The evaporator coils in air conditioning appliances provide the coldest surface for condensate formation from the air stream water vapor content in cooling operation mode as it cools and dehumidifies indoor air. As the amount of water condensed on the evaporator surface increases, water droplets are formed and intermittently drain due to gravity. Some water droplets adhere to the coil by surface tension phenomena. This is defined as hold-up condensate water. This hold-up water reacts with other indoor airborne contaminants and produces mold compounds and fouling resistance between the room air and the evaporator coil surface, Ali and Ismail [1]. Meanwhile, thin frost layer formation may occur on the evaporator surfaces of a room air-conditioner when it works as a heat pump in winter season. In this case, the outdoor air temperature is low and the evaporator operates at coil surface temperatures below 0^{o}C. It is found that some dust deposits on the outdoor heat exchanger of the air-conditioner, which sticks on the evaporator surface during the heating season with either condensate or an initial frost formation layer. Both compounds of water/dust depositions on the evaporator coil surface form a resistance to the heat transfer. Ali and Ismail [1] presented the effect of fouling deposits on room air-conditioner performance. In the literature, numerous studies have been conducted and provide detailed information relevant to both heat and mass transfer coefficients in the airside of fin and tube heat exchangers under dehumidifying conditions such as Yaun and Tucker [2], Jacobi et al. [3], Pirompugd et al. [4] and Halici and Taymaz [5]. Gravity-independent water separation within the condensing heat exchangers by the use of a hydrophilic fin surface coating, that promote the wetting and wicking of the condensate on the fin, were investigated by Shin et al. [6] and O'Neill et al. [7], while Lee et al. [8] investigated this effect in case of frost formation. Wetter [9] presented a simple simulation model of a dry finned water-to-air coil. Osada [10] reported that in the evaporator condensed water adheres to the fin surface and thus increases the pressure drop of the evaporator and degrades the heat transfer performance of the fins owing to louver blockage and water bridging. In addition, numerous studies have been conducted by using simulation models of thick frost layer formation and predicted the performance of fin and tube evaporator under these conditions such as [11 to 16]. The influence of thick frost formation on the performance of evaporator coils were investigated by either simulation or experimental studies by [17 to 23].

However, through a literature survey it was found that numerous experiments and models investigated the effect of water vapor condensate on the airside of evaporator surfaces mainly focused on the evaluation of both heat and mass transfer coefficients. Few examples cited that the condensate degrades the heat transfer performance of the evaporator coil fins as well as causes a decrease in the airflow area, thus leading to an increase of pressure drop through the evaporator coil. Ali and Ismail [1] found in their experiments that the clean wet-coil performance is higher than the dry-coil condition. Numerous studies investigated the influence of a thick frost formation layer on the evaporator coil, while the influence of initiation and thin frost layer formation on the evaporator coil performance is not clear. Thus, the performance of an evaporator coil of room air-conditioners, when its surface is covered by either condensate or initial frost layers without dust deposition on the coil, need to be clarified. Therefore, for room air-conditioners, this study aims at investigating experimentally and theoretically the effect of condensate and thin frost layer formation on the surface of evaporator coil on the performance of the evaporator coil compared to dry coil surface conditions. Experiments were carried out on a flat finned and staggered tube evaporator coil, while the theoretical model was used to clarify the effect of parameters on the evaporator coil performance which is difficult to measure experimentally.

2. Experimental Apparatus, Instrumentation and Procedure

2.1. Apparatus and Measurements

The test facility described in Ali and Ismail [1] is used to investigate the performance of the evaporator coil under wet and initial formation of thin frost layer conditions at various airflow rates with minor modifications in case of frost experiments. The modifications are: increasing the capillary tube length, and cooling the last 8 tubes in the condenser by water. A schematic diagram of the apparatus and its dimensions is shown in Figure 1.

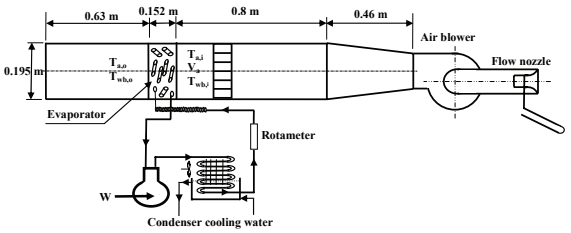

Figure 1: A schematic diagram of the test facility

The apparatus mainly consists of an air handling section, test section and the appropriately equipped instruments. The air handling sections include a nozzle meter, a variable speed airflow fan, an inlet air distribution plenum and a flow straightener (honeycomb). The flow straightener provides a uniform air velocity distribution at the inlet to the evaporator coil (test section). The evaporator coil frontal fined area dimensions are 0.254 x 0.191 m (10x7.5in) with a depth in flow direction of 0.152 m (6 in). It is a plate fin and tubes heat exchanger. The fins are made from aluminum alloy and the tubes are made from copper. Four rows of tubes with four tubes in depth are arranged in staggered manner ($2d_o$ x $2.5d_o$). The tubes are of 19.2 mm (3/4in) in outer diameter (d_o), fins pitch is fin/4.2mm (6 fin/in) and fin thickness is 0.6 mm. The test coil (evaporator) itself is a component of a compression refrigeration cycle using R12 as refrigerant, see Figure 1. The other main components of the refrigeration cycle include a hermetic compressor, an air-cooled condenser, a rotameter (uncertainty of ±0.01 l/min) for refrigerant mass flow measurements, 2 m long capillary tube for refrigerant

expansion, and 4 pressure gauges at inlet and outlet of both the evaporator and condenser with uncertainty of ±0.05 kPa. The input electric power to the compressor was measured by a Wattmeter with uncertainty of ±5W.

A variable electric resistor controlled the input power to the airflow fan motor. Thus, the airflow rate is controlled by the fan speed. The throat velocity of the air passing through the nozzle is determined by measuring the static pressure drop across the nozzle using water manometer with an accuracy of ±0.5 mm.

A data acquisition system having a resolution of 0.1°C is used to measure and record the temperatures. All temperatures are measured by using type T (copper/constantan) thermocouples with 0.5 mm diameter and an uncertainty of ±0.5 C. The thermocouples were used to measure the temperature at the following locations: 12 points air dry-bulb and wet-bulb temperatures before the evaporator coil, 6 points on the evaporator coil tubes and fins in addition, two points at refrigerant inlet and outlet, two points for ambient air dry-bulb and wet-bulb temperatures, respectively. The face air velocity at air inlet to the evaporator was measured using a portable digital anemometer with uncertainty of ±0.01 m/s.

2.2. Experimental Procedures and Data Reduction

To study the effect of dew formation on the performance, experiments were carried out in a quasi-steady state condition at different airflow rates corresponding to a face velocity ranging from 0.612 m/s to 5 m/s respectively. While for the case of initial formation of a thin frost layer, the face velocity was 0.612 m/s. This is because with this experimental apparatus and operating conditions, the frost is formed only at this low face velocity value. Stabilization of temperature readings to ± 0.1 °C in all thermocouple sensors was considered an indication of reaching a quasi-steady state condition, then the average of the temperature values are read and recorded. At the same time, the readings of the refrigeration cycle pressure gauges and rotameter as well as the manometer readings for the pressure difference across the nozzle were taken. The measurements were performed at the Heat Laboratory, Assiut University, Egypt. The experimental evaporator coil cooling capacity Q has been obtained from the energy balance on both refrigerant and air sides. It is given by:

$$Q=(Q_a+Q_r)/2 \qquad [W] \qquad (1)$$

where Q_a is the airside capacity of the evaporator coil. It is calculated by:

$$Q_a = \dot{m}_a(i_{a,1} - i_{a,2}) \qquad [W] \qquad (2)$$

where the air enthalpy, *i*, at the inlet and outlet of the evaporator coil is calculated by the formula of ASHRAE [24]. The air mass flow rate, $\dot{m}_a$, at the nozzle throat is calculated from the pressure drop across the nozzle. Q_r is the refrigerant side cooling capacity of the evaporator coil. It is calculated by:

$$Q_r = \dot{m}_r(i_{r,o} - i_{r,i}) \qquad [W] \qquad (3)$$

where the refrigerant enthalpy, *i*, at the inlet and outlet of the evaporator coil is obtained from [25] as a function of the temperature and pressure of state point. The refrigerant mass flow rate $\dot{m}_r$ is estimated from the rotameter reading and the refrigerant density. ASHRAE [24] relations were used to obtain the humid air properties ratio, W, at inlet and outlet of the evaporator coil from the measured data of air dry-bulb temperature, T_a, and air wet-bulb temperature, T_{wb}, respectively. The uncertainties were calculated through the data reduction of the experimental measurements based on the formula for computing overall errors of [26]; the uncertainty is estimated in determination Q ranging from 9.5% to 13.6%.

3. Thermal Model

The thermal model is used to investigate the factors influencing the evaporator coil performance, which are hardly to obtain by experimental measurements. These factors are the ratio of wet coil area to the total coil surface area, the ratio of the latent heat or sublimation heat capacities to the evaporator total cooling capacity and the effect of initial formation of thin frost layer thickness on the evaporator performance. The model is built for a flat fin air-to-refrigerant heat exchanger (evaporator coil) with staggered tubes shown in (Fig. 2-a). It is based on the discretization of the heat exchanger into cells. Each cell is one finned-tube in the refrigerant flow direction z as shown in Fig. (2-b).

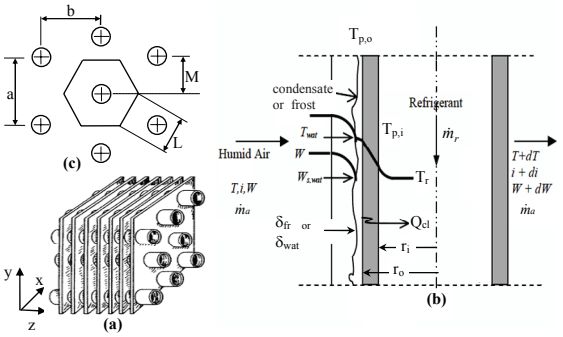

Figure 2: Schematic diagram of flat staggered fin-and tube evaporator coil with coordinate (a), energy and mass transfer balance on a cell (b) and hexagonal fin dimension parameters (c)

The refrigerant enters the evaporator as a two-phase mixture of saturated liquid and vapor with specific quality. Therefore, the energy variation is assumed to be one-dimensional in the flow direction and it is estimated from the enthalpy difference of the refrigerant between inlet and outlet from a cell. In contrast, the air dry-bulb temperature and its humidity ratio are varying in both x and y directions over each cell. Figure (2-b) shows a cell in the general case at which the surface could be dry, wet or with a thin frost layer at the cell surface. In the following subsections, modeling of the coil under these conditions is presented.

3.1. Dry Coil Surface Condition

For dry coil surface conditions, it is assumed that neither condensate nor frost is present on a cell surface shown in Fig. (2-b). The heat transfer rate for a cell, Q_{cl}, is obtained as follows: convection heat transfer from the air stream to the pipe outer surface and fins is sensible only and is calculated by:

$$Q_{cl} = h_{c,o}(A_{p,o} + \eta A_{fin})(T - T_{p,o}) \quad [W] \quad (4)$$

where $h_{c,o}$ is the outside convective heat transfer coefficient between air and dry surfaces of the cell. It is calculated from the correlation of a flat fin-and-tube heat exchanger of Wang [27]. $A_{p,o}$ and A_{fin} are the pipe outer surface areas and fin area in a cell, respectively. T is the air stream dry-bulb temperature, $T_{p,o}$ is the pipe outer surface temperature and η is the fin efficiency and is given by ASHRAE [24] in case of staggered tubes with continuous flat fins. In this study, η is treated as hexagonal fin as shown in Fig. (2-c) and given by:

$$\eta = \frac{\tanh(mr_o\varphi)}{mr_o\varphi} \quad (5)$$

where

$$m = \sqrt{\frac{2h_{c,o}}{k_{fin}\delta_{fin}}},$$

$$\varphi = \left(\frac{r_{eq}}{r_o} - 1\right)\left[1 + 0.35\ln\left(\frac{r_{eq}}{r_o}\right)\right]$$

$$\frac{r_{eq}}{r_o} = 1.27\left(\frac{M}{r_o}\right)\left[\left(\frac{L}{M} - 0.3\right)\right]^{0.5}$$

where r_o is the inner radius of the fin, the pipe outer radius, see Fig. (2-b), r_{eq} is the equivalent radius of the fin, k_{fin} is the fin thermal conductivity, δ_{fin} is the fin thickness and a, b, L and M are dimension parameters as shown in Figure (2-c), respectively. The conduction through the pipe wall for one cell is given by:

$$Q_{cl} = \frac{2\pi L_p k_p (T_{p,o} - T_{p,i})}{\ln\left(r_o / r_i\right)} \quad [W] \quad (6)$$

where k_p, $T_{p,o}$ and $T_{p,i}$ are the pipe thermal conductivity, outer and inner surface temperatures, respectively. Convection from inner tube surface to the refrigerant for a cell is given by:

$$Q_{cl} = h_i A_{p,i}(T_{p,i} - T_r) \quad [W] \quad (7)$$

where h_i is the convective-evaporation heat transfer coefficient between the two-phase refrigerant and the inner surface of the pipe. It is a function of the two-phase refrigerant mass flow rate, refrigerant quality, pressure, temperature and internal pipe dimensions. Throughout the literature, only a few methods explained the details for calculating the local values of h_i such as [28] and [29]. In this study, the value of h_i is calculated by the techniques presented in Corberán [30]. T_r is the refrigerant temperature. From Eqs. (4), (6) and (7) the value of Q_{cl} can be also expressed by:

$$Q_{cl} = U_o A_o \Delta T_m \quad [W] \quad (8)$$

where U_o is given by:

$$U_o = \frac{1}{\frac{A_o}{A_{P,i}h_i} + \frac{A_o \ln\left(r_o / r_i\right)}{2\pi k_p L_p} + \frac{A_o}{\eta A_{fin} h_{c,o}} + \frac{A_o}{A_{P,o}h_{c,o}}}$$

$$[W/m^2.K] \quad (9)$$

The logarithmic mean temperature difference, ΔT_m, between the air stream and refrigerant with the probability of refrigerant superheating at the outlet from the pipe at the last cell is given by:

$$\Delta T_m = \frac{(T_{a,in} - T_{r,out}) - (T_{a,out} - T_{r,in})}{ln\left[\frac{(T_{a,in} - T_{r,out})}{(T_{a,out} - T_{r,in})}\right]} \quad [K] \quad (10)$$

3.2. Wet Coil Surface Condition

As the moist air is cooled and its temperature decreases below the water vapor dew point temperature, the water vapor condenses on the evaporator coil surface. For wet coil conditions, both the heat transfer and mass transfer between the moist air and a thin condensate film takes place simultaneously according to the enthalpy difference as cited in [31]. In this part of the model the following assumption are used: the outer surface of fins and tubes are covered with a thin water film, the boundary layer of saturated moist air is at the thin water film temperature, which is equal to both the tube and modified fins surface temperature. The equation for convection heat and mass transfer between humid air and wet cell surfaces, shown in Fig. (2-b), is given by [31] as follows:

$$Q_{cl} = \frac{h_{c,o}A_o}{c_{p_a}}\left[(i - i_{s,wat}) + \frac{(W - W_{s,wat})(i_{g,T} - i_{f,wat} - i_g^0 Le)}{Le}\right]$$

$$[W] \quad (11)$$

with total outer surface area of the cell A_o, enthalpy i, humidity ratio W, specific heat c_p and Lewis number Le. To consider the conduction across the water film thickness shown in Fig. (2-b), conduction through the pipe wall and internal convection evaporation between the refrigerant and inner pipe surface Q_{cl} value is calculated by;

$$Q_{cl} = U_{o,w} A_o \Delta i_m \quad [W] \quad (12)$$

where $U_{o,w}$ is the overall heat transfer coefficient in wet condition based on the enthalpy potential. It is given by:

$$U_{o,w} = \frac{1}{\frac{b'_r A_o}{A_{p,i}h_i} + \frac{b'_p A_o \, ln\left(r_o / r_i\right)}{2\pi k_p L_p} + \frac{b'_{wat} A_o}{A_{fin}\eta_w h_{o,w}} + \frac{b'_{wat} A_o}{A_{p,o}h_{o,w}}}$$

$$[(W/m2)/(J/kg)] \quad (13)$$

where $b_r^{'} = \frac{i_{s,p} - i_{s,r}}{T_p - T_r}$, $i_{s,p}$ and $i_{s,r}$ are fictitious enthalpies of saturated moist air valuated at the pipe and refrigerant temperatures, respectively. The value of $i_{s,p}$ is defined in [31] by $i_{s,p} = a_{wat}^{'} + b_{wat}^{'} T_p$, where $a^{'}$ and $b^{'}$ are coefficients to be calculated from plots in [31] at the air saturation condition corresponding to the pipe temperature. Similarly the values of $i_{s,r}$, $b_p^{'}$ and $b_{wat}^{'}$ can be calculated, respectively. The wet fin efficiency, η_w, is calculated at $h_{o,w}$. The combined convection and evaporation heat transfer coefficient, $h_{o,w}$, between moist air and outer cell surfaces area is calculated by:

$$h_{o,w} = \frac{1}{\frac{cp_a}{b_{wat}^{'} h_{c,o}} + \frac{\delta_{wat}}{k_{wat}}} \qquad [W/m^2.K] \qquad (14)$$

Δi_m value is calculated by:

$$\Delta i_m = \frac{\left(i_1 - i_{s,r,2}\right) - \left(i_2 - i_{s,r,1}\right)}{ln\frac{\left(i_1 - i_{s,r,2}\right)}{\left(i_2 - i_{s,r,1}\right)}} \qquad [J/kg]$$

where i_1 and i_2 are enthalpies of the entering and leaving air stream of a cell, $i_{s,r,1}$ and $i_{s,r,2}$ are fictitious enthalpies of saturated air calculated at entering and leaving refrigerant temperatures of a cell and are estimated as defined in [31] . The pipe inner surface temperature is calculated from:

$$T_{p,i} = T_r + \frac{Q_{cl}}{h_i A_{p,i}} \qquad [K] \qquad (15)$$

The total heat transferred from the air stream to the cell surface consists of two parts: the sensible part and the latent part. Using the relation of convective heat and convective mass transfer by Le number relation, the outer pipe surface temperature is compared with the inlet air dew point temperature to the cell in order to clarify at which cell the condensate begins. It is calculated by:

$$Q_{cl} = h_{c,o}\left[1 + \frac{\left(W - W_{s,p}\right)\ i_{fg}}{Le\ \ c_{p_a}(T - T_{p,o})}\right](T - T_{p,o})(A_{p,o} + \eta A_{fin}) \qquad [W] \qquad (16)$$

where i_{fg} is the enthalpy for latent heat of condensation.

3.3. Frost Coil Surface Condition

In this part of the model, a correlation that considers the molecular diffusion of water vapor inside an initially formed frost layer, mass and heat transfer between air stream and frosted coil surface is used to predict the effect of an initial formation of a thin frost layer on the evaporator coil surface and the thin frost thickness effect on the evaporator performance. The following assumptions are considered: all heat and mass transfer surfaces are covered with thin frost layer and this layer is to be characterized by average properties; frost thermal conductivity varies only with frost density.

The total heat transfer rate in a cell with frosted surface conditions is calculated by:

$$Q_{cl} = U_{o,fr} A_o \Delta T_m \qquad [W] \qquad (17)$$

where $U_{o,fr}$ is given by:

$$U_{o,fr} = \frac{1}{\frac{A_o}{A_{P,i} h_i} + \frac{A_o\, ln\left(r_o / r_i\right)}{2\pi k_p L_p} + \frac{\delta_{fr}}{k_{fr}} + \frac{A_o}{\eta A_{fin} h_{eff}} + \frac{A_o}{A_{P,o} h_{eff}}} \qquad [W/m^2.K] \qquad (18)$$

k_{fr} and δ_{fr} are the frost thermal conductivity and thickness, respectively. The equations presented in [19] for k_{fr} and δ_{fr} are used in this study. h_{eff} is effective combined sensible/ sublimation heat transfer coefficient. By similarity with eq. (16) it is calculated by:

$$h_{eff} = h_{c,o}\left[1 + \frac{\left(W - W_{s,fr}\right)\ i_{sv}}{Le\ \ c_{p_a}\left(T - T_{fr,o}\right)}\right] \qquad [W/m^2.K] \qquad (19)$$

where i_{sv} is the enthalpy for heat of sublimation and $T_{fr,o}$ is the frost layer surface temperature which is calculated by:

$$T_{fr} = \frac{Q_{cl}}{h_{eff} A_o} - T \qquad [K] \qquad (20)$$

3.4. Solution Techniques

The inlet conditions for both the air and refrigerant are input into the model. The solution method of the equation in general is based on an iterative solution procedure for pipe temperatures. First, a guess is made for pipe temperature distribution in each cell, and then the governing equations for the refrigerant are solved in an explicit manner. Once the refrigerant properties are obtained for any fluid cell, the pipe temperatures at every pipe cell are estimated from the heat transferred across it. This procedure is repeated until convergence is reached. In the airside, depending on the operating condition parameters, some cells may operate with a dry surface, and with remainder of its wet surface. Detailed procedures for the solution of humid air are in ARI [32] and can be summarized as follows: the evaporator is first treated as dry, then the inlet dew point temperature of the air is compared with the wall temperature of cells. From the heat transfer rate equation the outlet enthalpy is calculated, and then the outlet air temperature. At cells where the pipe wall temperature is equal to the inlet air dew point temperature of the cell, the calculation for a wet coil is integrated. Then, the latent heat portion is calculated as the difference between the total heat and the sensible heat. From the latent heat portion, the outlet humidity values from the cells are calculated. The evaporator coil

dimensions described in the experimental section with the aid of the equations for calculation of A_o and A_{fin}, which are given in ARI [32], are input into the model. The mean hold-up water thickness, δ_{wat} , remaining on the evaporator surfaces and the frost thickness δ_{fr} are set to 0.1 mm in case of investigating other parameters than their thickness. The Lewis number (Le) is set to 1. A computer program based on this model was written in FORTRAN language. In the program, air properties are calculated with using ASHRAE [24] equations and refrigerant properties are calculated by using subroutine PROPERTY of ASHRAE [25].

4. Results and Discussion

4.1. Effect of Condensate on Evaporator Coil Performance

The results presented in this study are based on a quasi-steady state condition. Among many measurements that were carried out for face velocities ranging from 0.612 m/s to 5 m/s, it was observed experimentally that there is no condensate for experiments performed at face velocities greater than 1 m/s. Therefore, there was a significant contact time required between moist air and the evaporator coil surface for dew formation. In addition to this factor, the lower air relative humidity as seen from Figure (3-a) inside the laboratory during the experiments time, is anther factor contributing to this effect. However, in order to investigate the effect of condensate formation on the evaporator coil performance, all experiments were carried out with inlet refrigerant temperature higher than 0 °C, to avoid frost formation on the coil surface. The measured values of variation of inlet air dry-bulb temperature entering the evaporator coil, refrigerant inlet temperature to evaporator coil as well as the determined air water continent humidity ratio and relative humidity both were calculated from the measured wet-bulb and dry-bulb temperatures at various air face velocity as shown in Figure (3-a). The calculated values of outlet air dry-bulb temperature, air water continent humidity ratio and the evaporator coil total cooling capacity, from the input operating conditions data to the model that is shown in Figure (3-a), are compared with their corresponding experimentally determined values as shown in Figures (3-b,c and d), respectively. As seen from the Figure (3), the model of wet coil condition predicts the performance of the evaporator coil within 10% of relative error without any specific adjustment. Thus, it can be considered that a good agreement was obtained as the calculated values lay within the range of experimental uncertainty. This agreement validates the calculated results of the evaporator coil performance under condensate formation.

The model is used to investigate the characteristic parameters to clarify the effect of dew formation on the evaporator coil performance. The obtained results from the wet coil model are shown in Figure (4). These results were obtained with the input operating conditions shown in Figure (3-a). Comparing the total conductivity (UA) values in both wet and dry conditions, their values presented in Figure (4-a) are based on logarithmic mean temperature difference of Eq. (10). As stated previously, in the presented range of face velocity, drainage of condensate from the evaporator coil is observed experimentally, until a face velocity value of 1m/s.

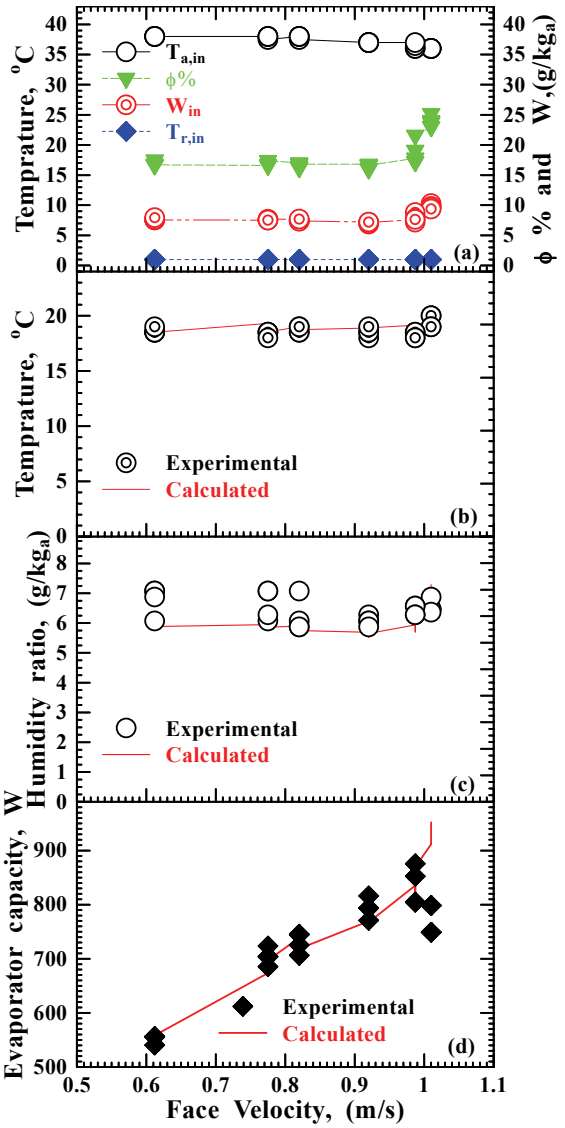

Figure 3: Measured entering operating conditions to the evaporator coil at wet condition (a), comparison of the calculated values with correspondence measured values, outlet air dry-bulb temperature (b), outlet air humidity ratio, (c) and evaporator cooling capacity (d)

In this range of face velocity, this observation agrees with the model results of 100% wet coil surface that are shown in Figure (4-b). From Figure (4-a), it is clear that both calculated (UA) values, for dry and wet conditions increases with increase in the face velocity values. This result is expected because the heat transfer coefficient is dependant on the flow Reynolds number, in which it is a function of the face velocity. While, the value of (UA) in wet conditions is higher than the case of dry coil and the difference between both (UA) values increases as the latent heat ratio value increases. This can be attributed to the following: in the present experiments, the fin pitch is 4.23mm, the retained condensate droplets on the coil do not bridge the inter-fin gap but increase the heat transfer rate. The higher $(UA)_{wet}$ value instead of retained condensate thin layer, which can represent conduction resistance, can be explained with aid of group in the

brackets of Eq. (16). The term in the bracket is the dry convective heat transfer coefficient plus the portion of latent heat of condensation.

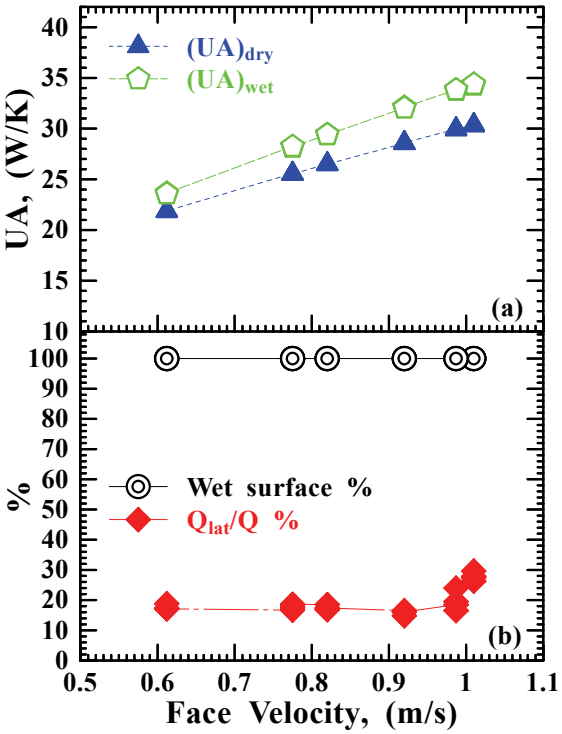

Figure 4: Characteristics of the evaporator coil under wet condition

The increase in $(UA)_{wet}$ value is function of inlet air dry-bulb temperature and humidity ratio and refrigerant temperature, with considering the conduction resistance in the tube wall is very small. The ratio of the increase on $(UA)_{wet}$ value can be clearly explained in quantity values as follows: at the latent heat to the evaporator total cooling capacity ratio (Q_{lat}/Q) value of 18.2% the values of (UA) in both dry and wet coil were 21.85 and 23.6 (W/K), respectively. While, at (Q_{lat}/Q) value of 29.64%, UA values became 30.32 and 34.31 (W/K), respectively. Thus, for the same range of a change in face velocity value, $(UA)_{dry}$ is increased by 38.76%, while when it is combined with an increase in (Q_{lat}/Q) value by 10.64%, the $(UA)_{wet}$ is 45.4%. These results clearly indicate that, an evaporator coil with higher fin-pitch is characterized by higher performance under wet condition than the dry coil surface condition and the retained condensate has an important effect on the evaporator coil performance enhancement.

4.2. Effect of Initial Formation of Thin Frost Layer on the Evaporator Coil Performance

To investigate the effect of initial formation of thin frost layer on the evaporator coil, the experimental apparatus had a minor modification compared to that described before in order to obtain entering refrigerant temperature less than 0°C. With this modification, initial formation of thin frost layer on the coil is built at low face velocity values only. An experiment was carried out for number of hours with thin frost layer formed on the evaporator coil. The measured entering conditions to the coil are shown in Fig. (5-a). The model results for the outlet air humidity ratio under frost condition were compared with experimentally obtained value as shown in Figure (5-b). It can be seen from Figure (5-b) that both results are in good agreement with the scale measurements (±7%). The calculated (UA) values for both dry and frosted coil conditions as well as the sublimated heat to the evaporator total cooling capacity ratio (Q_{sv}/Q) values are shown in (5-c). As shown in Figure (5-c), (UA) values are constant with time variation in both coil conditions instead of change in (Q_{sv}/Q) values. Also, the results shown in the figure indicate that the total conductivity under initial formation of thin frost layer $(UA)_{fr}$ has higher values than dry coil condition, for the presented operating conditions, by about 8.2%. The higher value of $(UA)_{fr}$, instead of the thin frost layer that added conduction resistance to heat transfer, can be explained with the aid of the brackets in Eq. (19). The value in the brackets is the sum of dry convective heat transfer coefficient plus the sublimated heat portion ratio.

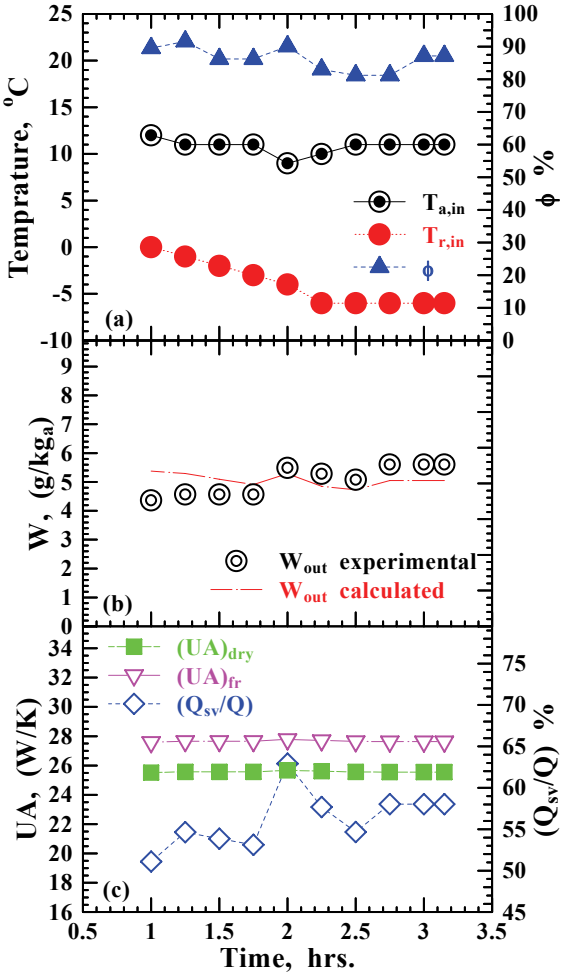

Figure 5: Measured entering operating conditions to the evaporator coil at frost condition (a), the calculated outlet air humidity ratio under frost condition compared with correspondence experimental one (b) and characteristics of the evaporator coil under thin frost formed layer (c)

Interpretation of this results are based on morphology diagram presented in Libbrecht [33], in which the initial frost layer, at tube temperature range of 0 to -5°C, consists

of a porous structure composed of individual ice crystals and air pockets. Based on this physical structure, the initial frost formation provide more pores for diffusion of the difference of air moister content ($W-W_{s,fr}$) into this initial frost layer. This difference in the air humidity is converted into frost and combined by extraction to the sublimation heat from the air stream, which has a positive effect on the heat transfer rate between the air stream and the coil. These results clearly indicate that, the evaporator coil surface with higher fin-pitch has higher performance under initial formation of thin frost layer compared with dry coil surface condition.

4.3. Effect of Frost Thin Thickness on the Evaporator Coil Performance

In the experiments for investigation of the effect of frost formation on the coil performance, no instruments were used to measure the frost thickness due to the difficulty in measuring the frost thickness in a full-scale evaporator coil. Therefore, the model is used to investigate the effect of thin formed frost thickness layer on the coil surface up to one mm on the evaporator coil performance. The result is presented in the form of the total conductivity under frost condition $(UA)_{fr}$. The calculated result correspondence to the operating conditions of face velocity equal 0.612 m/s, entering air dry-bulb temperature of 10°C, inlet air relative humidity of 87.1% and inlet refrigerant temperature of -6 °C is presented in Figure (6).

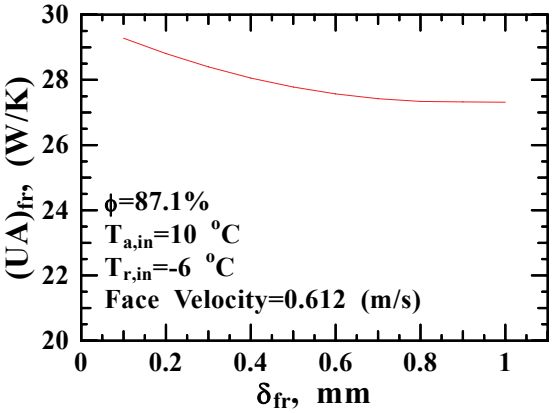

Figure 6: Effect of initial thin frost layer on the evaporator coil total conductivity (UA)fr

The result indicates that the degradation in $(UA)_{fr}$ value for frost layer thickness up to one mm is only about 6.7%. Explanation of this result is as stated in the previous subsection. Thus, it can be concluded that, the reduction in coil total heat transfer rate due to initial thin frost layer up to one mm at the stated operating condition has insignificant effect on the evaporator coil performance. While, through the aforementioned literature concerning the degradation on the evaporator coil performance at deep freezing temperatures under frost condition may be explained by the fact that, frost formation on heat exchanger surface at these low temperature has different construction, non-pours, as shown in morphology diagram presented in [33]. In addition, greater frost thickness with low fin-pitch leads to blocking of the airflow paths followed by a greater reduction of airflow rate and higher-pressure drop through the evaporator coil, resulting in a greater reduction of the evaporator coil performance. In addition, it causes additional thermal conduction resistance on the coil surface leading to dramatic decreases in the evaporator coil performance.

5. Conclusions

This study investigated experimentally and theoretically the effects of condensate and initial formation of thin frost layer on the evaporator coil surface on the performance of the evaporator coil of room air-conditioners compared with dry coil surface conditions. Experiments were carried on flat fin and staggered tube evaporator coil, while the theoretical model was used to clarify the effects of parameters which are difficult to measure in the experiments on the evaporator coil performance. The obtained results are summarized as follows:

- The model results were validated with the measured data in both wet and initial frost formation conditions of the evaporator coil, and the predicted results are within 10 % of relative error. This validation is considered a good agreement as the calculated values are within the range of experimental uncertainty.
- For the same range of a change in face velocity value, $(UA)_{dry}$ is increased by 38.76%, while when it is combined by an increase in (Q_{lat}/Q) value by 10.64%, the $(UA)_{wet}$ is 45.4%.
- The evaporator coil with higher fin-pitch is characterized by higher performance under wet condition than the dry coil surface condition.
- The total conductivity under initial formation of thin frost layer $(UA)_{fr}$ has higher values than dry coil condition by about 8.2% in the range of operating conditions of this study.
- At the stated operating condition, the degradation in $(UA)_{fr}$ under thin frost thickness up to one mm is only about 6.7% that has insignificant effect on the evaporator coil performance.

References

[1] Ali, Ahmed Hamza H. and Ismail, Ibrahim M, "Effect of the evaporator airside fouling on performance of room air conditioners and its impact on indoor air quality", ASHRAE Int. J. of HVAC&R Research, 2007, Accepted for publication

[2] Yaun Y. H. and Tucker A. S., "The performance study of a wet six-row heat-pipe heat exchanger operating in tropical buildings". Int. J. Energy Res., Vol. 27, 2003, 187–202.

[3] Jacobi A. M., Park Y., Zhong Y., Michna G., and Xia Y., "High Performance Heat Exchangers for Air-Conditioning and Refrigeration Applications (Non-Circular Tubes)". ARTI-21CR/605-20021-01, Final Report, July 2005

[4] Pirompugd W., Wongwises S. and Wang C., "Simultaneous heat and mass transfer characteristics for wavy fin-and-tube heat exchangers under dehumidifying conditions". Int. J. of Heat and Mass Transfer, Vol.49, 2006, 132–143.

[5] Halici F. and Taymaz I., "Experimental study of the airside performance of tube row spacing in finned tube heat exchangers". Heat Mass Transfer, Vol. 42, 2006, 817-822.

[6] Shin J. and Ha. S., "The effect of hydrophilicity on condensation over various types of fin-and-tube heat exchangers". Int. J. of Refrigeration Vol. 25, 2002, 688-694.
[7] O'Neill C., Beving D.E., Chen W. and Yan Y., "Durability of hydrophilic and antimicrobial zeolite coatings under water immersion". AIChE J., Vol. 52, No. 3, 2006, 1157-1161.
[8] Lee H., Shin J., Ha S., Choi B. and Lee J., "Frost formation on a plate with different surface hydrophilicity". Int. J. of Heat and Mass Transfer Vol. 47, 2004, 4881-489.
[9] Wetter M., "Simulation Model Finned Water-to-Air Coil without Condensation". Lawrence Berkeley National Laboratory Report LBNL-42355, January 1999.
[10] Osada H., Aoki H., Ohara T. and Kuroyanagi I., "Research on corrugated multi-louvered fins under dehumidification". Heat Transfer Asian Research, Vol. 30, No. 5, 2001, 383-393.
[11] Hong C. H., "Modeling and measurement of frost characteristics on heat exchanger surfaces". PhD. Thesis, University of Saskatchewan, Saskatoon, Canada, 2000.
[12] Watters R. J., O'Neal D. L. and Yang J., "Evaluation of Fin Staging Methods for Minimizing Coil Frost Accumulation". ASHRAE Res. Project: 1002-RP, July 2000.
[13] Yang J., "A study of heat pump fin staged evaporators under frosting conditions". PhD Dissertation, Texas A&M University, 2003.
[14] Chen H., Thomas L. and Besant R. W., "Fan supplied heat exchanger fin performance under frosting conditions". Int. J. of Refrigeration Vol. 26, 2003, 140-149.
[15] Hoffenbecker N., "Investigation of Alternative Defrost Strategies". M. Sc Thesis University of Wisconsin-Madison, 2004.
[16] Liu Z., Zhu H. and Wang H., "Study on transient distributed model of frost on heat pump evaporator". J. of Asian Architecture and Building Engineering, Vol. 4, No. 1, 2005, 265-270.
[17] Horuz I., Kurem E. and Yamankaradeniz R., "Experimental and theoretical performance analysis of air-cooled plate-finned-tube evaporators". Int. Comm. Heat Mass Transfer, Vol. 25, No. 6, 1998, 787-798.
[18] Verma P., Carlson D. M., Wu Y., Hrnjak P. S. and Bullard C. W., "Experimentally validated model for frosting of plain-fin-round-tube heat exchangers". Proc. of IIF–IIR Commission D1/B1 – Urbana, IL, 2002.
[19] Seker D., Karatas H., Egrican N., "Frost formation on fin-and-tube heat exchangers. Part I-Modeling of frost formation on fin-and-tube heat exchangers". Int. J. of Refrigeration, Vol. 27, 2004, 367–374.
[20] Seker D., Karatas H., Egrican N., "Frost formation on fin-and- tube heat exchangers. Part II-Experimental investigation of frost formation on fin-and-tube heat exchangers". Int. J. of Refrigeration, Vol. 27, 2004, 375–377.
[21] Aljuwayhel N. F., "Numerical and Experimental Study of the Influence of Frost Formation and Defrosting on the Performance of Industrial Evaporator Coils". PhD Dissertation, University of Wisconsin-Madison, 2006
[22] Muehlbauer, J., "Investigation of Performance Degradation of Evaporator for Low Temperature Refrigeration Applications". M. Sc Thesis, University of Maryland, College Park, 2006.
[23] Yao Y., Jiang Y., Deng S. and Ma Z., "A study on the performance of the airside heat exchanger under frosting in an air source heat pump water heater/chiller unit". Int. J. of Heat and Mass Transfer, Vol. 47, 2004, 3745-3756.
[24] ASHRAE (2005). 2005 Fundamentals Handbook SI. American Society of Heating, Refrigerating and Air-Conditioning Engineers. Atlanta, Georgia.
[25] ASHRAE, HVAC1 Toolkit: A Toolkit for Primary HVAC System Energy Calculations. American Society of Heating, Refrigerating and Air-Conditioning Engineers. Atlanta, Georgia, 1999.
[26] Doeblin, E. O. Measurement Systems, Application and Design. McGraw-Hill Book Co; 1990.
[27] Wang, C.C., Chi, K.Y., and Chang, C.J., "Heat transfer and friction characteristics of plain fin-and-tube heat exchangers, part II: correlation". Int. J. of Heat Mass Transfer, Vol. 43, 2000, 2693-2700.
[28] Payne, W. V. and Domanski, P. A., "Potential Benefits of Smart Refrigerant Distributors. ARTI-21CR/610-20050-01, Final Report, January 2003.
[29] Corberán J. M., Fernández de Córdoba P., Ortuño S., Ferri V., Setaro T. and Boccardi J., "Modeling of tube and fin coils working as evaporators or condensers". Proc. of third European Thermal Sciences Conf., Heidelberg, Germany, 2000.
[30] Corberán, J. M., Fernández de Córdoba, P., Ortuño S., Ferri, V., Gonzálvez, J., Setaro T. and Boccardi J., "Modelling of compact evaporators and condensers". Proc. of Sixth Int. Conf. on Advanced Computational Methods in Heat Transfer, Madrid, 2000.
[31] Kuehn T. H., Ramsey J. W. and Threlkeld J. L. Thermal Environmental Engineering 3rd Ed., Prentice Hall; 1998.
[32] ARI Standard 410-2001 with Addendum 2, Forced-Circulation Air-Heating and Air-Cooling Coils. May 2005.
[33] Libbrecht, K. G., "The physics of snow crystals". Institute of Physics Publishing, Reports on Progress in Physics, Vol. 68, 2005, 855–895.

JJMIE

Volume 1, Number 2, Dec. 2007
ISSN 1995-6665
Pages 79 - 84

Jordan Journal of Mechanical and Industrial Engineering

Application of Neural Net Modeling and Inverse Control to the Desulphurization of Hot Metal Process

"Moh'd Sami" S. Ashhab *

Department of Mechanical Engineering, The Hashemite University, Zarqa, 13115, Jordan

Abstract

Optimization techniques are powerful in determining inputs to a process that will drive its output to a desired target. This inverse control problem reduces to minimizing a positive cost function that measures the difference between the output and its target value. In this paper, we present a method for inverse control that uses a combination of artificial neural net modeling and optimization. We apply this method to the desulphurization of hot metal process. In this steel industry application, the sulphur content of hot metal, obtained at the end of calcium carbide powder injection into 400 ton torpedo ladles is predicted as a function of hot metal weight, treatment time, initial sulphur content, gas flow rate, and powder injection rate. Based on the prediction model, the optimization algorithm coordinates the five inputs or part of them to achieve a desired sulphur content in the hot metal.

Keywords: Inverse control; Neural network; Constrained optimization; Desulphurization;

Nomenclature

Alphabetic symbols

B_i	: column vector of size n that contains the biases from the input to the hidden layer of the neural net model
b_o	: bias (scalar) from the hidden layer to the output of the neural net model
d	: desired output value
J	: cost function
Lb	: lower input bound
M	: number of points of the simplex in the complex method algorithm
p	: number of process inputs
p_c	: number of process inputs that can be changed by the controller
U	: column vector of size p that contains the p inputs of the process.
Ub	: upper input bound
U^o	: initial input vector for the complex method algorithm
W_o	: row vector of size n that contains the weights of the neural net model from the hidden layer to the output
W_i	: matrix that contains the weights of the neural net model from the inputs to the hidden layer and has n rows and p columns
y	: neural net model output

Greek symbols

α	: reflection parameter for the complex method algorithm
ε	: termination parameter for the complex method algorithm
δ	: termination parameter for the complex method algorithm

1. Introduction

In many industrial applications, there is a need to calculate the inputs to a process that will drive its output in a desired way and thus achieve some optimum (desired) goal. In such applications a mathematical input-output model for the process is usually derived. The model could be based on the physical phenomena or available (historical) data about the process. Once the model is developed, control techniques can be used to determine the inputs to the process that will satisfy a certain given criteria.

In this paper, we deal with the inverse control problem of a multi-input-single-output process whose input/output data is given. The objective of the controller is to determine the set of inputs that will make the output of the process go to its desired target value. The input/output data is used to train an artificial neural net model with one hidden layer. This kind of identified model is an input-

* Corresponding author. e-mail: sami@hu.edu.jo

output model for which control techniques can be applied. To achieve our objective we build a positive cost function that measures the difference between the output and its target value. We use the complex method optimization to minimize this cost function. The resultant set of inputs will drive the output as close as possible to its target value. Clearly, the output will achieve its target value if and only if the minimum of the cost function is equal to zero.

Control of linear systems is well developed and neural network modeling is not needed in this case even though the procedure will give good results. A method to identify the inverse of linear systems was presented in [1]. For non-linear systems, the use of neural net modeling is helpful, especially, for the cases where a mathematical model based on the physical phenomena is difficult to obtain and process input/output data is available. The inverse model can be learned by an artificial neural network (ANN) [2]. The process inputs are predicted if the target outputs are passed to the net as inputs. There has been a lot of research on using ANN for control [3-5]. In this paper we calculate the inputs to a process based on the forward (input to output) neural net model. After proper training, the net can be used to calculate particular inputs when all the other inputs and the target output are known. This is done using optimization techniques. Thus, the ANN model functions as a versatile means for process control.

The developed inverse controller is applied to the desulphurization of hot metal process. The desulphurization of carbon saturated hot-metal in torpedo ladles is performed by injecting powdered calcium diamide through a submerged lance. Nitrogen acts as a carrier gas. The interaction between the injected gas plus powder and the liquid metal is complex because of a variety of reaction interfaces. Seven different reaction zones can be identified according to the reactor model for the ladle injection. The powder particles, on entering the gas stream, are accelerated by the high velocity of the carrier gas. On leaving the nozzle, the particles travel almost in a straight line downwards until the gas jet breaks up into a swarm of rising gas bubbles as a result of the resistance offered by the metal buoyancy forces. The final sulphur content of hot metal can be considered to be a function of five input variables, namely, treatment time, hot metal weight, initial mass content of sulphur, carrier gas flow rate, and powder injection rate [6].

A neural net model for the desulphurization of hot metal process described above is derived. The model predicts the final sulphur content of hot metal as a function of the five inputs. The error between the real and predicted outputs is small. Based on the developed neural net model of the desulphurization process an inverse controller is derived. The controller objective is to determine the five inputs or part of them that will achieve a predetermined value of the final sulphur content of the hot metal. We call this value the desired or target value of the output. The controller uses given initial inputs and the target value of the output to calculate the corresponding optimum inputs. If the optimization algorithm is successful, these inputs are mapped by the neural net model to the desired output. It should be clear that the optimum set of inputs will cause the true desulphurization process to have approximately the target value of the final sulphur content if the developed neural net model can predict the output accurately over the given range of inputs. Therefore, accurate models of the process are significant in order to obtain good performance of the controller.

2. Neural Net Modeling Experiment Design

Neural networks were originally inspired as being models of human nervous system. They have been shown to exhibit many abilities, such as learning, generalization, and abstraction [7]. Useful information about neural networks can also be found in [8]. These networks are used as models for processes that have input/output data available. The input/output data allows the neural network to be trained in a way that minimizes the error between the real output and the estimated (neural net) output. The model is then used for different purposes among which are estimation and control.

The neural net structure that we will consider in this paper is shown in Figure 1. The inputs are linked to a hidden layer which in turn is linked to the output. The components of the hidden layer are called nodes or neurons. Each link is associated with a weight. These weights are determined from given input/output data about the process such that the least square error between the given output data and the model output is minimized. The optimization process for calculating the weights of the neural net is called training. If the data used for training is huge or the number of hidden nodes is large then the training may take a long time. Once the net is trained it can be tested on a different set of data than that used for training. It is a good approach to divide the given input/output data into two parts: one part is used for training whereas the other usually smaller part is used for testing the neural net model.

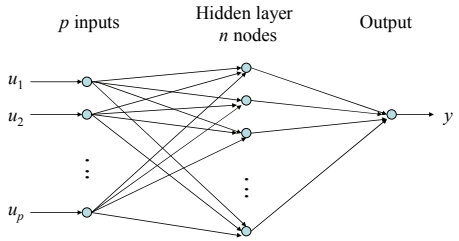

Figure 1: Neural net structure

Note that Figure 1 shows a neural net with one hidden layer. This is the case that we are going to consider since a number of results have been published showing that a feed-forward network with only a single hidden layer can well approximate a continuous function [9,10]. In practice, most processes are continuous.

An artificial neural net mathematical model that represents the structure shown in Figure 1 is written as

$$y = f(U) = W_o * \tanh(W_i * U + B_i) + b_o \qquad (1)$$

where,

y : is the output of the neural net model.

U : is a column vector of size p that contains the p inputs of the process. If there is only one input the U becomes a scalar.

W_o :is a row vector of size n that contains the weights of the neural net model from the hidden layer to the output.

W_i : is a matrix that contains the weights of the neural net model from the inputs to the

hidden layer. This matrix has n rows and p columns.

B_i : (not shown in Figure 1) is a column vector of size n that contains the biases from the input to the hidden layer of the neural net model.

b_o : (not shown in Figure 1) is the bias (scalar) from the hidden layer to the output of the neural net model.

$tanh(W_i*U+B_i)$: is a column vector that contains the hyperbolic tangent of the elements of the vector W_i*U+B_i

Each input u_j, j=1,2,…p has lower and upper bounds, Lb_j and Ub_j, respectively. These bounds are calculated from the given input data. Lb_j is the minimum value of the jth input over the given data whereas Ub_j is the maximum value of the jth input over the given data. If all the inputs lie within their lower and upper bounds then the estimated output by the neural net should lie within the given output data range. In other words, the output bounds are dictated by the neural network and the input bounds.

The number of hidden neurons affects the performance of the neural net over the training and test sets of data. More neurons make the fitting of data more accurate over the training region. It is more important to check the performance of the model over the test set of data since it was not used to calculate the parameters of the model. Overtrained neural net may perform badly over the test set. The number of nodes is usually chosen by trying different values and selecting the one that performs best over both the training and test sets of data.

3. Inverse Control

The inverse control of a process is to find the inputs to that process that will drive its output as close as possible to a given desired goal. In order to solve this problem a mathematical model of the process is needed. In this paper we deal with processes whose input/output data is available. We model the process using artificial neural networks based on the available input/output data. Optimization techniques are then used to determine the inputs to the process that will drive its output as close as possible to the given desired goal. Figure 2 illustrates these ideas. A desired signal d is passed to the inverse controller. The controller determines the input signal U to the process such that the output y of the neural net model is as close as possible to the desired signal d. The real output y_r of the process will not be equal to y unless there are no modeling errors. In practice, the performance of the controller will depend on the accuracy of the controller and the neural net model.

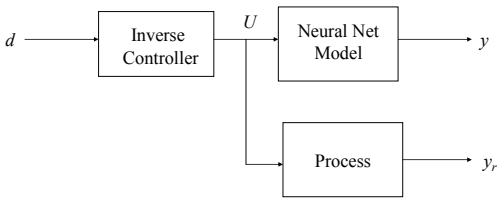

Figure 2: Inverse controller

The controller operation is characterized by minimizing a positive cost function that measures the difference between the model output and its desired value. If there is a set of inputs at which the cost function is equal to zero (minimum) then this is an optimum input. Generally speaking, the output is not equal to its target value at the initial inputs. Thus, the inverse controller coordinates the inputs or part of them to achieve the desired output if possible. Optimization over a subset of the inputs is a feature of the developed algorithm that leaves the freedom to the user to determine the other inputs in a way such that other essential requirements of the process are met. In this paper, we test our optimization algorithm on the developed neural net model of the desulphurization process (see next section).

Given a neural net model of a process as described in the previous section, we define the cost function J as:

$$J = (d - y)^2 \tag{2}$$

The cost function is expressed explicitly in terms of the model output. However, since the output is a function of the process inputs as given in the equation of the neural net model which is available in the previous section, the cost function is expressed implicitly in terms of the inputs. Note that the cost function J is non-negative and is equal to zero if and only if the output is at its desired value. In order to drive the output as close as possible to its target value we need to minimize J. Optimization techniques are best in tackling such problems.

We are now ready to define our inverse control problem: Given a process with p inputs and a single output, and a neural net model for this process. Assume that p_c of the p inputs (p_c is less than or equal to p) are allowed to change by the controller. These are called the control inputs. Minimize the cost function J subject to the following constraints

$$Lb_i \le u_i \le Ub_i, i = 1,2,...p \tag{3}$$

We are going to use the complex method to solve this constrained optimization problem. This technique will be applied to the control inputs only. The other inputs will stay constant at their given initial values. These inputs are usually set at values (within their given constraints) that satisfy some other desired conditions for the process. The complex method is based on the generation and maintenance of a pattern of search points and the use of projections of undesirable points through the centroid of the remaining points as the means of finding new trial points. In the presence of inequality constraints, it is evident that if the new point is infeasible, then it is a simple matter to retract it toward the centroid until it becomes feasible. Box proposed in [11] the complex method as a better alternative to the simplex direct search-method. The considerations that led him to the simplex modification are:

1. The destruction of the regularity of the simplex.
2. Many of the points of the regular initial simplex will be infeasible.

3. The points must be generated sequentially rather than being essentially simultaneously defined using the formula for a regular simplex.

Box proposed in [11] that the set of P trial points be generated randomly and sequentially. N samples are required to define a point in N dimensions. Each newly generated point is tested for feasibility, and if infeasible it is retracted toward the centroid of the prviously generated points until it becomes feasible. The total number to be used, P, should be no less than N+1 but can be larger. The complex method can be summarized as follows [12]:

Given an initial strictly feasible point U^o (set of inputs), reflection parameter α, and termination parameters ε and δ.

1. Generate the initial set of M feasible points. For each point $m = 1,\ldots,M$-1,
   (a) Sample p_c times to determine the point U^m. Note that the inputs that are not allowed to change are left constant at their initial values.
   (b) If U^m is infeasible, calculate the centroid U_a of the current set of points and reset
   $$U^m = U^m + \frac{1}{2}(U_a - U^p).$$
   Repeat until U^m becomes feasible.
   (c) If U^m is feasible, continue with (a) until M points are available.
   (d) Evaluate $J(U^m)$, for $m = 0,1,\ldots,M$-1.
2. Carry out the reflection step.
   (a) Select the point U^R such that $J(U^R) = \max J(U^m) \equiv J_{\max}$.
   (b) Calculate the centroid U_a and the new point $U^n = U_a + \alpha(U_a - U^R)$.
   (c) if U^n is feasible and $J(U^n)$ is greater than or equal to $J_{\max}$, retract half the distance to the centroid U_a. Continue until $J(U^n)$ becomes less than $J_{\max}$.
   (d) If U^n is feasible and $J(U^n) < J_{\max}$, go to step 4.
   (e) If U^n is infeasible, go to step 3.
3. Adjust for feasibility
   (a) Reset violated variable bounds:
   If $u_i^n < Lb_i$, set $u_i = Lb_i$.
   If $u_i^n > Ub_i$, set $u_i = Ub_i$.
   Note that the subscript i denotes the ith input. This step will be applied only to the control inputs since the other inputs are set within their constraints initially.
   (b) If the resulting U^n is infeasible, retract half the distance to the centroid. Continue until U^n is feasible, then go to step 2(c).
4. Check for termination.
   (a) Calculate
   $$J_a = \frac{1}{M}\sum J(U^m)$$
   and
   $$U_a = \frac{1}{M}\sum U^m.$$
   (b) If
   $$\sum_m (J(U^m) - J_a)^2 \le \varepsilon$$
   and
   $$\sum_m \left\| U^m - U_a \right\| \le \delta$$
   Terminate. Otherwise, go to step 2(a).

The search is terminated when the pattern of points has shrunk so that the points are sufficiently close together and/or when the differences between the function values at the points become small enough.

Box has performed numerical experiments in [11] with this algorithm, and on this empirical basis recommends using $\alpha = 1.3$ and $M = 2p_c$. Biles [13], on the other hand, reports good results with $M = p_c + 2$. The $\alpha > 1$ compensates for shrinking of the complex caused by halving the distances, while the large number of vertices is intended to prevent the complex from collapsing and flattening out along the constraints. The setting at the value of the bound is intended to avoid unnecessary contraction of the complex.

The complex method requires that the feasible region be a convex set. This requirement arises in two places: in the calculation of the centroid and in the retraction of a feasible but unsatisfactory point. For nonconvex regions the method could fail to converge satisfactorily. In practice, the method is widely used and has successfully solved numerous nonconvex problems. Thus, the above situation must arise with low probability.

4. The Desulphurization of Hot Metal Process

The primary objective of introducing powdered reagents into liquid steel, with the help of either cored wire or a carrier gas, is for desulphurization, deoxidation, alloy dissolution and inclusion shape control. Injection technology and equipment are well advanced and available on commercial basis [6].

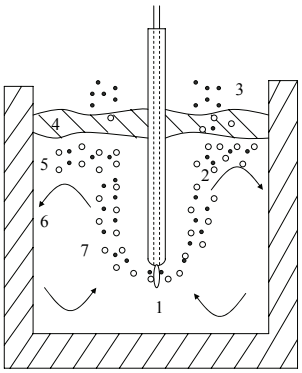

Figure 3: Reactor model for ladle injection. The different reaction zones are: (1) jet zone in front of lance outlet; (2) plume zone containing bubbles and particles rising in metal; (3) breakthrough zone where bubbles emerge; (4) slag zone; (5) dispersion zone where gas-slag-metal emulsion can form; (6) lining zone where metal may react with lining; and (7) intermediate zone with lowest stirring intensity [6]

The desulphurization of carbon saturated hot-metal in torpedo ladles is performed by injecting powdered calcium diamide through a submerged lance (see Figure 3). Nitrogen acts as a carrier gas. The interaction between the injected gas plus powder and the liquid metal is complex because of a variety of reaction interfaces. Seven different reaction zones can be identified according to the reactor model for the ladle injection. The powder particles, on entering the gas stream, are accelerated by the high velocity of the carrier gas. On leaving the nozzle, the

particles travel almost in a straight line downwards until the gas jet breaks up into a swarm of rising gas bubbles as a result of the resistance offered by the metal buoyancy forces. The final sulphur content of hot metal can be considered to be a function of five input variables, namely, treatment time, hot metal weight, initial mass content of sulphur, carrier gas flow rate, and powder injection rate.

The desulphurization process is very complex and is affected by many parameters as mentioned above. It is almost impossible to derive a mathematical model for such a chemical process based on physical phenomena. The input/output data for the system is available which allows modeling with neural networks. The data for the desulphurization of hot metal process is provided in [14] and has 51 patterns. Each pattern includes the data about the five inputs and the corresponding output which is the final sulphur content, namely, each pattern includes data for the five inputs:

1. Treatment time
2. Hot metal weight
3. Initial mass content of sulphur
4. Carrier gas flow rate
5. Powder injection rate
6. and the single output which is the final sulphur content.

Forty of the provided 51 data patterns are used to train a neural net model for this process, whereas the remaining 11 data patterns are used to test the performance of the model. We ran experiments for different numbers of hidden neurons. It was observed that the quality of the results depends on this number. The least square error versus the number of hidden neurons is plotted for the training and test regions in Figure 4. We choose the ANN with 25 hidden neurons since it produces the minimum least square error over the test region and a very small least square error over the training region. The real and predicted (ANN model) sulphur content are plotted in Figure 5 as a function of the pattern index which starts from 1 and ends at 51. Note that in the training region (index < 41) the predicted values are very close to the real ones. The corresponding least square error is 0.0032 and standard deviation is 0.0005. On the other hand, there are some errors at indices 43 and 48 within the test region. The test least square error and standard deviation are 0.0110 and 0.0034, respectively. The results are acceptable compared to the ones generated by neural models in the literature. In [14] the authors used the same training patterns to obtain a neural net model that predicts the final sulfur content. Their generalization results over the same test set we have above are shown in Figure 6. The corresponding least square error and standard deviation are 0.0116 and 0.0037, respectively. Note that our results over the test region are slightly better which shows that our ANN model is satisfactory and thus will be utilized by the proposed inverse controller later in this section.

The neural network that represents the mathematical model for the desulphurization process consists of 25 hidden neurons and there are five inputs. In this case, there are more parameters than data points. Over fitting is expected under these conditions. The available data for the desulphurization process consists of 51 patterns. Part of this data must be used for training the neural net and the rest of data is used for testing the performance of the neural network.

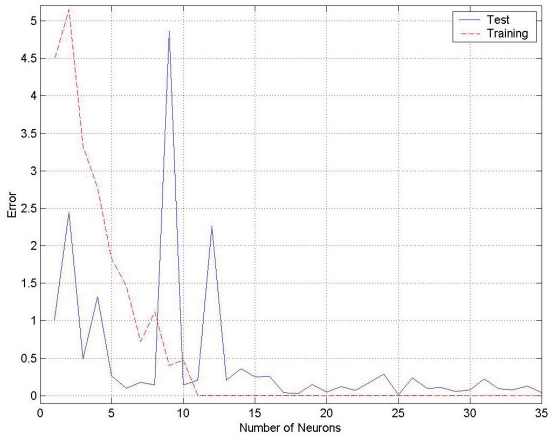

Figure 4: The least square error versus the number of hidden neurons for the training and test regions

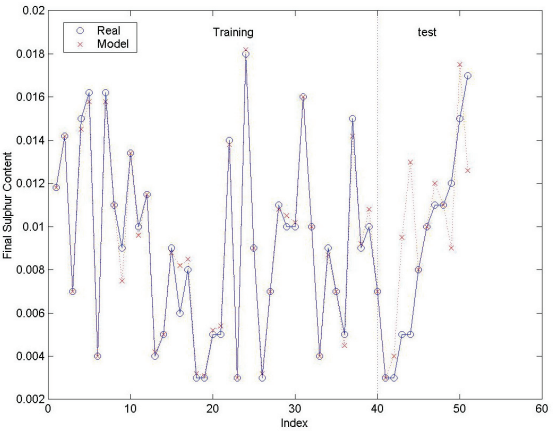

Figure 5: Neural net model results

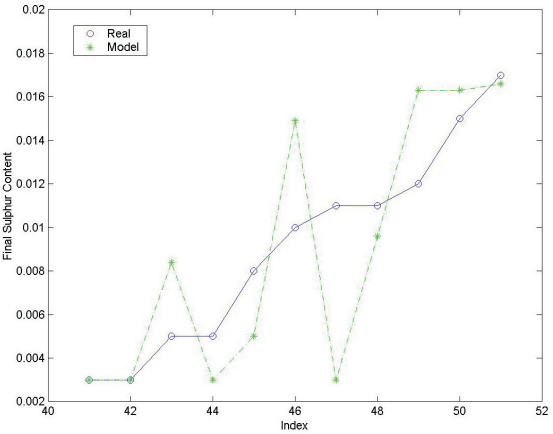

Figure 6: Neural net model results of [14]

We use about 80% of the patterns for training and 20% of the patterns for testing the neural network. Over fitting is avoided when neural nets with small number of neurons are used. However, it was observed that the performance over the test region is bad in these cases. Increasing the number of neurons causes over fitting in the training region. Therefore, the quality of the neural net is judged by its performance over the test region. In the case of the desulphurization process the best performance over the test region was obtained with 25 hidden neurons. It is worth to point out that in order to construct better models for the

desulphurization process more data points should be generated.

The optimization algorithm described earlier in this paper uses given initial inputs to the desulphurization of hot metal process and a target (desired) value of the final sulphur content in order to calculate the optimum set of inputs that will cause the actual final sulphur content to be equal to its desired value. As discussed above, the algorithm represented in this paper is based on the neural net model of the process. Optimization over a subset of the inputs is an important feature of the algorithm. This allows choosing the other inputs such that some essential requirements can be satisfied. We now present the simulation results that demonstrate the optimization algorithm ability in driving the final output sulphur content from a given initial value to a final desired one by coordinating the inputs to the desulphurization process. We pick one of the available data patterns to be the initial state. The inputs thus have the following initial values:

1. Treatment time = 430 seconds
2. Hot metal weight = 267 tons
3. Initial sulphur content = 0.021%
4. Gas flow rate = 0.677 m^3 / min.
5. Powder injection rate = 50 kg / min.

The corresponding initial value of the sulphur content is 0.015% as calculated from the neural net model. We would like to reduce the sulphur content to a final value of 0.0117 by regulating only two out of the above five inputs, namely, treatment time and gas flow rate. The remaining three inputs will be fixed at their initial values. The simulation results

of the optimization algorithm in this case are shown in Figure 7. The three subplots show history of the two inputs and output in terms of the iteration number of the complex method. The inverse controller achieves its goal of moving the final sulphur content to 0.0017 in ten iterations. The corresponding optimum values of the inputs are treatment time = 699 seconds and gas flow rate = 0.6 m^3 / min. Iteration 0 represents the initial condition for the optimization algorithm or inverse controller.

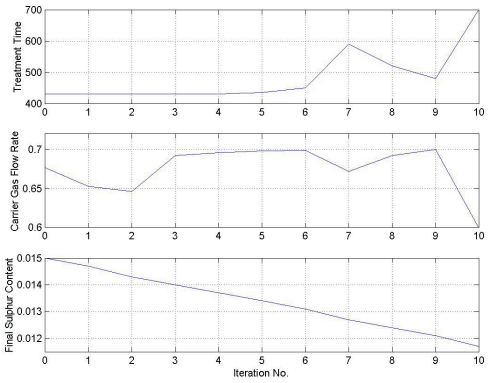

Figure 7: Inverse controller performance

5. Conclusions

A method for inverse control of processes with available input/output data was developed. The method consists of neural net modeling and constrained optimization using the complex method. The developed inverse controller was tested on the desulphurization of hot metal process. The controller achieves its objective.

References

[1] B. Widrow, J. McCool, B. Medoff, "Adaptive control by inverse modeling". Twelfth Asilomar Conference on Circuits, Systems, and Computers, 1979.

[2] A. Karniel, R. Meir, G. Inbar, "Best estimated inverse versus inverse of the best estimator". Neural Networks, Vol. 14, 2001, 1153-1159.

[3] K. Narendra, K. Parthasarathy, "Identification and control of dynamical systems using neural networks". IEEE Transaction On Neural Networks, Vol. 1, No. 1, 1990, 4-27.

[4] D. Bullock, S. Grossberg, F. Guenther, "A self-organizing neural model of motor equivalent reaching and tool use by a multijoint arm". Journal of Cognitive Neuroscience, Vol. 5, No. 4, 1993, 408-435.

[5] A. Karniel, G. Inbar, "Human motor control: Learning to control a time-varying non-linear many-to-one System". IEEE Transactions on Systems, Man, and Cybernetics Part C, Vol. 30, No. 1, 2000, 1-11.

[6] Deo B, Boom R. Fundamentals Of Steelmaking Metallurgy. New York: Prentice Hall, 1993.

[7] Patterson D. Introduction To Artificial Intelligence And Expert Systems. New York: Prentice Hall, 1990.

[8] Haykin S. Neural Networks: A Comprehensive Foundation. New York: Prentice Hall, 1998.

[9] G. Cybenko, "Approximations by superpositions of a sigmoidal function". Math. Control Signal Systems, Vol. 2, 1989, 303-314.

[10] K. Funahashi, "On the approximate realization of continuous mappings by neural networks". Neural Networks, Vol. 2, 1989, 183-192.

[11] M. Box, "A new method of constrained optimization and a comparison with other methods". Computer Journal, Vol. 8, 1965, 42-52.

[12] Reklaitis G. Engineering Optimization. New York :John Wiley & Sons; 2002.

[13] W. Biles, "Optimization of multiple response simulation models". Final Report, ONR-Contract N00014-76-C-1021, University of Notre Dame, 1978.

[14] A. Datta, M. Hareesh, P. Kalra, B. Deo, R. Boom, "Adaptive neural net (ANN) models for desulphurization of hot metal and steel". Steel Research, Vol. 65, No. 11, 1994, 466-471.

JJMIE

Volume 1, Number 2, Dec. 2007
ISSN 1995-6665
Pages 85 - 91

Jordan Journal of Mechanical and Industrial Engineering

A Computer Based Approach for the Design of the Orifice-Compensated with Feeding Pocket Annular Hydrostatic Thrust Bearings

M. Al-Ajlouni *

Mechanical Engineering Department, Engineering Faculty, Mu'tah University, Mu'tah 61710, Jordan

Abstract

The orifice-compensated with feeding pocket annular hydrostatic (OCFPAH) thrust bearing is a unique type of gas bearing with many distinguishing characteristics. It is finding many applications in ultra high-speed rotors. A computer code was written to overcome the difficulties involved in the design of such a bearing. Initially, the design charts were converted into the alternative equations using a curve-fitting technique. The program, which is based on these equations, was designed so that mechanical and physical properties of the lubricant and the main dimensions of the bearing can be entered in a user-friendly manner. Many runs of the code have been carried out successfully. The code has proven to be fast, compatible with CAD and CAD/CAM packages as well as the ability of linking it with data banks and the Internet.

Keywords: Design; Hydrostatic thrust bearings; Stiffness;

Nomenclature

Alphabetic Symbol

a : Orifice radius.[mm **or** inch]
B : Axial damping.[N sec m^{-1} **or** lbs sec/inch]
$(B = \overline{B}\,\mu R_o \left(\frac{R_o}{C}\right)^3)$
C : Film thickness.[mm **or** inch]
$(C \cong 0.5 \times 10^{-3}$ to 2×10^{-3} inch$\cong$ 12.5 to 50 μm)
d : Feeding hole diameter.[mm **or** inch]
K : Axial stiffness.[N m sec^{-1} **or** lbs/inch]
$(K = \overline{K}\,(\frac{1}{C}\pi(R_o^2 - R_i^2)(p_s - p_a)^{1+2/3\delta^2}/_{1+\delta^2}))$
n : Number of holes.
("nξ" must be greater than "nξ"$_{min}$)
n_p : Number parameter.($n_p = d / 2\xi R_c$)
p_a : Ambient pressure [Bar **or** psi]
p_s : Supply pressure.[Bar **or** psi]
Q : Mass flow rate.[cfm **or** lbs sec/inch]
$(Q = \overline{Q}\,\Pi C^3 p_s^2 / 6\mu\,\Re\,T)$
R_c : Hole radius [mm **or** inch]
$(R_c = \sqrt{R_o R_i} \quad \pm 20\%)$
R_i : Inner radius [mm **or** inch]
R_o : Outer radius.[mm **or** inch]
T : Temperature.[° R **or** K]
W : Bearing load [N **or** lb]
$(W = \overline{W}\ \pi\left(R_o^2 - R_i^2\right)(p_s - p_a))$
V_i : Feeder hole volume [(mm **or** inch)^3]

Greek symbols

Λ_S : The restrictor coefficient
$(\Lambda_s = 6\mu n a^2 \sqrt{\Re T} / p_s C^3 \sqrt{1+\delta^2})$
μ : Gas viscosity [N sec m^{-2} **or**. lb sec/inch^2]
σ : Squeeze number ($\sigma = 12\mu\nu(R_o/C)^2/p_a$)
ν : Vibratory frequency [rad/sec]
δ : Ratio of orifice area to the clearance
ξ : Logarithmic radii ratio ($\xi = 0.5 \log_e(R_o / R_i)$)

Notes:

[….] Unit: *'Imperial' units are used only in the intermediate stages to be compatible with the available design equations and charts, whilst SI units are used as input and output of the design.*

(…..) Governing equation: *Using the dash ' ¯ ' as a superscripts means that this value is a dimensional one and can be extracted from the design charts in the conventional method or direct by the code with the new approach.*

* Corresponding author. e-mail: ajlouni@ mutah.edu.jo

1. Introduction

Thrust bearings are widely used in many engineering applications. Sternlicht [1] in his key paper, presented the different fields of use of these bearings that include aerospace, nuclear, refrigeration, textile, chemical, medical, food and pharmaceutical industries. He also, listed the machines such as turbines, compressors, generators, motors, pumps, centrifuges, blowers, and expanders in which these bearings were used. The main function of thrust bearings is to support the axial load and position of the rotors. Considerable work has been carried out towards their development of various types of thrust bearings over the past decades and the recent technological advance make this an opportune time for any study in their science and development. Characterization and classification of different types of thrust bearings can be found in many references [1-6]. Figure 1 shows an orifice-compensated with feeding pockets annular hydrostatic (OCFPAH) thrust bearing which was selected for this project. The selection procedure was based on the fact that gas bearings have the ability to operate over a wide range of temperatures with low friction and low power loss. Their construction and service is simple as no oil lubrication system is required in addition to their cleanliness and stability of lubricant. Hydrostatic bearings have a number of inherent advantages such as; high load carrying capacity without the influence of the rotating speed, film thickness can be controlled by varying the supply and orifice geometry without major changes in the overall bearing and starting and stopping are not considered critical problems.

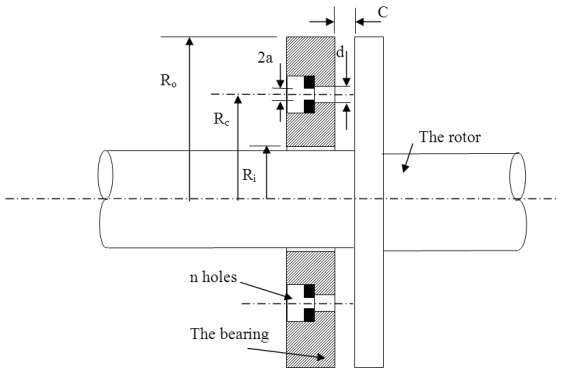

Fig. 1. Schematic of the (OCFPAH) thrust bearing

Above all, the (OCFPAH) thrust bearing has other special features like its relatively high stiffness, easy construction and its reliability in operation. Full details can be found in many references [1-6].

It is important to note that the design procedure of this type of bearing is rather lengthy and complicated as the procedure must go through a sequence of designing charts and equations analogous to that found in Cheng [5]. Fuller [7] in his review paper mentions that the designer needs to have a sharper pencil when working with gas-lubricated bearings. They are less forgiving of errors in estimating loads or of deviations from specifications during manufacture and installation and less forgiving of distortions that may find their way into the rotor, the bearing components or the housing. Further complications will arise particularly if the stiffness of the bearing is to be optimized then controlling the dimensions of the bearing and the supply pressure can alter the stiffness. Henceforth, any changes in the above(e.g. supply pressure, dimensions, temperature and etc.) would require a repetition of the whole procedure and the manual calculations becoming impractical. Therefore, the main aim of this paper is the development of a computer code for the design of this type of bearing. This is realized with Visual Basic code with a user-friendly environment in order to include the effect of a wide variety of design parameters.

2. Problem Definition And Theoretical Background

Fig. 2 shows design procedures that must be conducted in a number of steps namely; entering or specifying the dimensions, calculating the governing parameters, calculating the characteristic quantities, checking stage and calculating the final output. These steps are quite lengthy and laborious, but the third step that deals with calculating the characteristic quantities, however, is the hardest because the design charts must be accessed at all times. As an example, Figures 3, 4, 5 show only one set of charts related to one value of radius ratio (R_o/R_i = 1.25). This indicates that each one of these charts contains six different curves related to six values of pressure ratios (P_o/P_i = 2, 4, 7, 10, 15 and 20) giving a wide range of pressure values. Different radii ratios (R_o/R_i = 1.5, 2 and 3) obtained from Cheng paper [5] will also be used in this work. Figure 6 shows design chart that can be used to find the minimum number of feed holes required. The checking stage also contains a few important points that need to be examined in order to prove the withstand ability of its operating conditions. The final stage also includes calculations of output properties of such bearing using a complicated set of equations similar to the ones illustrated in the appendix. It is necessary to note that the proof or derivation of these well-established equations is beyond the scope of this paper and can be found in many references like Cheng [5 and 6], Vohr [8] and Lund [9].

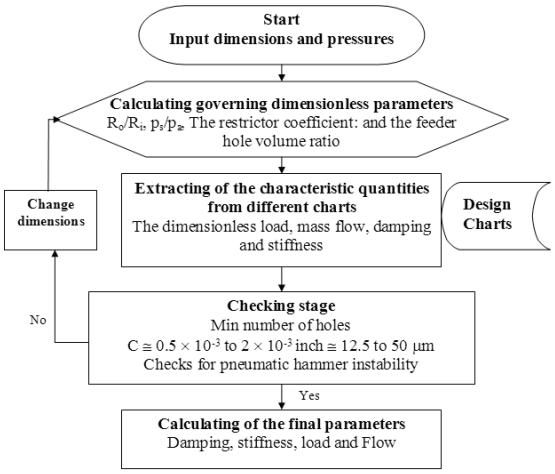

Fig. 2. The design processes of the (OCFPAH) thrust bearing

The difficulty in determining the bearing dimensions and properties for any particular design case is quite

apparent at this stage, and even becoming impractical specially if the bearing operating conditions are to be altered or changed.

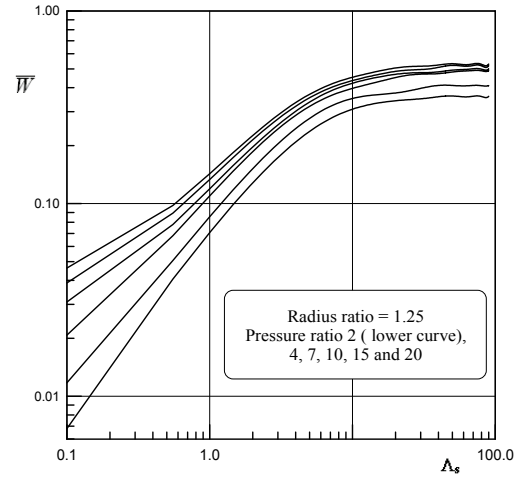

Fig. 3. The design chart for determining the dimensionless load ($\overline{W}$)of the (OCFPAH) thrust bearing for radius ratio (Ro/Ri) =1.25 (other ratios are not shown)

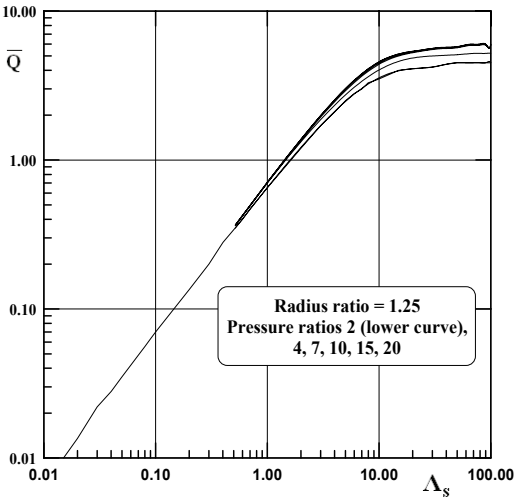

Fig. 4. The design chart for determining the dimensionless flow ($\overline{Q}$)of the (OCFPAH) thrust bearing for radius ratio (Ro/Ri) =1.25 (other ratios are not shown)

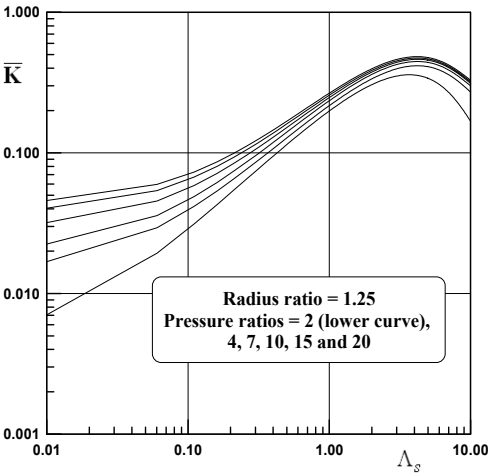

Fig. 5. The design chart for determining the dimensionless stiffness ($\overline{K}$) of the (OCFPAH) thrust bearing for radius ratio (Ro/Ri) =1.25 (other ratios are not shown).

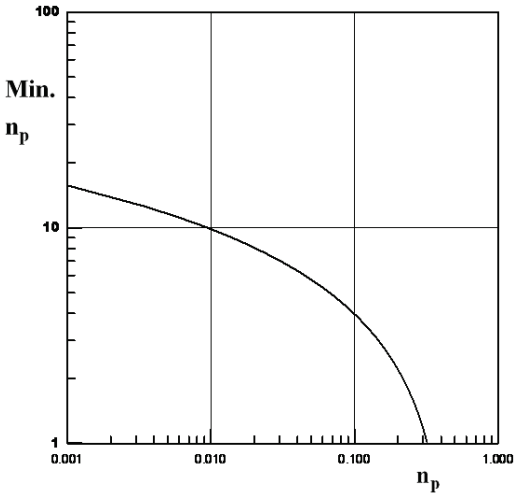

Fig. 6. The design chart for determining the number of feeder holes of the (OCFPAH) thrust bearing

3. The Methodology Used

The conversion of the equations into a computer code is an easy task with special care to the programming language syntax. The more complicated task, however, is how to make the computer understand the different charts. Using curve fitting techniques in converting each chart into an accurate equivalent formula solved this problem. A standard procedure was used in converting of the required design charts into very accurate equations with the aids of a graphic software called Grapher. The required types of equations for usage in the calculation process were accurately chosen from a list of multi-models in order to find the exact equivalent solution. The statistical data extracted like the coefficient of determination and the residuals proved that the accuracy of this process is very high.

The above equations have been converted into a Visual Basic Code. Visual Basic has been chosen because of its super characteristics as it contains strong software's instructions, perfect compatibility with windows applications and easy to operate. The code was designed to be as general as possible. In practice, the most important step is the calculation of load, flow, stiffness and damping. The mechanical and physical properties can be entered by the user or can be extracted directly from the available database in the program. The user will enter the main dimensions of the bearings. Many other dimensions, parameters and characteristics will be calculated by the code itself. One more function of the code is the large amount of information that is built-in the program. These include information about thrust bearing classifications, characteristics, key references, the full statistical data of the formulae used, and help utilities. This data was collected from different sources in the literature and distributed in different branches of the main menu of the program. The output of the code can be displayed on the screen, and the data can be saved on a file or printed on a hard copy.

The program, at this stage, contains a frame that can be filled with many more information and calculations. The

code, also, can be connected to other software that work on the complementary sides of it, like, rotor dynamics and other bearing types.

4. Curve Fittings

It is common practice for engineers to start fitting the data linearly, as it is the simplest model. Failure of the linear model will lead to representing the data by plotting these paired data on various types of graph paper. This is carried out in order to determine whether a suitably transformed scale and their corresponding points will fall close to a straight line or not. In this way, any transformation that suggests a straight line regression equation, the constant parameter(s) can be estimated or determined using the well-known method called least square method [10-14]. It can be said, however, that if there is no clear indication about the functional form of the regression of Y on X, we often assume that the underlying relationship is at least "well-behaved" to the extent that it has a Taylor series expansion and that the first few terms of this expansion will yield a fairly good approximation. The data, thus, is fit on a polynomial equation, where its degree can be determined by direct inspection of the results. An alternative method can also be used, that is by minimizing the sum of the squares of the vertical distances from the point to the curve and taking the partial derivatives with respect to all parameters and equating their partial derivatives to zero [11].

The above procedure has been used with the following general notes and guidelines:

1. The risk inherent in extrapolation.
2. The search actually seek a polynomial of the lowest possible degree that adequately describes the data.
3. Determining the degree of the polynomial by inspection or by a more rigorous method. Essentially, by first fitting a straight line as well as a second-degree polynomial and test whether the case gained by including the quadratic term. If this hypothesis was rejected, then one must fit a third-degree polynomial and the effect of the cubic term is then tested. This procedure is continued until the hypothesis cannot be rejected in two successive steps and there is, thus, no apparent advantages in carrying out the extra terms [12-14].

4.1. The load Capacity of the thrust bearing

The load of the (OCFPAH) thrust bearing may be influenced by many parameters. Investigations of such parameters can be carried out by plotting the load at different values of the restrictor coefficient whilst the pressure ratio and radius ratio are maintained constant. Other values of pressure ratio or radius ratio need other design charts similar to those explained above. The entire effect of all these parameters can be observed in a family of design charts like those found in Cheng [5], where the required statistical data of the first value of pressure ratio(R_o/R_i=2) and radius ratio (R_o/R_i =1.25) for the curve fitting is extracted from the original design charts. The data are then converted into pairs of mathematical (the restrictor coefficient) and random (the dimensionless load) variables. Drawing the variables on different graph papers (normal, log-log, semi-log, etc.) proves that it cannot be straightened out by any standard technique and, thus, the linear model cannot be reached. Hence, a polynomial model must be used in representing the data. Starting from the second-degree polynomial and increasing its degree step by step and keep inspecting the effect of that leads to a very confident result with the tenth degree polynomial. Other similar trials were carried out for different values of pressure ratios (namely 4,7,10,15 and 20). The results obtained from curve fitting for these trials for different conditions are presented in Table 1 and in Figure 3.

4.2. The flow through the thrust bearing

The flow through the (OCFPAH) thrust bearing can be affected by many parameters. These effects, as in the case of the load calculation, can be seen with a family of design charts. The previously described procedure can also be used here to collect the required statistical data and to convert them into pairs of mathematical (the restrictor coefficient) and random (the dimensionless flow) variables. The polynomial model is again used to represent the data. The results obtained for curve fitting for the different conditions are presented in Table 2 and in Figure 4.

Table 1: The results of curve fitting of the load of the (OCFPAH) thrust bearings with different pressure ratios and with radius ratio = 1.25

Pressure ratio		2	4	7	10	15	20
Polynomial coefficients	Degree 0	0.0012E-10	0.00259993	0.00951562	0.0197223	0.0267031	0.0339925
	Degree 1	0.08062601	0.0925192	0.114349	0.112973	0.122239	0.124698
	Degree 2	0.00920107	0.0101155	-.0152103	-.0142421	-.0167423	-.0169637
	Degree 3	0.00064731	0.00062018	0.0011961	0.00108646	.00138093	0.0013883
	Degree 4	2.9877E-5	-.34942E-5	-5.7754E-5	-.23343E-5	:-10252E-5	-7.0775E-5
	Degree 5	9.2136E-7	5.8632E-7	1.7716E-6	1.6286E-6	2.3326E-6	2.3043E-6
	Degree 6	1.8918E-8	-.9399E-9	-.51488E-8	-.30382E-8	-4.9444E-8	-.84804E-8
	Degree 7	2.53506	1.1414E-10	4.492E-10	4.3289E-10	6.7123E-10	6.5425E-10
	Degree 8	2.1187E-12	-.5137E-13	-.5677E-12	-.5252E-12	-5.623E-12	-5.457E-12
	Degree 9	9.9909E-15	3.7138E-15	1.6012E-14	1.6201E-14	2.6435E-14	2.5567E-14
	Degree 10	2.0255E-17	-.1626E-18	-.1010E-17	-3.207E-17	-5.328E-17	-5.141E-17
Residuals*		0.00042545	0.00079808	0.00022594	0.00074087	0.00091901	0.00126009
R^2**		0.999195	0.998802	0.999744	0.999177	0.999022	0.998692

* Sums of Squares of Residuals about Polynomial

** Coefficient of Determination (R-squared)

Table 2: The results of curve fitting of the flow through the (OCFPAH) thrust bearing with different pressure ratios & with radius ratio = 1.25

Pressure ratio		2	4	7	10	15	20
Polynomial coefficients	Degree 0	-0.0011197	-0.0173592	-0.0158591	-0.0196556	-0.0182668	-0.0182668
	Degree 1	0.703616	0.77185	0.748359	0.759607	0.749732	0.74973
	Degree 2	-0.0511522	-0.0541708	-0.0298796	-0.028081	-0.0214549	-0.0214549
	Degree 3	0.00216023	0.00224434	-0.0011824	-0.0016026	-0.0024620	-0.0024620
	Degree 4	-6.5382E-5	-5.9771E-5	0.00017008	0.00020174	0.00025446	0.00025446
	Degree 5	1.6798E-6	1.0591E-6	-7.7213E-6	-8.9793E-6	-1.0831E-5	-1.0831E-5
	Degree 6	-3.5515E-8	-1.2601E-8	1.9174E-7	2.2146E-7	2.6149E-7	2.6149E-7
	Degree 7	5.3264E-10	1.0033E-10	-2.8491E-9	-3.2808E-9	-3.8232E-9	-3.8232E-9
	Degree 8	-5.011E-12	-5.264E-13	2.525E-11	2.9031E-11	3.3524E-11	3.3524E-11
	Degree 9	2.6124E-14	1.7258E-15	-1.231E-13	-1.415E-13	-1.623E-13	-1.623E-13
	Degree 10	-5.733E-17	-2.817E-18	2.544E-16	2.9231E-16	3.3357E-16	3.3357E-16
Residuals*		0.0118048	0.0646438	0.0686515	0.0940048	0.106286	0.106286
R2**		0.999906	0.999618	0.999676	0.999566	0.99952	0.99952

Table 3: The results of curve fitting of the stiffness of the (OCFPAH) thrust bearings with different pressure ratios & with radius ratio = 1.25

Pressure ratio		2	4	7	10	15	20
Polynomial coefficients	Degree 0	0.00457279	0.0143095	).019739	0.0291722	0.0376087	0.0429851
	Degree 1	0.248417	0.253803	0.270389	0.273506	0.275645	0.280146
	Degree 2	-0.0601906	-0.0567191	-0.0608826	-0.0612723	-0.0620105	-0.0632268
	Degree 3	0.00631848	0.00573283	0.00623178	0.00623401	0.00633225	0.00647457
	Degree 4	-0.0003648	-0.0003253	-0.0003574	0.00035574	-0.0003625	-0.0003713
	Degree 5	1.27054E-5	1.12487E-5	1.24514E-5	1.23414E-5	1.26079E-5	1.29242E-5
	Degree 6	-2.778E-7	2.45462E-7	2.73016E-7	-2.6972E-7	-2.7611E-7	-2.8307E-7
	Degree 7	3.83601E-9	-3.3918E-9	-3.7837E-9	3.72822E-9	.82306E-9	3.91805E-9
	Degree 8	-3.245E-11	2.875E-11	-3.213E-11	-3.159E-11	-3.244E-11	-3.323E-11
	Degree 9	1.534E-13	1.363E-13	1.5242E-13	1.4963E-13	1.5383E-13	1.5745E-13
	Degree 10	-3.102E-16	2.764E-16	-3.093E-16	-3.032E-16	-3.12E-16	-3.191E-16
Residuals		0.0059766	0.00628429	0.00990691	0.0106458	0.0123008	0.01262
R^2		0.989296	0.991683	0.988507	0.988228	0.986709	0.986828

4.3. The Stiffness of the thrust bearing

Many parameters may also affect the stiffness of the (OCFPAH) thrust bearing. These effects, as in the case of the load and flow calculation, can be seen with a family of design charts. The same procedure was used in collection of the required statistical data and converting them into pairs of mathematical (the restrictor coefficient) and random (the dimensionless stiffness) variables. Similarly, the polynomial model is again used to represent the data. The results obtained for curve fitting with the different conditions are presented in Table 3 and in Figure 5.

4.4. Number of holes

The minimum number of holes is an important design output and it is a function of the number parameter that is defined in the appendix. The data proved that the function is intrinsically linear. Graphing the relation between log (Number parameter) in X axis and Log (Minimum Number parameter) in Y axis results in a straight line with the equation:

*Log (nξ) = -2.54638 * log (np) - 1.89372*

with the following statistics:

- Residual sum of squares = 6.63503
- Coefficient of determination, R-squared = 0.985326
- Residual mean square, sigma-hat-sq'd = 0.315954

This equation is shown in Fig. 6 and it will be used at latter stage in the program.

5. Construction Of The Program

Figure 7 shows the main structure of the program without showing any sub forms. The drop lists that are located at the top of this form allow the user to perform many functions directly. This includes File, Air properties, Dimensions, Calculations, Results, Information, References and Help. Most functions can be performed by other methods like clicking above the designed icons that are shown below the drop list menu in the main tool bar. All other forms of the code have been designed as child forms of the above form. The main choice among all of these varieties for this paper is the calculations sub form shown in Fig. 8 after performing a numerical example. From this calculations form, it can be seen that, many other sub forms can be easily addressed. After completing the entries of the input properties and dimensions, the calculation process can be started by clicking above the calculating icon. The result will be displayed directly at proper locations as illustrated in Fig. 8.

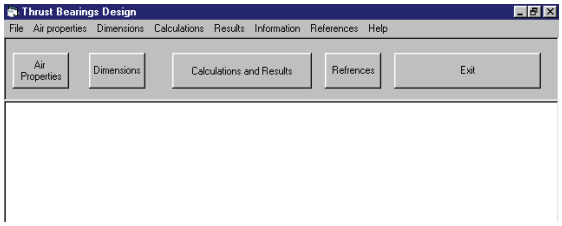

Fig. 7. The main form of the program for the design of (OCFPAH) thrust bearing.

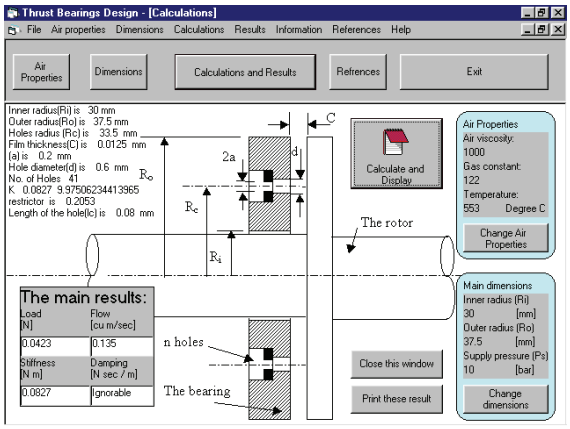

Fig. 8. The calculation form including the result of the numerical example.

The code is user-friendly and can be used like any other window software. When starting the program, the user will enter the main menu after passing through the welcoming form. The input data should be entered from the dimensions and air properties forms. All output data is obtained from the calculations and results form. Any change of the input parameters will immediately cause a change in the results. One more feature of the program is the huge amount of information about thrust bearings, which is built-in the code and can be seen from the Information drop list. Many other features of the program will not be explained here because they are from the standard style of many other window applications.

6. Results And Discussion

The code has been used for many trials in the debugging stage until the final edition has been reached. Using this final version is very easy and clear results come out rapidly. Many tasks have been carried out with the code and the results proved that it is work probably as expected. A couple of numerical examples are shown here. The first was worked out previously using the traditional method. This example represents a design of a thrust bearing for a very high speed [around 50000 rpm] rotating tube. Table 4 shows the bearing dimensions which are chosen according to application data. This data is used as inputs to the design chart. Table 4 also shows the main check points that are used as an indicator of the validity of the design chart. The second part of the table shows the dimensionless output quantities and the real value of the load, flow, damping and stiffness. The calculated results by the code, as shown in figure 8, are almost the same as that of the traditional method, used by the author in previous work [2]. The main difference is in the time consumed and the expertise of the designer. The time consumed in using the traditional method takes many working hours, compared to that of a few minutes in operating or using the procedure. The traditional method requires from the designer to be an expert in the field whilst any person with a little knowledge of the subject can use the code. The second example was carried out to find the effect of changing the pressure supply (from 1-15 bar) on the load, flow and stiffness of the same bearing in the previous example. Figure 9 shows the results of these runs that were performed within a very short time (of less than 30 minutes). Whereas if we did the computations using the traditional method (hand calculations) we would need a very long time (many days), which is impractical.

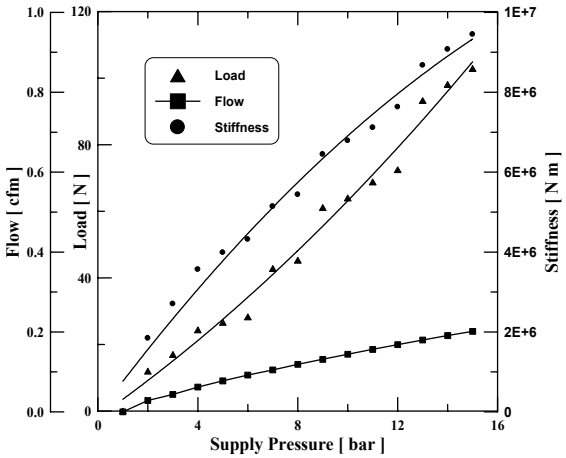

Fig. 9. The graphical results of the effect of supply pressure variance on Load, flow and stiffness.

Table 4: Numerical example of using the code.

Bearing dimensions and air properties:	R_o =37.5 mm	p_a=1e5 Pa
	R_i =30 mm	$\sqrt{\Re T} = 298.75$ m sec^{-1}
	p_s=7.1e5 Pa	μ=1.93e-5 N sec m^{-2}
Calculated dimensions	$R_c = \sqrt{R_o R_i} = 33.5$ mm	n=41
	a=0.2 mm	d=0.6 mm
	C=0.0125 mm	lc=0.08 mm
Governing dimensionless parameters	R_o/R_i=1.25	p_s/p_a=7.1
	σ =1.5	Λ_s=0.36
	The feeder hole volume ratio =0.056	
Dimensionless output: $\overline{W}$ $\overline{Q}$ $\overline{K}$ $\overline{B}$ are not shown as output by code		
Check list	n>n min	5e-3≤C≤2e-3
	Pneumatic Hammer, ok	Load, ok
Output parameters	W=43.105N	K=5.17e6 N m sec^{-1}
	Q=0.1065 cfm	B = Ignored

7. Conclusions

It must be emphasized that the use of this program is not a substitute for the solid understanding of basic principles of bearing design. It can, however, relieve the designer from the burden of performing many routine calculations and provide analytical capabilities far beyond those attainable using hand calculations or user-written subroutines. For these reasons, programs such as (OCFPAH) will rapidly become indispensable tools for industrial designers.

The frequent use of the new approach of the design of this important type of bearing with many distinguished characteristics proved that the proposed procedure was working very well. The new approach saves time, needs less experience and does the job accurately.Future work is planned to integrate this code with other related codes like radial bearings and rotor dynamics.

References

[1] B. Sternlicht, "Gas bearing turbomachinary". Trans. Of ASME, Journal of Lubrication Technology, Vol. 90**,** 1968, 665-679.
[2] AL-Ajlouni M., Studies of the rotating high speed separation systems, PhD Thesis, Cardiff, UK,1996.
[3] Gross W.A, Gas film lubrication. New York and London: John Wiley and sons, Inc, 1962.
[4] Ford GWK., Winfrith UKAEA. The place and scope of gas lubrication. In: Grassam NS, Powell, JW, editors. Gas lubricated bearings, London: Butterworths, 1964, 3-24
[5] Cheng HS. Hydrostatic thrust bearings. Design of gas bearings/ MTI/RPI manual. Latham, New York, 1966.
[6] Cheng HS. Basic relations. Design of gas bearings/ MTI/RPI manual. Latham, New York, 1966.
[7] DD. Fuller, "A Review of the state-of-the-Art for the Design of self-Acting Gas-Lubricated bearings". Trans. Of ASME, Journal of Lubrication Technology, Vol. 91**,** 1969, 1-16.
[8] Vohr JH. Restrictor flow. Design of gas bearings/ MTI/RPI manual. Latham, New York 1966.
[9] Lund JW. Dynamic performance and stability. Design of gas bearings/ MTI/RPI manual. Latham, New York, 1966.
[10] Johnson, RA. Miller and Freund's Probability and Statistics for Engineers. Upper Saddle River, USA: Prentice Hall, 2000.
[11] Hines WW, Montgomery DC. Probability and Statistics in Engineering and Management Science. New York and others: John Wiley and sons,1990.
[12] Dovore JL. Probability and Statistics for Engineering and Sciences. Fourth edition London: Duxbury Press, 2004.
[13] Montgomery D. C., Runger G. C. and Hubele N. F., Engineering Statistics. Fourth edition. New York and others: John Wiley and sons,2007.
[14] Montgomery D. C., Design and Analysis of Experiments. Sixth edition. John Wiley and sons, New York ,2005.

JJMIE

Volume 1, Number 2, Dec. 2007
ISSN 1995-6665
Pages 93 - 98

Jordan Journal of Mechanical and Industrial Engineering

Prospects of Energy Savings in the Jordanian Plastic Industry

A. Al-Ghandoor *[,a], I. Al-Hinti [b]

a Department of Industrial Engineering, The Hashemite University, Zarqa, 13133, Jordan
b Department of Mechanical Engineering, The Hashemite University, Zarqa, 13133, Jordan

Abstract

With the rapid and sharp rise in energy prices in Jordan, energy cost is becoming a value that cannot be ignored in the Jordan's industrial sector. However, there are still many practices adopted in industry that do not take energy efficiency as a prime consideration, but rather focus on immediate and direct savings in materials and machinery. This study examines potential opportunities of electrical energy savings in the Jordanian plastic industry. It demonstrates that electrical energy saving can be considered as a superior option to increase profit and competition within this sector. To achieve this purpose, detailed energy audits have been carried out for the most common plastic facilities in Jordan. An electrical energy conservation guideline is recommended and each recommendation is illustrated in terms of electrical energy savings, demand savings, cost savings, and payback period. A substantial annual electricity cost saving of 871,940 JD is reported in this study. This represents nearly 23% of the total plastic industry electricity bill with a payback period of less than 7 months. The contribution of electricity cost to the total value added can be reduced from 0.08 to 0.0616 (JD of electricity/JD of value added) if such recommendations are adopted.

Keywords: Energy savings; Electricity; Plastic industry; efficiency; Jordan;

1. Introduction

In non-oil producing countries where energy resources are scarce and production of electricity is very costly, energy conservation studies are of great importance. Jordan, unlike most other countries in the Middle East region, does not produce its consumed oil and is totally dependent on imported oil from neighboring countries. The annual fuel consumption has been rapidly increasing over the past few years. Therefore, it is an extremely important duty to reduce the energy consumption and search for alternative resources of energy.

The industrial sector represents approximately 23% of the total Jordanian energy consumption [1]. The primary building units of the industrial sector are the facilities it is comprised from. Therefore, analyzing these building units will definitely improve the overall energy situation of this sector. In recent years, concerns about energy consumption in Jordan have been growing, especially in the industrial sector, since the energy cost represents a significant percentage of the total value added in most industries. The importance of energy conservation in Jordan has been outlined by Kablan [2] and Akash et al. [3] and has been identified and estimated for different industries in different countries by Chan et al. [4], Markis et al. [5], Khan [6], Worrell et al. [7], and Fickett et al. [8]

Figure .1 shows the cost of electricity relative to the total value added of the most common products of the industrial sector in Jordan. As it is shown in the Fig. 1 plastic facilities use high rates of electrical energy consumption to maintain their productions. In fact, the plastic industry is ranked third among the most electrical energy intensive industries behind the non-metallic mineral, and mining and quarrying industries. In 2004, fuel and electricity bills of the Jordanian plastic industry were 4.589 million Jordanian Dinars (JD) [9]. In this industry, energy can be viewed as the most expensive and the most important form of inputs. At the same time, there are some primary energy end uses that are common among the plastic facilities: heaters, compressors, motors, lightings, HVAC, boilers, and chillers irrespective of the kind of products processed by the plastic facility .

The primary objective of this paper is to identify and evaluate opportunities for electrical energy conservation in the Jordanian plastic industry. This will be achieved through auditing the different types of Jordanian plastic facilities.

* Corresponding author. e-mail: ghandoor@hu.edu.jo

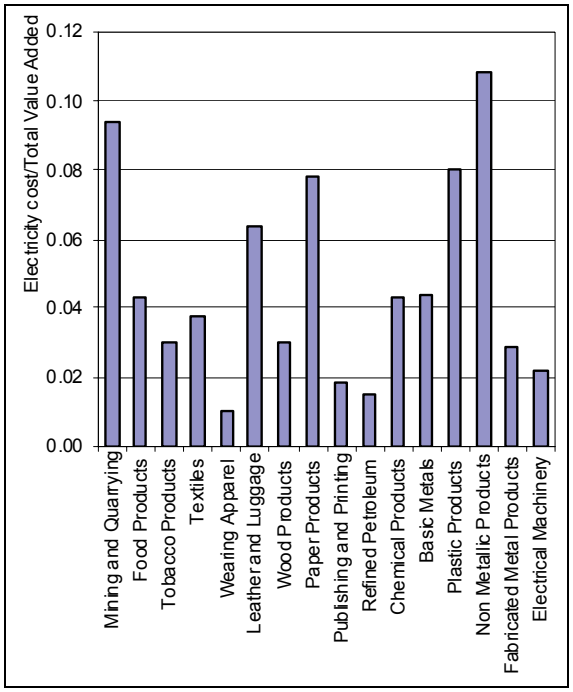

Figure 1: The cost of electricity relative to the total value added of the most common products of the industrial sector in Jordan.

The following four factors are considered when discussing energy conservation:

- Electrical energy savings (kWh)
- Electrical demand savings (kW)
- Electrical energy cost savings (JD)
- Payback period (month)

These factors will be quantified for the suggested recommendations throughout the paper.

2. Energy Consumption in Jordan

In 2005, Jordan's consumption of primary energy (crude oil and petroleum products, natural gas, renewable energy, imported electricity) amounted to 7.028×10^6 Ton Oil Equivalent (TOE) while the final energy consumption was 4.802×10^6 TOE. Final energy consumption in Jordan is mainly distributed between three major sectors: transportation, industrial, and residential. The distribution of final energy consumption among different sectors over the past five years is presented in Table 1, while a breakdown of electricity consumption among the different sectors is presented in Table 2 [1]. It can be seen from both tables that the industrial sector is the second largest consuming sector of final energy and electricity. The share of this sector has been nearly constant over the past few years at nearly 24% of final energy consumption and nearly 31% of the electricity consumption.

3. Plastic Industry in Jordan

Over the past two decades, the plastic industry in Jordan has witnessed a very fast growth as it can be seen in Figure .2, which shows the development of the number of facilities, employees and energy consumption relative to the base year of 1985. For example, in 1985, there were 58 facilities, and 1586 employees. Twenty years later, the industry has grown to more than 281 facilities and employed more than 5800 people [9]. Such enormous increase in the number of facilities and produced products has contributed to an increase in the indigenous energy and electricity demands. In 1985, the industry's energy consumption was 233 TJ compared to 506 TJ in 2004 [9].

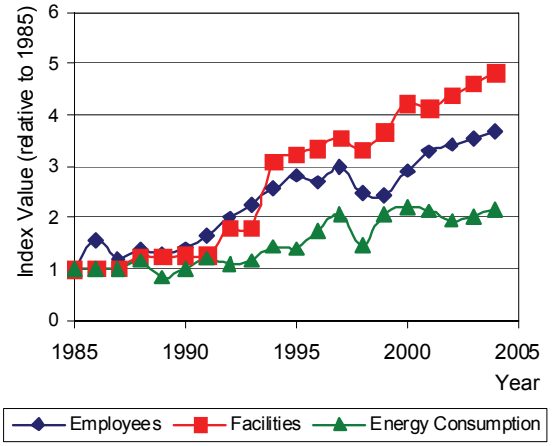

Figure 2: Development of the number of employees, facilities and energy consumption indices of the Jordanian plastic industry over the period 1985-2004.

Table 1: Sectoral distribution of the final energy consumption in Jordan during the period 2001-2005 (Thousand TOE) [1].

Year	Sector				Total
	Transport	Industrial	Household	Other	
2001	1411 (38.2%)	826 (22.4%)	849 (23.0%)	606 (16.4%)	3692 (100%)
2002	1435 (37.7%)	846 (22.2%)	868 (22.8%)	662 (17.4%)	3811 (100%)
2003	1495 (37.0%)	878 (21.7%)	945 (23.4%)	722 (17.9%)	4040 (100%)
2004	1693 (37.4%)	1034 (22.8%)	1007 (22.2%)	792 (17.5%)	4526 (100%)
2005	1779 (37.0%)	1159 (24.1%)	1060 (22.1%)	804 (16.7%)	4802 (100%)

Table 2: Sectoral distribution of electricity consumption in Jordan during the period 2001-2005 (GWh) [1].

Year	Sector						Total
	Household	Industrial	Commercial	Water Pumping	Street Lighting	Other	
2001	2110 (33.0%)	2024 (31.7%)	880 (13.8%)	982 (15.4%)	177 (2.8%)	219 (3.4%)	6392 (100%)
2002	2266 (32.8%)	2193 (31.8%)	971 (14.1%)	1044 (15.1%)	190 (2.8%)	236 (3.4%)	6900 (100%)
2003	2471 (33.7%)	2294 (31.3%)	1047 (14.3%)	1104 (15.1%)	201 (2.7%)	213 (2.9%)	7330 (100%)
2004	2745 (33.9%)	2479 (30.6%)	1190 (14.7%)	1261 (15.6%)	213 (2.6%)	201 (2.5%)	8089 (100%)
2005	2989 (34.3%)	2659 (30.5%)	1317 (15.1%)	1298 (14.9%)	248 (2.8%)	201 (2.3%)	8712 (100%)

The plastic industry in Jordan is mainly based on three manufacturing techniques: Extrusion, injection molding, and blow molding, in addition to some processes that

include combinations of some of these techniques. Hundreds of products are processed by the industry including: heating pipes, water pipes, strings, ropes, medicals cans, food and beverage cans, sheets, seals, grains, kitchen tools, molds, and bags. Table 3 shows the distribution of different plants that are associated with the most common plastic products [10].

Table 3: The distribution of plastic facilities according to processed products.

Type of product	Number of the facilities
Pipes	34
Ropes and strings	4
Medical containers	3
Sheets	5
Seals	15
Containers and Bottles	58
Granules	32
Kitchen tools	32
Food package	4
Plumping tools	8
Molds	5
Bags	61

4. Methodology

This paper will concentrate on analyzing the electrical saving opportunities since electricity forms about 83% of the total energy cost input. In order to do so, the distribution of input electrical energy among different end uses should be known. Such data and information are unavailable in Jordan, not only for the plastic industry, but also for most other industries since the collection and analysis of such data on a national scale is a long, difficult and costly process. However, a survey on a narrow scale aiming at collecting relevant consumption data can be useful in bringing a good understanding of the characteristics of the electrical energy consumption in the plastic industry. For this reason, ten facilities of different products (such as: pipes, containers and bottles, granules, plumping tools, and kitchen tools) in Amman were visited and investigated. During the site visits, relevant measurements for various devices (motors, compressors, heaters, etc.) were taken as a part of energy survey. Also, several interviews with specialists in the plastic processing industries were conducted. This enabled the identification of potential opportunities of electricity savings, quantification of such savings, and the cost incurred for achieving them.

5. Electrical Energy End Use Model

In order to determine the plastic industry's overall electrical energy conservation, the proportion of electrical energy consumed for each end use process within the industry should be known. Fortunately, irrespective of the kind of facility, the manufacturing techniques it uses, or the type of products it processes, there are six primary end uses of electricity: Space conditioning, lighting, motors, compressors, heating, and cooling. A model in the form of an electrical energy flow diagram that explains how total electrical energy input is distributed and routed to different categories of end-uses has been developed as shown in Figure 3. This model is based on the data gathered during the site visits for the ten facilities. This paper will concentrate on motors, compressors, and heaters since they account for approximately 75% of the total electrical energy consumption.

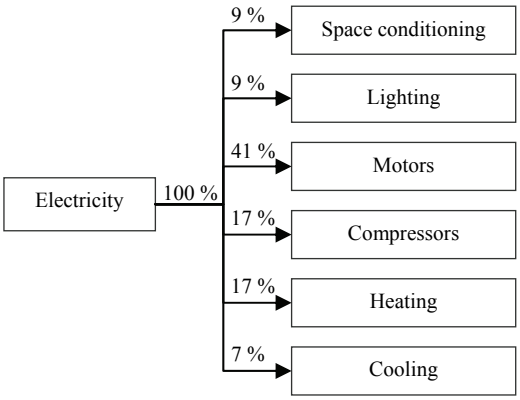

Figure 3: End use model for Jordanian Plastic Industry

To start the analysis, the total electrical energy input to the Jordanian plastic industry in terms of a physical unit (kWh for example) should be known. Although such data are not available, the total annual cost of the electricity input to plastic industry was reported as 3,803,700 JD in 2004 [9]. The total physical electricity input (kWh) to the plastic industry can be estimated as follows:

$$\textit{Total physical electricity input (kWh)} = \frac{\textit{Total cost of actual consumed electricity}}{\textit{Electricity cost of kWh}} \quad (1)$$

The total reported cost of electricity (RCE) includes three types of costs: cost of actual electricity consumption (ACE), the power factor penalty (PP) applied to medium and large facilities and the peak load penalty (DP) applied to medium and large facilities. In order to estimate the total physical electricity input (kWh), the total cost of actual consumed electricity (ACE) should be known. Therefore, the penalties due to power factor and peak load should be taken out from the total reported electricity cost. The total cost of actual consumed electricity can thus be estimated as follows:

$$ACE = RCE - PP - DP \quad (2)$$

The power factor penalty is applied to medium and large facilities that have power factor less than 0.85. The average annual power factor penalty for each medium and large facility was reported as 2,250 JD [11]. There are about 43 medium and 13 large plastic industrial facilities in Jordan. Therefore, the annual power factor penalty can be estimated as 126,000 JD. The peak load penalty is applied also to medium and large facilities. This is charged for the maximum power consumption (kW) that occurs for continuous thirty minutes during the peak time (from 5:00 PM to 8:00 PM during winter and 7:00 PM-10:00 PM

during summer) within the month. It has been estimated that the electrical power of medium and large facilities during the peak time is 250 kW and 400 kW respectively [11]. Therefore, the total annual charges that are due to peak load penalty can be estimated as 543,210 JD. Applying these figures in Eqution. (2), the total annual cost of actual consumed electricity can then be found equal to 3,134,490 JD.

In order to estimate the total physical electricity consumption (kWh), the cost of each kWh should be known. However, this cost depends upon whether the facility is small, medium, or large. Also, it depends whether the consumption occurs during the day or night periods. In 2004, the weighted average cost of each kWh for small, medium, and large facilities are 0.0380, 0.0320, and 0.043 JD/kWh, respectively. The actual electricity consumption (kWh) distribution between small, medium, and large facilities is estimated as 40%, 48%, and 12%, respectively [11]. The weighted electricity cost of the small, medium, and large facilities can be estimated as 0.0357 JD/kWh. Using this value with the total annual cost of actual consumed electricity, the total annual physical electricity input can finally be calculated and found equal to 87,809 MWh.

6. Energy Conservation Opportunities

This section presents the most common recommendations of electrical energy conservations that have been found in the visited ten facilities and can be applied in a typical plastic facility. The analysis will be shown in detail for one recommendation (replacement of energy inefficient motors with efficient ones) while summaries for other recommendations will be given.

6.1. Improvement of the Electrical Power Factor of the Facility:

The average power factor in this sector has been estimated as 0.7, which is considered low in terms of industry standards. Power factor can be an important aspect to consider in an AC circuit; because any power factor less than unity means that the circuit's wiring has to carry more current than what would be necessary with zero reactance in the circuit to deliver the same amount of (true) power to the resistive load. Hence, the power factor of the generator can be improved by addition of capacitors parallel to the line. As discussed earlier, the total annual penalty that is due to power factor has been estimated as 126,000 JD. By adding the appropriate capacitor, the charged amount will be reduced to zero with an average total cost of 3500 JD/facility. The payback period will be approximately 7 months.

6.2. Replacement of Energy-Inefficient Motors:

For the visited facilities, currently in Jordan, the demand electricity costs are 2.4 and 3.05 JD/(kW.mo) for large and medium facilities respectively. It has been found that the average current operating efficiency of a typical motor is 78%. This low efficiency is due to the common practice by many facilities to simply rewind an existing motor when it burns out rather than purchasing a high efficiency replacement motor. However, a rewound motor is typically less efficient than a new one. The loss of efficiency is due to the age of the failed motor and degradation of its stator core during failure, or as a result of the rewind process. The typical efficiency loss ranges from 1% to 5% for each rewinding process [12].

The energy savings, *ES*, and energy cost savings, *ECS*, for replacing an old motor with a new high efficiency motor, can be estimated as follows:

$$ES = ECM\left(\frac{1}{E_c} - \frac{1}{E_p}\right) \tag{3}$$

$$ECS = ES \times cost\ of\ electricity \tag{4}$$

Where *ECM* is the electrical energy consumed by motors (can be estimated from figure 3 as 36,001.7 MWh), E_p the efficiency of proposed high efficiency replacement motor (assume 90%), and E_c the efficiency of the current motor (assume 78%). As estimated ealier, the weighted average electricity charge is 0.0357 JD/kWh, the annual electrical energy savings, *ES*, and the resulting annual electrical energy cost savings, *ECS* will be 6,154.1 MWh and 219,703 JD, respectively.

Demand savings will result from using a smaller capacity load per unit time. The demand savings by replacement of inefficient motors with energy efficient motors can be derived as:

$$EDS = \frac{SF \times ES}{AOH} \tag{5}$$

Where *EDS* is the electricity demand savings, *SF* is the sharing factor of electrical energy consumption for medium and large facilities (0.6), *AOH* is the annual operating hours. The average annual operating hours are estimated to be 6,257 h. The annual demand cost savings *(EDCS)*, can be estimated from

$$EDCS = DC \times EDS \times 12 \tag{6}$$

Where *DC* is the demand cost (estimated on the basis of a weighted average of medium and large facilities equal to 2.92 JD/(kW.month)). The resulting demand savings and annual demand cost savings are then 590.13 kW and 20,678 JD, respectively. In average, the payback period will be approximately 9 months.

6.3. Installation of Variable Frequency Drives (VFD):

In many industrial environments, the application of variable speed control is cost effective. Energy savings result from reduced power consumption by the motors. As the system power requirements are reduced, the power consumed by the equipment can be reduced by an amount significantly greater than can be achieved with the existing controls. For example, in the case of pumps, flow is often controlled (throttled) by valves, which increase the pump head and reduce the flow rate. In the Plastic industry, VFDs can be applied to injection and blow molding

motors, pumps, and compressors. It is estimated that a saving of 15-20% of the motor electrical energy can be achieved if such controllers are adopted. Assuming an average saving of 17.5%, the annual electrical energy savings and electrical energy cost savings will be 6,300.3 MWh and 224,921 JD, respectively. The resulting demand savings and annual demand cost savings are 604.15 kW and 21,170 JD, respectively. In average, the payback period will be approximately 9 months.

6.4. Repair of Compressed Air Leaks

The cost of compressed air leaks is the energy cost to compress the volume of lost air from atmospheric pressure to the compressor operating pressure. The amount of lost air depends on the line pressure, the compressed air temperature at the point of the leak, the air temperature at the compressor inlet, and the estimated area of the leak. The leak area is usually detected depending on the sound and feeling of air flow from the leak. The detailed equations to estimate the air leaks are given by Shapiro [13]. An alternative method to determine total losses due to air leaks is to measure the time between compressor cycles when all air operated equipment are shut off. It is estimated that a saving of 15-20% of the compressor electrical energy can be achieved if air leaks are eliminated. Assuming an average saving of 17.5%, the annual electrical energy savings and electrical energy cost savings will be 2,612.3 MWh and 93,260 JD, respectively. The resulting demand savings and annual demand cost savings are 250.50 kW and 8,778 JD, respectively. In general, implementation involves one or two of the following: replacement of couplings and/or hoses, replacement of seals around filters, shutting off air flow during lunch or break periods, and repairing breaks in lines, etc. The payback period will be approximately 10 days.

6.5. Avoiding Poor Practices of Compressed Air Usages:

During the site visits, several poor practices of compressed air usage have been noticed. For examples: Several companies use the compressed air to cool the extruded pipes or some devices such as motors, while others use it for cleaning purposes. Since the use of compressed air is either for cooling or cleaning purposes, air at sufficient flow rates can be adequate for these purposes. This can be done by blowers which use much less energy. It was estimated that a saving of 10-20% of the compressor electrical energy can be achieved by avoiding such poor practices. Assuming an average saving of 15%, the annual electrical energy savings and electrical energy cost savings will be 2,239.16 MWh and 79,937 JD, respectively. The demand savings and annual demand cost savings are then found to be equal to 214.72 kW and 7,524 JD, respectively. Implementation costs include purchasing blowers to replace the compressed air. The payback period will be approximately 1 month.

6.6. Insulation of the Extrusion, Injection, and Blow Molding Machine Heaters:

During the site visits, it was found that some areas of the extrusion, injection, and blow molding machines are not well insulated. This results in heat losses and associated energy costs. These areas of heat losses were studied and carefully calculated using the equations of heat transfer from bared surfaces [14]. The energy savings were estimated to be 10-14% of the total input electricity to heaters. Assuming an average saving of 12%, the annual electrical energy savings and electrical energy cost savings will be 1,791.3 MWh and 63,950 JD, respectively. The resulting demand savings and annual demand cost savings are then 171.77 kW and 6,019 JD, respectively. Implementation costs include purchasing of insulation material in addition to labor costs with a payback period of approximately 1 month.

6.7. Overall Energy and Cost Savings:

After implementing the previous recommendations for all plastic processing facilities in Jordan, the total annual electrical energy savings, the electrical demand savings, and the total annual cost savings are estimated to be equal to 19,097.2 MWh, 1,831.27 kW, and 871,940 JD, respectively. The average payback period will not exceed 7 months.

7. Conclusions

An analysis and estimation of the potential electrical energy saving opportunities in the plastic industry in Jordan was carried out. The results revealed that there is a large room of improving the efficiency of electricity consumption in this industry with remarkable energy cost savings. The total electricity cost savings represent nearly 23% of the industry's total annual electricity bill. The contribution of electricity cost to the total value added can be reduced from 0.08 to 0.0616 (JD of electricity/ JD of value added). This can be considered as an effective option for increasing profit and competition within this sector.

Having listed all the different remedies that can lead to electrical energy conservation, the implementation of these recommendations is very crucial for the plastic industry in Jordan to reach the desired cost savings. Such study can be considered as the corner stone in achieving national energy savings among all Jordanian industries. Therefore, it is highly recommended to carry out such studies and analyses for other Jordanian industries.

References

[1] Ministry of Energy and Mineral Resources. Annual Report Amman, Jordan, 2006.

[2] Kablan M. "Energy Conservation Projects implementation at Jordan's Industrial Sector: A Total Quality Management Approach". Energy, Vol. 28, No. 15, 2003, 1533-1543.

[3] Akash B., and Mohsen M. "Current Situation of Energy Consumption in the Jordanian Industry". Energy Conversion and Management, Vol. 44, No. 9, 2003, 1501-1510.

[4] Chan D., Yang K., Hsu C., Chien M., and Hong G. "Current Situation of Energy Conservation in High Energy-Consuming Industries in Taiwan". Energy Policy, Vol. 35, No. 1, 2007, 202-209.

[5] Markis T., and Paravantis J. "Energy Conservation in Small Enterprises", Energy and Buildings, Vol. 39, No. 4, 2007, 404-415.

[6] Khan A. “Electrical Energy Conservation and Its Application to a Sheet Glass Industry”. IEEE Transactions on Energy Conversion, Vol. 11, No. 3, 1996, 666-671.

[7] Worrell E., Beer J., Faaji A., and Blok K. "Potential Energy Savings in the Production Route for Plastics". Energy Conversion and Management, Vol. 35, No. 12, 1994, 1073-1085.

[8] Fickett A., Gellings A., and Lovins A. “Efficient Use of Electricity”. Scientific American, Vol. 263, No. 3, 1990, 64-68.

[9] Department of Statistics. "Statistical Yearbook 2004: Industry Survey". Amman, Jordan, 2005.

[10] Amman Chamber of Industry. "Industrial Directory". Amman, Jordan. See also: www.aciorg.jo, 2007

[11] Ministry of Energy and Mineral Resources. "Preliminary Survey of Energy Consumption in the Industrial Sector 1996", Final Report, Amman, Jordan, 1998

[12] De Almeida A., Elliot N., Greenberg S., Katz G., Nadel S., and Shepard M. "Energy Efficient Motor Systems: A Handbook on Technology, Program, and Policy Opportunities". Second edition, ACE: Washington, DC, 2002.

[13] Shapiro A. "The Dynamics and Thermodynamics of Compressible Fluid Flow". Ronald Press, N.Y., 1953.

[14] Incropera F.A. and DeWitt D.P. "Fundamentals of Heat and Mass Transfer". Sixth edition. John Wiley and Sons, 1996.

JJMIE

Volume 1, Number 2, Dec. 2007
ISSN 1995-6665
Pages 99 - 104

Jordan Journal of Mechanical and Industrial Engineering

On Three-Dimensionality of Turbulent Buoyant Channel Flow

Osama A. El-Samni *

Department of Mechanical Engineering, The University of Alexandria, El-Chatby, Alexandria 21544, Egypt

Abstract

A three-dimensional buoyancy-driven turbulent boundary layer is generated in fully developed turbulent channel flow. Setting the buoyancy forces perpendicular to the mean flow direction and using high Grashof number result in strong cross flow which is expected to have a similar influence to that of the previously studied pressure- and shear-driven three-dimensional turbulence boundary layers (3DTBLs). The present buoyancy-driven configuration has the advantage of being in equilibrium and three-dimensional from inception. Few issues are presented and discussed in order to give better understanding of the underlying physics associated with buoyancy-induced 3DTBL flows. The characteristics of the resulting 3DTBL are examined in comparisons with the available data in the literature. Reduction of the structure parameter A_1 (defined as the ratio between the total Reynolds shear stress to twice the turbulent kinetic energy TKE) is noticed in the edge of the inner layer which is attributed to the reduction of both Reynolds shear stress and turbulent kinetic energy. Explanation for such reductions is given by examining the changes in coherent structures due to buoyancy effect. Comparisons of some relevant quantities used in turbulence modeling with those of 2DTBL flow reveal the difficulty of establishing a universal model for a satisfactory 3DTBL flow prediction.

Keywords: Buoyancy; Channel flow; Turbulence; Direct numerical simulation; 3DTBL;

1. Introduction

Buoyancy forces play a significant role in various industrial equipment which deals with heat exchange. The effects of buoyancy should be taken into account in the optimum design of such equipment. One of the issues that has not been covered in detail is the flow three-dimensionality generated by buoyancy. In this specific case, the three-dimensionality takes place when the gravity vector is parallel to the duct walls (mainly in case of vertical walls) but perpendicular to the mean flow direction. Lateral motions are generated causing the flow to skew in the transversal direction. Consequently, all Reynolds shear stresses and heat flux components become non-zeros. The difficulty of dealing with 3DTBL flows arises from poor predictions of the flow velocities with the current turbulence models which in turn lead to poor predictions of the thermal field. Most of the commercial software packages dealing with thermal equipment design are using turbulence models based on 2DTBL assumption. There is still great need to assess and improve such turbulence models to deal with three-dimensional flows in general and more specifically with buoyant flows. Therefore, understanding the underlying physics of three-dimensional buoyant flow is essential before improving the relevant models.

3DTBL flows have been explored extensively in laboratories, to our knowledge, without imposing buoyancy forces. The three-dimensionality is likely to occur in a nominally 2D flow by imposing a cross-stream pressure gradient which skews the flow in the near-wall region more strongly than near the free stream direction. Different techniques have been used in pressure-driven flows experiments to generate a 3DTBL. Schwarz and Bradshaw [1-3] and Flack [4] used a flat end-wall of constant area rectangular duct including a 30º bend around its mid point. Bradshaw and Pontikos [5] simulated an infinite swept wing by a deformable roof of a duct and measurements were done on its flat floor. Ölçmen and Simpson [6] used a wing-body junction type which is mounted vertically on a flat wind-tunnel wall. Compton and Eaton [7], Anderson and Eaton [8], and Eaton [9] generated their 3DTBL by constructing upstream facing wedges of different angles. Skewing the flow can also be developed by shear force when a wall moves in a direction different from the main flow direction. An example of the shear-driven flows is the experiments of Littell and Eaton [10], Chiang and Eaton [11] and Kang et al. [12] of flow on a free rotating disk.

Direct numerical simulation (DNS) has become a vital tool in 3DTBL flows discovery. DNS can simulate 3DTBL cases which cannot be realized experimentally. For example, Spalart [13,14] simulated turbulent boundary layer on a flat plate. He showed that when the free-stream

* Corresponding author. e-mail: elsamni@gmail.com

velocity vector rotates at constant angular rate, the resulting mild skewing of the velocity in this configuration resembles turbulent Ekman layer [15]. Moin et al. [16] applied a spanwise pressure gradient in a 2D channel flow. Non-equilibrium simulations were done by Coleman et al. [17, 18] by imposing mean irrotational deformations in the streamwise-spanwise planes which can mimic a favorable or an adverse pressure gradient. Le et al. [19] imposed an impulse spanwise movement to the lower wall of a turbulent channel flow. Wu and Squires [20] used large eddy simulation to predict a three dimensional equilibrium boundary layer by rotating the free-stream velocity over an infinite plate which resembles the growth of TBL over a rotating disk.

The present study tries to give more insight to the three-dimensionality induced by buoyancy forces. Various structural parameters which are usually used in describing 3DTBL flows will be compared with those of pressure- and shear-driven 3DTBLs. Explanation for the reduction of the structure parameter A_1 will be given in terms of the changes of the near-wall coherent structures. Some modeling issues will be covered by comparing the relevant quantities with those of 2DTBL flows.

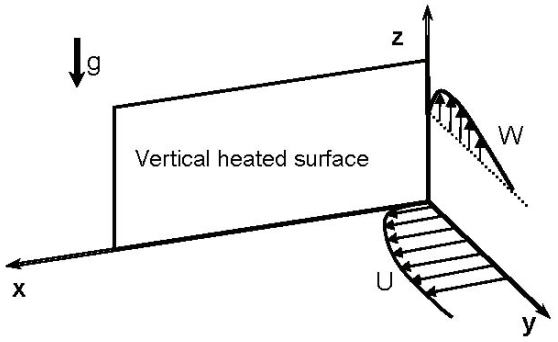

Fig. 1 Sketch of 3DTBL driven by buoyancy.

2. Numerical Approach

Vertical channel with two differentially heated walls are used for the present simulation in which the air flows horizontally and thus buoyancy vector is perpendicular to the mean flow direction. The focus will be on the heated wall as shown in.Figure .1. The temperature difference ΔT is sufficient to account for the buoyancy effect. The continuity, Navier-Stokes equations and the energy equation are solved using Pseudospectral code for a channel flow. It eliminates the pressure by transforming the Navier-Stokes equations to the vorticity-normal velocity formulation. Fourier series have been used for expanding the resolved variables in the homogenous directions while Chebyshev polynomial expansion is employed in the wall-normal direction. The driving pressure gradient is adjusted to keep constant mass flow rate in the x-direction. The channel width is 2δ and the computational domain has the dimensions $5\pi\delta \times 2\delta \times 2\pi\delta$ with grid points 128×129×128 in x, y, and z directions, respectively. The flow is assumed fully developed so that the periodic boundary conditions are applied in x and z-directions. The no-slip boundary conditions for the flow field and the isothermal boundary conditions with zero fluctuations are applied at both walls. Further details about the numerical approach and the verification of the code can be found in El-Samni et al. [21]. The friction Reynolds number $Re_\tau = u_\tau \delta / \nu$ is fixed 164, where u_τ is friction velocity; d is half the channel depth and n is the kinematic viscosity. Grashof number, defined by $g\beta\Delta T(2d)^3/n^2$, is set to 4×10^6, where g is the gravitational acceleration and β is thermal expansion coefficient..

3. Results and Discussions

The present configuration is advantageous in terms of the simplified statistics compared with other 3DTBL flows. The equilibrium status of the flow and the homogeneity in the planes parallel to the stream wise-span wise directions make the quantities under consideration changing only in the wall-normal direction y. The quantities presented here are normalized by the friction velocity u_t^* deduced from the total mean velocity $Q = (U^2 + W^2)^{1/2}$ and n unless otherwise stated and are superscripted by +. Some quantities may be normalized by the momentum thickness q. Capital letters and over-bar denote the time and spatial average over $x-z$ planes and prime indicates the fluctuation component which may be dropped for clarity.

3.1. Polar Plot

With the above mentioned configuration, the buoyancy forces induce anti-symmetric mean span wise velocity (W) giving positive values near the heated wall as sketched in Figure .1

The peak of w occurs at y^+~26 which is smaller than those values observed in typical 3DTBL flows; see for example Wu and Squires [20]. Polar plot of the cross-flow velocity profile is shown in Fig. 2 where both the stream wise and span wise mean velocity components are normalized by the centerline velocity U_C.

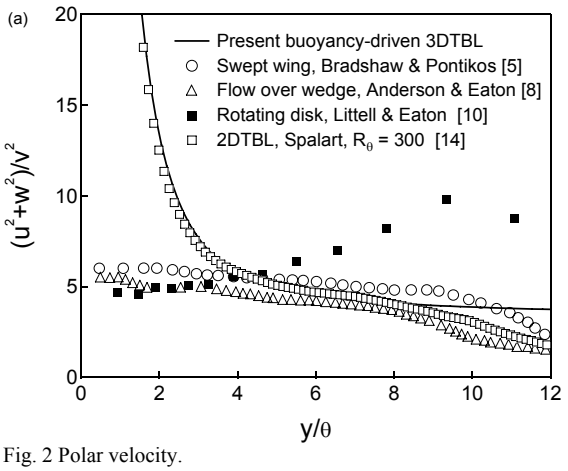

Fig. 2 Polar velocity.

The profile is compared with the 3DTBL data of the 30° bend [4] and the rotating disk [10] aiming at showing the relative magnitudes of the induced spanwise mean velocities in different 3DTBL flows. The apex of the

triangle reaches a maximum value of around 0.34. The peak value shown in the polar plot is larger than the value observed in the 30° bend of Flack [4] whose peak was around 0.25 and that of the rotating disk of Littell and Eaton [10] which approached 0.11. It can be noted also that the slope near the channel center is steeper than those observed in the experiments of 3TDBL in the outer layer. This difference in the profile shape and the peak of the polar plots can be attributed to the non-vanishing strain resulted from the anti-symmetric trend of W in the present study. In most of the 3DTBL flows, W in the outer layer vanishes resulting in very small $\partial W/\partial y$.

3.2. 3DTBL Structural Parameters

In this section, several structural parameters which are generally used in characterizing 3DTBLs are deduced from the statistical quantities presented in El-Samni et al. [21]. Of those parameters is the ratio of the wall-parallel normal stresses to the vertical normal stress, $(u'^2+w'^2)/v'^2$ which can be a measure of the turbulence anisotropy. Comparisons with data of swept wing of Bradshaw and Pontikos [5], flow over wedge of Anderson and Eaton [8], rotating disk of Littell and Eaton [10], and Spalart [14] are presented in Fig. 3(a). Due to the continuity constraint at the wall, v is very small in the vicinity of the wall and consequently $(u'^2+w'^2)/v'^2$ estimated from numerical simulation of Spalart [14] and the present simulation are two orders of magnitude larger than those of the experiments mentioned above. In the range $4<y/\theta<8$, the experiments of Littell and Eaton [10] and Bradshaw and Pontikos [5] show similar flatten profiles around the same value of the present study, between 3.8 ~ 5. At the outer edge of the boundary layer, $(u'^2+w'^2)/v'^2$ approaches a value 2, the isotropic state for most of 3DTBL flows. However, in the present study it reveals a value around 3.6 showing high anisotropy in the core region due to the large increase of $w'w'$. Rotating disk [10] gives lower value of $(u'^2+w'^2)/v'^2$ near the wall and increases in the far field with increasing the wall distance y. This trend is opposite to the present 3DTBL buoyant channel trend which starts very high at the wall and decreases with increasing y.

Another relevant parameter is the ratio of the wall-normal stress to the total shear stress magnitude $v'^2/[(u'v')^2+(v'w')^2]^{1/2}$. The significance of this parameter was deduced from its trend in 2DTBL flows. In 2DTBL, $\overline{u'v'}$ is proportional to $\overline{v'^2}$. If such correlation exists in a 3DTBL flow, a simple relationship between the two quantities may reduce the number of unknowns in the turbulence model. In Fig. 3(b), a plateau profile in the range $50<y^+<250$ can be noticed which resembles those of Spalart [14] and that of Compton and Eaton [7] but with higher values. In the inner layer, the profile is close to those of 2DTBL flows of Spalart [14]. However, in contrast to both Reynolds numbers of the 2DTBL of Spalart[14], this parameter does not show sharp increase in the outer layer due to the increased total shear stress $[(u'v')^2+(v'w')^2]^{1/2}$ in the core region. The structure parameter A_1, defined by $[(u'v')^2+(v'w')^2]^{1/2}/k$, has been widely investigated in most of the previous 3DTBL flows. In general, three-dimensionality results in reduction of A_1 than its value in 2DTBL of around 0.15. In Fig. 3(c), A_1 is plotted in comparison with other numerical and experimental results. Reduction of A_1 at $y^+<120$ is observed in the present study in accordance with the reduction revealed in 2DTBL of Spalart [14] at Re_q =1410, the bend flow of Flack [4], and the rotating disk of Wu and Squires [20] at $Re_t \sim 840$. However, at $y^+>120$, A_1 increases. Although turbulent kinetic energy increases in the outer layer, still A_1 reveals higher value which indicates the efficiency of the flow to generate shear stress in the core region of the channel. This can be attributed to the nearly constant mean strain dW/dy across the channel core in the present case.

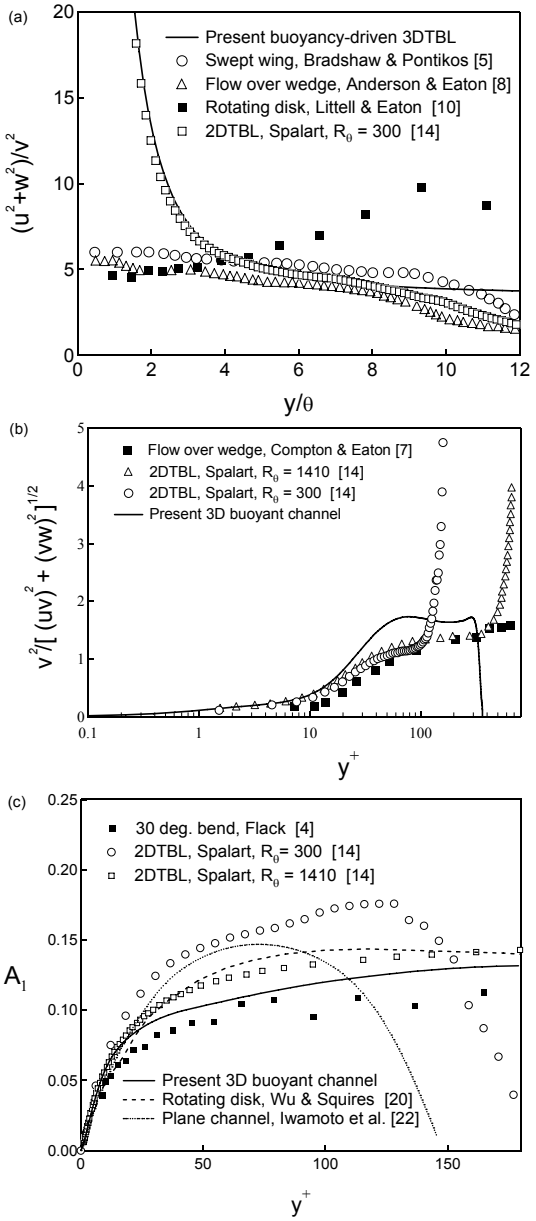

Fig. 3 Turbulence structures; (a) $(u'^2+w'^2)/v'^2$; and (b) $v'^2/[(u'v')^2+(v'w')^2]^{1/2}$; and (c) A_1.

The present 3DTBL buoyant flow resembles the rotating disk flow. Both are three-dimensional from inception and have their peaks of the spanwise velocity W in near-wall region. Although they show reduction of A_1, their anisotropy behaviors are different as shown in Fig. 3. This inconsistency, even between similar 3DTBL flows, reveals again the difficulty of proposing a universal discreption of 3DTBLs in the inner and outer regions.

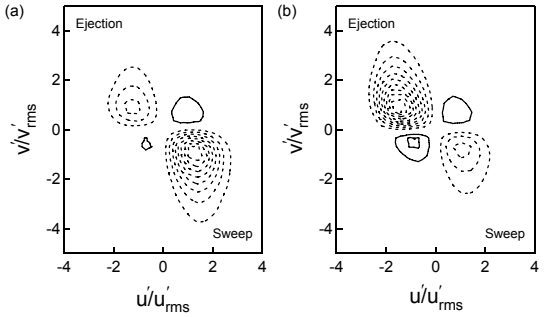

Fig. 4 JPDF of u' and v' at $y^+ \sim 12.5$: (a) weighted with positive w'_x ; (b) weighted with negative w'_x .

3.3. Changes of Coherent Structures

Several studies have tried to investigate the effects of three-dimensionality on the near-wall structures aiming at explaining the responsible mechanism of Reynolds shear stress reduction. Littell and Eaton[10], Kang et al.[12] and Wu and Squares[20] showed that cross flow reduces the ability of positive streamwise vortices to produce strong ejections ($u'<0, v'>0$) while weakening the ability of the negative ones to produce strong sweeps ($u'>0, v'<0$). In order to examine this hypothesis, the joint probability density function (JPDF) weighted by positive and negative streamwise vortices is performed and plotted in Fig. 4(a) and (b), respectively. This is performed at the height where both sweep and ejection events are of equal contribution to Reynolds shear stress $-\overline{u'v'}$ which is found to be at $y^+ \sim 12.5$. In 2DTBL case, the contours of the weighted JPDF are anti-symmetry in the diagonal connecting the 2nd and 4th quadrants. Clear agreement with the above claim can be seen in the Fig. 4 where positive w'_x is associated with weak ejections and negative w'_x is associated with weak sweeps. Two-point velocity correlation R_{uv} commonly defined by $R_{uv}(r_z) = \overline{u'(z)v'(z+r_z)}/u'_{rms}v'_{rms}$ is plotted in **Fig. 5** at the same height of that used in Fig. 4. However, there exists a strong dip in the negative separation in agreement with Littell and Eaton[10] and Kang et al.[12]. This asymmetry of the correlation coefficient implies that the strength of positive and negative vortices is not statistically equivalent. In other words, if both kinds of vortices are weakened with the same degree, the correlation R_{uv} should be symmetry around $r_z = 0$.

Decomposition of RMS of ω'_x based on their signs can verify the difference of strength of each kind of vortices. Kim et al. [23] estimated roughly a measure for the size and strength of vortices based on the peaks location of ω'_x . In **Fig. 6**(a), the positive vortices appear stronger than the negative ones since the later have weaker peak and the spacing between its local peaks becomes wider. Another verification is performed **Fig. 6**(b), where the number of events corresponding to $|w'_x| > 2\, w'_{x,rms}$ is estimated for long time of integration. In 2DTBL, the number of positive and negative vortices exceeding any threshold should be identical as long as the two vortices are symmetry. However, it can be seen that at $y^+ \sim 20$ the positive ω'_x has a clear peak in the time that negative w'_x has a minimum. The location $y^+ \sim 20$ refers to the centers of vortices [23].

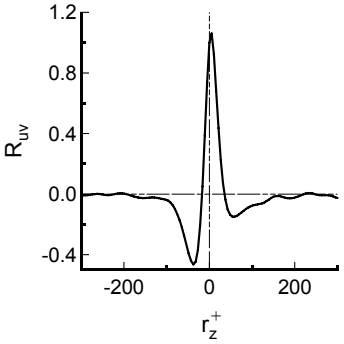

Fig. 5 Correlation coefficient at $y^+ \sim 12.5$.

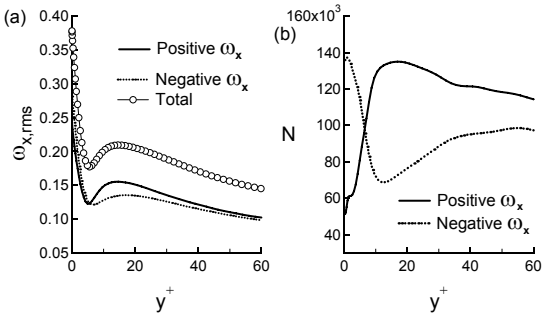

Fig. 6 (a) Vorticity decomposition; (b) number of strong vorticity RMS events

3.4. Modeling Issues

The above mentioned structural parameters are used in deriving various constants of the k-ε model. More derived quantities of interest to Reynolds-averaged modeling are computed in this section. It was shown by El-Samni et al. [21] that there is a lag between the shear stress and the mean velocity gradient vectors which makes restriction on using isotropy eddy viscosity assumption in turbulence modeling. A verification of their claim can be checked out by looking at the eddy-viscosity ε_x and ε_z in the stream wise and span wise directions:

$$\text{where } \varepsilon_x = \frac{-\overline{u'v'}}{\partial U/\partial y} \text{ and } \varepsilon_z = \frac{-\overline{v'w'}}{\partial W/\partial y}$$

In most of the 3DTBL flows studied so far, the eddy viscosity is not isotropic which means that $e_x \neq e_z$. This inequality has made unrealistic predictions of 3DTBL

flows using turbulence models based on the isotropy eddy-viscosity assumption. As shown in Fig. 7(a), ε_x matches with the 2DTBL values in near wall region while it departs substantially in the outer layer. ε_z oscillates from negative to positive at y^+~26 where the dW/dy changes its sign. Shown in Fig. 7(b) is the ratio $\varepsilon_x/\varepsilon_z$ which is denoted as the anisotropy factor N_e. Its value is far from unity in most of the channel depth in agreement with values obtained in other 3DTBL [6, 7].

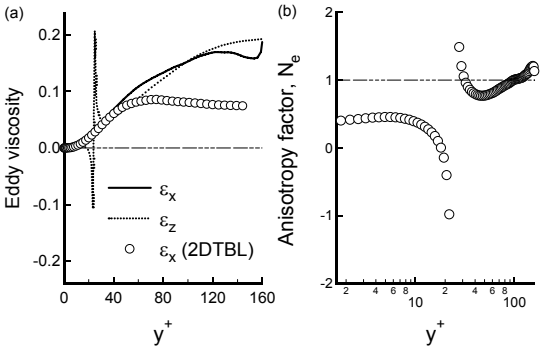

Fig. 7 Eddy viscosity (a); the anisotropy factor Ne.

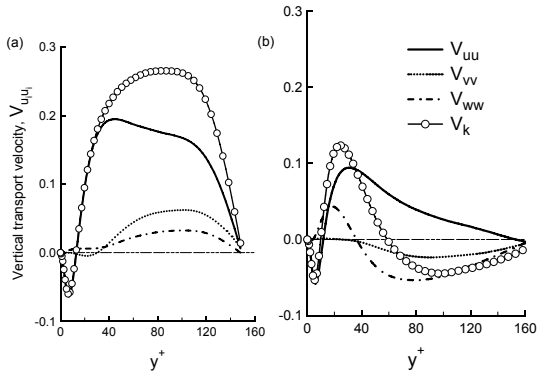

Fig. 8 Vertical transport velocities: (a) 2DTBL; (b) 3DTBL.

The effect of turbulence to transport turbulent kinetic energy can be expressed as an effective vertical transport velocity which is the sum of the three normal Reynolds stresses transport velocities:

$$V_k = (\overline{u'^2v'} + \overline{v'^3} + \overline{w'^2v'})/k$$

These triple correlations are commonly used in the transport equations of the normal Reynolds stresses. In near wall region, turbulent kinetic energy is transported away from the wall similar to 2D and 3DTBL flows as shown in **Fig. 8**(a,b). The major changes due to the buoyancy effect can be seen in the outer layer ($y^+ > 30$) in which V_k becomes negative in contrast to the 2DTBL profile and also to other 3DTBLs [1, 2, 5] and [8]. That is due to the change of transport direction of both V_{vv} and V_{ww} as shown in **Fig. 8**(b).

The triple products used in the closure of transport equations of Reynolds shear stresses $-u'v'$ and $-v'w'$ are shown in **Fig. 9**. The growth of $w'v'^2$ can be seen easily with comparable values to the primary triple product $u'v'^2$. The appearance of local peaks in $u'v'^2$ indicates the necessity to adjust turbulence models dealing with local shear stress gradient rather than the local shear stress values.

Last issue to be addressed is the pressure-strain correlation which is responsible for redistributing TKE among the velocity components and its trace should vanish. As shown in **Fig. 10**, the energy is redistributed from u and v to w component in near-wall region of both 2D and 3DTBL but with larger contribution from v in the existence of buoyancy forces which enhance the eruption of plumes of hot fluid from the surface. In contrast to 2DTBL, the buoyancy modifies the redistribution of TKE in the outer layer so that the energy is redistributed from w to both u and v as shown in **Fig. 10**(b). Moin et al. [16] observed reduction of the pressure-strain due to the flow three-dimensionality in contrast to the present findings. This discrepancy reflects the difficulty to propose a reasonable assumption for the pressure strain term in turbulence models.

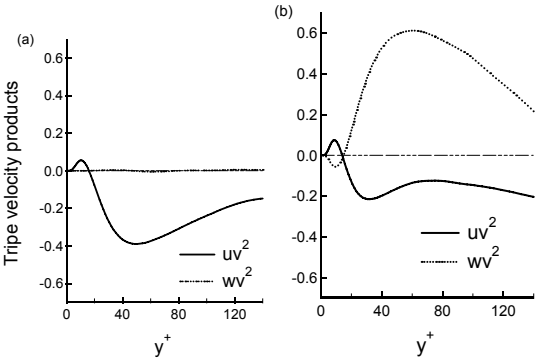

Fig. 9 Triple velocity products: (a) 2DTBL; (b) 3DTBL.

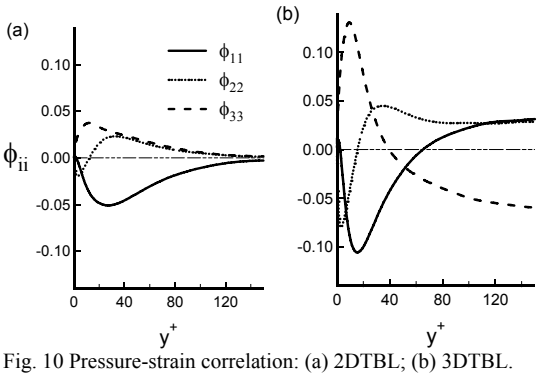

Fig. 10 Pressure-strain correlation: (a) 2DTBL; (b) 3DTBL.

3.5 Practical Implementation

One of the practical applications of the present study is the drag reduction of turbulent flow. It was shown by Yoon et al. [24] that setting periodically arrayed heating and cooling strips in a vertical wall can lead to 11% drag reduction at the present studied Grashof number and 35% at Grashof number of 10^7. Such arrangements lead to reversing the directional effect of the buoyancy forces affecting the flow particles moving beside heated then cooled strips. Continuous reverse of the buoyancy forces leads to faster decay of both kinds of vortices and eventually to substantial drag reduction.

4. Conclusion

The present study demonstrates some of the 3DTBL features induced by buoyancy forces. The resulting 3DTBL flow is simpler than the previously investigated flows either experimentally or numerically since the relevant turbulent quantities are function only on the wall-normal direction. Moreover, the flow is three-dimensional from inception and therefore the transient and non-equilibrium effects are absent. The present configuration can be used repeatedly in testing and improving turbulence models. The significance of the present study lies in the predominance of the buoyancy forces in various thermal equipment and the necessity to provide deep understanding for the underlying physics in 3DTBL induced by buoyancy.

Comparisons with the previous experimental and numerical studies show that the present flow has similar characteristics with 3DTBL flows such as the reduction of the structural parameter A_1. However, the anisotropy of the flow necessitates more concern about turbulence modeling dealing with flow three-dimensionality in addition to mixed convection. Intensive investigations on eddy viscosity models and full Reynolds stresses models are needed to test their closures. Difficulties of modeling the triple correlations and pressure-strain terms are presented.

Near-wall structures are proven to be asymmetry in accordance with various 3DTBLs flows. The ability of positive rotating vortices to produce ejection events is weakened; meanwhile, the ability of negative vortices to produce sweep motion is reduced. The resultant effect of both reductions is to reduce the total Reynolds shear stress in accordance with most of the previously studied 3DTBLs. The total contribution from events (ejections and sweeps) associated with the positively rotating vortices is larger than that of negatively rotating vortices.

Acknowledgments

The author thanks Prof. H. H. Chun and Dr. H. S. Yoon for their helpful discussions during the course of this study. This work was supported by Advanced Ship Engineering Research Center (ASERC), Pusan National University, through the Korean Science and Engineering Foundation.

References

[1] Schwarz, WR, Bradshaw, P., "Measurements in a pressure driven three-dimensional turbulent boundary layer during development and decay" AIAA J. Vol. 31, 1993, 1207-1214.

[2] Schwarz, WR, Bradshaw, P., "Turbulence structural changes for a three-dimensional turbulent boundary layer in a 30 degree bend". Journal of Fluid Mech. Vol. 272, 1994, 183-209.

[3] Schwarz, WR, Bradshaw, P., "Term-by-term tests of stress-transport turbulence models in a three-dimensional boundary layer" Phys. Fluids, Vol. 6, 1994, 986-998.

[4] Flack, KA. "Near-wall structure of three-dimensional turbulent boundary layers". Experiments in Fluids, Vol 3, 1997, 335-340.

[5] Bradshaw, P., Pontikos, NS, "Measurements in the turbulent boundary layer on an infinite swept wing" Journal Fluid Mech., Vol. 159, 1985, 105-130.

[6] Ölçmen, MS, Simpson, RL, "An experimental study of a three-dimensional pressure-driven turbulent boundary layer"J. Fluid Mech., Vol. 290, 1995, 225-262.

[7] Compton, DA, Eaton, JK, "Near-wall measurements in a three-dimensional turbulent boundary layer" Journal Fluid Mech., Vol. 350, 1997, 189-208.

[8] Anderson, SD, Eaton, JK," Reynolds stress development in pressure-driven three-dimensional turbulent boundary layers". J. Fluid Mech., Vol. 202, 1989, 263-294.

[9] Eaton, JK. "Effects of mean flow three-dimensionality on turbulent boundary layer structure". AIAA J., Vol. 33, 1995, 2020-2025.

[10] Littell, HS, Eaton, JK. "Turbulence characteristics of the boundary layer on a rotating disk.", J. Fluid Mech., Vol. 266, 1994, 175-207.

[11] Chiang, C., Eaton, JK. "An experimental study of the effects of three-dimensionality on the near wall turbulence structures using flow visualization" Experiments in Fluids, Vol. 20, 1996, 266-272.

[12] Kang, HS, Choi, H., Yoo, JY. "On the modification of the near-wall coherent structure in a three-dimensional turbulent boundary layer on a free rotating disk", Phys. Fluids, Vol. 10, 1998, 2315-2322.

[13] Spalart, PR. "Theoretical and numerical study of a three-dimensional turbulent boundary layer". J. Fluid Mech. Vol. 205, 1989, 319-340.

[14] Spalart, PR. "Direct simulation of a turbulent boundary layer up to Re_q=1410", J. Fluid Mech., Vol. 187, 1988, 61-98.

[15] Coleman, GN, Ferziger, JH, Spalart, PR. A numerical study of the turbulent Ekman layer. J. Fluid Mech., Vol. 213, 1990, 313-348.

[16] Moin, P., Shih, T.–H, Driver, D., Mansour, NN. "Direct numerical simulation of a three-dimensional boundary layer." Phys. Fluids , Vol. 2, 1990, 1846-1853.

[17] Coleman, GN, Kim, J., Spalart, PR." Direct numerical simulation of strained three-dimensional wall-bounded flows". Experimental Thermal Fluid Science , Vol. 13, 1996, 239-251.

[18] Coleman, GN, Kim, J., Le, A.-T. "A Numerical study of three-dimensional wall-bounded flows". Int. J. Heat Fluid Flow Vol. 17, 1996, 333-342.

[19] Le, A.-T., Coleman, GN, Kim, J. "Near-wall turbulence structures in three-dimensional boundary layer". International Journal Heat Fluid Flow, Vol. 21, 2000, 480-488.

[20] Wu, X., Squares, KD. "Large eddy simulation of an equilibrium three-dimensional turbulent boundary layer." AIAA J. Vol. 35, 1997, 67-74.

[21] El-Samni, OA, Yoon, HS, Chun, HH. "Direct numerical simulation of turbulent flow in a vertical channel with buoyancy orthogonal to the mean flow". Int. J. Heat Mass Transfer Vol. 48, 2005, 1267-1282.

[22] Iwamoto, K., Suzuki, Y., Kasagi, N. "Reynolds number effect on wall turbulence. toward effective feedback control". Int. J. Heat Fluid Flow, Vol. 23, 2002, 678-689.

[23] Kim, J., Moin, P., Moser, R. "Turbulence statistics in fully developed channel flow at low Reynolds number." J. Fluid Mech., Vol. 177, 1978, 133-166.

[24] Yoon, HS, El-Samni, OA, Chun, HH." Drag reduction in turbulent channel flow with periodically arrayed heating and cooling strips". Physics of Fluids Vol. 18, 2006, 025104.

JJMIE

Volume 1, Number 2, Dec. 2007
ISSN 1995-6665
Pages 105 - 111

Jordan Journal of Mechanical and Industrial Engineering

Strain-Concentration Factor of Notched Cylindrical Austenitic Stainless Steel Bar with Double Slant Circumferential U-Notches Under Static Tension

Hitham M. Tlilan [a,*], Ahmad S. Al-Shyyab [a], Tariq Darabseh [b], Majima Tamotsu [c]

[a] Department of Mechanical Engg., Faculty of Engg., The Hashemite University, P.O. Box 330127, Zarqa 13133, Jordan
[b] Department of Mechanical Engg., Faculty of Engg., J.U.S.T, Irbid, 22110, Jordan
[c] Graduate School of Science and Technology, Chiba University, Chiba, 263-8522, Japan

Abstract

The interference effect on the new strain-concentration factor (SNCF), defined under the triaxial stress state, is studied for circumferentially notched cylindrical bars with double-slant notches under static tension. The material employed is Austenitic stainless steel. The results indicate that the new SNCF (K_ε^{new}) for a certain l_o is constant during elastic deformation and increases with decreasing pitch l_o. It also increases with increasing notch radius. The elastic K_ε^{new} for l_o = 0.5 mm is the minimum. This becomes prominent with decreasing notch radius. The new SNCF increases from its elastic value to a peak value as the plastic deformation develops from notch root. On further plastic deformation, the new SNCF increases to the maximum value for l_o = 0.0 and $l_o \geq 2.5$ and then decreases with plastic deformation. This peak value is the maximum K_ε^{new} for $0.0 < l_o \leq 2.0$.

Keywords: Austenitic stainless steel; interference; slanted notch; strain-concentration factor; tension;

Nomenclature

Alphabetic symbols

A	: net-section area
d_o	: initial net-section diameter
D_o	: initial gross diameter
E	: Young's modulus
K_ε^{con}	: conventional strain-concentration factor
K_ε^{new}	: new strain-concentration factor
P	: tensile load
P_Y	: tensile load at yielding at the notch root
r	: instantaneous distance from the center of the net-section ($0 \leq r \leq r_n$)
r_n	: instantaneous net-section radius = $d/2$
s	: $= r/r_n$ ($0 \leq s \leq 1.0$)

Greek Symbols

ε_z	: axial strain
$(\varepsilon_z)_{av}^{con}$	: conventional average axial strain
$(\varepsilon_z)_{av}^{new}$	: new average axial strain
$(\varepsilon_z)_{max}$	: maximum axial strain
ν	: Poisson's ratio
ρ_o	: initial notch radius
σ_{eq}	: equivalent stress $= \left\{(\sigma_z-\sigma_\theta)^2+(\sigma_\theta-\sigma_r)^2+(\sigma_r-\sigma_z)^2\right\}^{1/2}/\sqrt{2}$
$(\sigma_{eq})_{max}$	: equivalent stress at the notch root
σ_r , σ_z , σ_θ	: radial , axial and tangential stresses
σ_Y	: yield stress
$(\sigma_z)_{av}$	: average axial stress at the net section = P/A
$(\sigma_z)_{max}$	: axial stress at the notch root in elastic deformation
$(\sigma_\theta)_{max}$	: tangential stress at the notch root in elastic deformation

1. Introduction

Geometrical irregularities, in the following referred to as notches, are of prime importance in the life assessment of machine elements, since they act as local stress and strain raisers. The presence of notches in machine element forms an interruption of the load path; it will, therefore, bring about stress and strain concentrations at the notch root. The knowledge of stress and strain distributions on the net section is valuable for practical design and application of various engineering elements. In addition to

* Corresponding author. e-mail: hitham@hu.edu.jo

the stress and strain concentrations introduced by the notch, there is also a change in the stress state even if the stress state is uniaxial throughout the remainder of the gage length. That is, the stress state becomes triaxial stress state in the immediate vicinity of the notch root.

Attempts have been made to predict the axial strain at the notch root under static and cyclic tensile loading. This prediction was made using the SNCF, referred to as the conventional SNCF here, through Neuber's rule [1-7], Glinka's method [3, 5, 7, 8] or linear rule [2, 4, 5, 9]. Comparison of the predicted values with finite element and experimental ones indicates that no rule can accurately predict the magnitude of the axial strain at the notch root. In particular, in notched rectangular bars the accuracy of the prediction decreases with increasing the thickness. The reason for this is that the conventional SNCF is defined under the uniaxial stress state [10], while the axial strain at the notch root occurs under the triaxial stress state. Strain-concentration factor should thus be defined under the triaxial stress state at the net section.

A new SNCF has been proposed by Majima under axial tension [10]. This new SNCF has been defined under the triaxial stress state at the net section. This has enabled the new SNCF to provide the reasonable values consistent with concave distributions of the axial strain on the net section [10, 11]. Moreover, this new SNCF has removed the contradiction that the conventional SNCF has the values less than unity for the concave distributions of the axial strain under elastic-plastic deformation. As mentioned earlier, the average axial strain or the nominal strain of the conventional SNCF has been defined under the uniaxial stress state; completely unrelated to the stress state at the net section [10, 11]. This causes the above contradiction of the conventional SNCF. This result indicates that the SNCF for any type of loading should be defined under the triaxial stress state at the net section.

Some studies have been made on the interference effect on the elastic stress-concentration factor (SSCF) of the flat bars with double U- or semicircular notches under tension. The obtained relations between the elastic SSCF and the notch pitch have been published for engineering design [12]. The important thing deduced from these studies is that the SSCF subjected to the interference effect is less than the SSCF of a single notch. Few studies have been carried out on the interference effect on the elastic SSCF of cylindrical bars with double U- or semicircular notches under tension [12]. Moreover, only two studies have been performed on the interference effect on strength such as yield point load and ultimate tensile strength and deformation properties of notched bars under tension [13, 14]. In these studies the interference effect has also been discussed on the elastic SSCF of cylindrical bars with double U-notches under tension.

In this paper the slant notch is employed to study the interference effect on the elastic-plastic SNCF accordingly. This is because the slant notch is closely related to the cracks growing in the slant direction.

2. Strain-Concentration Factor under Static Tension

The new strain-concentration factor (SNCF) proposed for tensile loading is given by [10]

$$K_{\varepsilon}^{\text{new}} = \frac{(\varepsilon_z)_{max}}{(\varepsilon_z)_{\text{av}}^{\text{new}}} \tag{2-1}$$

where $(\varepsilon_z)_{\max}$ and $(\varepsilon_z)_{\text{av}}^{\text{new}}$ are the maximum axial strain at the notch root and the new average axial or new nominal strain, respectively. The maximum axial strain at the notch root is independent of definition, and hence the new SNCF depends on a new definition of the average axial strain. For circumferentially notched cylindrical bars $(\varepsilon_z)_{\text{av}}^{\text{new}}$ is defined as follows [10]:

$$\begin{aligned}(\varepsilon_z)_{\text{av}}^{\text{new}} &= \frac{1}{\pi r_{\text{n}}^2}\int_0^{r_{\text{n}}} \varepsilon_z(r)\, 2\pi r\, dr \\ &= 2\int_0^1 \varepsilon_z(s)\, s\, ds\end{aligned} \tag{2-2}$$

where $s = r/r_{\text{n}}$. In the elastic level of deformation, $(\varepsilon_z)_{\text{av}}^{\text{new}}$ can be transformed into the following equation:

$$\begin{aligned}(\varepsilon_z)_{\text{av}}^{\text{new}} &= \frac{1}{\pi r_{\text{n}}^2}\int_0^{r_{\text{n}}} [\frac{\sigma_z}{E} - \frac{\nu}{E}(\sigma_\theta + \sigma_r)]\, 2\pi r\, dr \\ &= \frac{1}{E}\cdot\frac{1}{\pi r_{\text{n}}^2}\int_0^{r_{\text{n}}} \sigma_z\, 2\pi r\, dr - \frac{\nu}{E}\cdot\frac{1}{\pi r_{\text{n}}^2}\int_0^{r_{\text{n}}} (\sigma_\theta + \sigma_r)\, 2\pi r\, dr \\ &= \frac{1}{E}\cdot\frac{P}{\pi r_{\text{n}}^2} - \frac{\nu}{E}\cdot\frac{1}{\pi r_{\text{n}}^2}\int_0^{r_{\text{n}}} (\sigma_\theta + \sigma_r)\, 2\pi r\, dr \\ &= \frac{(\sigma_z)_{\text{av}}}{E} - \frac{\nu}{E}\cdot\frac{1}{\pi r_{\text{n}}^2}\int_0^{r_{\text{n}}} (\sigma_\theta + \sigma_r)\, 2\pi r\, dr\end{aligned} \tag{2-3}$$

where E and ν are the Young's modulus and Poisson's ratio, respectively. Equation (2-3) can be rewritten as follows:

$$(\varepsilon_z)_{\text{av}}^{\text{new}} = \frac{(\sigma_z)_{\text{av}}}{E} - \frac{2\nu}{E}\int_0^1 \{\sigma_\theta(s) + \sigma_r(s)\}\, s\, ds \tag{2-4}$$

This equation indicates that $(\varepsilon_z)_{\text{av}}^{\text{new}}$ is defined under the triaxial stress state at the net section. It should be noted that $(\varepsilon_z)_{\text{av}}^{\text{new}}$, given by Eq. (2-2), is defined under the triaxial stress state also in plastically deformed area at the net section. This is due to the following reason: the plastic component of the axial strain is directly related to the triaxial stress state, as indicated by the theory of plasticity. The definition under the triaxial stress state gives reasonable results consistent with the concave distribution of the axial strain at any deformation level [10, 11].

The conventional SNCF under static tension has been defined as the ratio of the maximum axial strain $(\varepsilon_z)_{\max}$ at the notch root to the conventional average axial strain $(\varepsilon_z)_{\text{av}}^{\text{con}}$, i.e.

$$K_{\varepsilon}^{\text{con}} = \frac{(\varepsilon_z)_{\max}}{(\varepsilon_z)_{\text{av}}^{\text{con}}} \tag{2-5}$$

This conventional SNCF has been defined under uniaxial stress state at the net section. This is because the conventional average axial strain $(\varepsilon_z)_{\text{av}}^{\text{con}}$ has been defined under uniaxial stress state [10]. In elastic deformation, the axial stress σ_z at the notch root $(\sigma_z)_{\max}$ is much greater than $(\sigma_z)_{\text{av}}$, and the equivalent stress at the notch root $(\sigma_{\text{eq}})_{\max}$ is

a little lower than $(\sigma_z)_{max}$ under the biaxial tensile stress state. This indicates that the small plastic deformation occurs around the notch root even in the range $(\sigma_z)_{av} \leq \sigma_Y$, when $(\sigma_z)_{av}$ approaches σ_Y. Even in this range $(\varepsilon_z)_{av}^{con}$ is given by

$$(\varepsilon_z)_{av}^{con} = \frac{(\sigma_z)_{av}}{E} \qquad (2\text{-}6)$$

This equation indicates that the conventional definition has neglected the effect of tangential and radial stresses σ_θ and σ_r, respectively. On further development of plastic deformation, i.e. in the range $(\sigma_z)_{av} > \sigma_Y$, $(\varepsilon_z)_{av}^{con}$ is determined using the uniaxial true stress–total strain curve $\sigma = f(\varepsilon)$. The reason for using this curve is that $(\varepsilon_z)_{av}^{con}$ is defined under the uniaxial stress state and $(\sigma_z)_{av}$ is based on the instantaneous area of the net section. The conventional average axial strain is therefore given by

$$(\varepsilon_z)_{av}^{con} = f^{-1}\{(\sigma_z)_{av}\} \qquad (2\text{-}7)$$

As the plastic deformation develops from the notch root; i.e. $\sigma_{eq} > \sigma_Y$, the newly defined average axial strain has been calculated using the incremental or flow theory, which relates the stresses to the plastic strain increments. In the plastic deformation the strains in general are not uniquely determined by the stresses but depend on the entire history of loading.

3. Geometries and Materials

3.1. Geometries

The employed cylindrical bar with double-slant circumferential U-notches is shown in Fig. 1. The net-section diameter d_o of 10.0 mm and the gross diameter D_o of 16.7 mm were selected to give the net-to-gross diameter ratio d_o/D_o of 0.6. The specimen length is expressed as $(2L_o+2lo)$, where $2L_o$ and $2l_o$ are the unnotched length from the notch to the loaded end and the notch pitch, as shown in Fig. 1. The unnotched length L_o is 25 mm, held constant, while the half notch pitch l_o is varied from 0.0 to 12.5 mm to examine the interference effect of the double-slant circumferential U-notches. The notch pitch $2l_o$= 0.0 mm means a cylindrical bar with a circumferential V-notch, perpendicular to the axial direction. Two notch radii ρ_o of 0.5 and 1.0 mm are employed to vary the notch sharpness $d_o/2\rho_o$. The calculations were made on the double-slant circumferential U-notches of the slant angle of $\gamma = 45^o$.

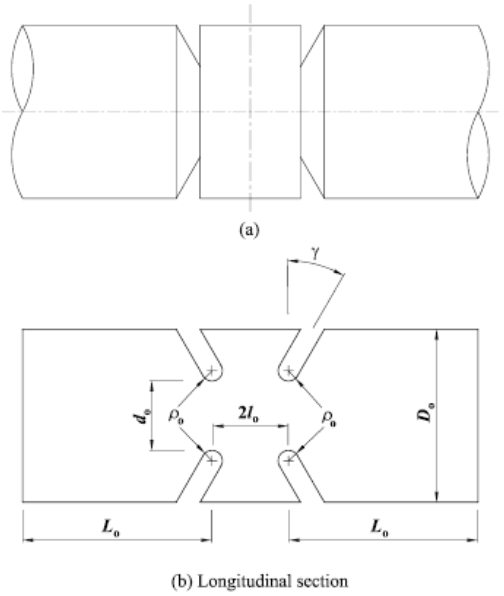

Figure 1: Cylindrical bar with double-slant circumferential U-notches.

3.2. Materials

The material employed is an Austenitic stainless steel. Young's modulus E, Poisson's ratio ν and the tensile yield stress σ_Y are listed in Table 1. The true stress-plastic strain curves were obtained from tension tests. In order to express the stress-strain curve accurately the obtained relation was divided into a few ranges of plastic strain and in each range the following fifth-degree polynomial was fitted:

$$\sigma = C_o + C_1\varepsilon_p + C_2\varepsilon_p^2 + C_3\varepsilon_p^3 + C_4\varepsilon_p^4 + C_5\varepsilon_p^5$$

The values of these coefficients in the plastic strain ranges used are also listed in Table 1. Figure 2 shows the true stress-plastic strain curve given by this polynomial.

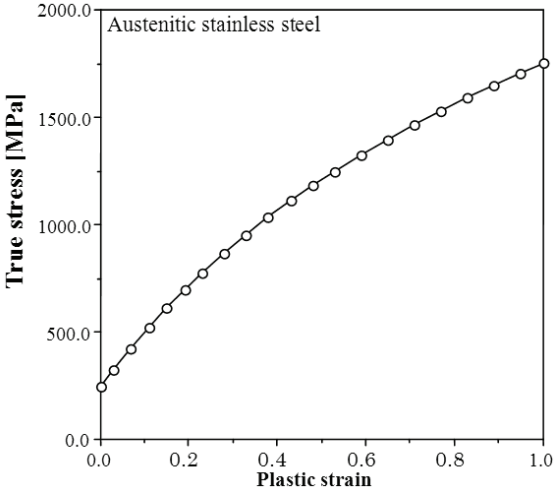

Figure 2: True Stress-strain curve for the plastic range of the material used.

Table 1: Mechanical properties and polynomial coefficients

Material ν, E [GPa], σ_Y [MPa]	Plastic strain range	C_o	C_1	C_2	C_3	C_4	C_5
Austenitic stainless steel	$\varepsilon_p \le 0.2$	2.459×10^2	4.389×10^3	-3.265×10^4	2.402×10^5	-8.899×10^5	1.258×10^6
0.30, 206, 245.9	$0.2< \varepsilon_p \le 0.5$	3.789×10^2	1.535×10^3	1.173×10^3	-1.874×10^3	0.0	0.0

4. Finite Element Mesh For Double-Slant Circumferential U-Notches

Figure 3 shows a finite element mesh of one quarter of a notched specimen with the double-slant circumferential U-notches. An eight-node axisymmetric ring element was chosen to model the notched specimens. The number of elements and nodes are given in Table 2 for ρ_o = 0.5 mm and in Table 3 for ρ_o =1.0 mm.

Table 2: Finite element mesh parameters for the double-slant circumferential U-notches of γ = 45° and ρ_o = 0.5 mm

l_o [mm]	L_o+l_o [mm]	No. of elements r × z	No. of elements Total	No. of nodes
0	25.0	18 × 28	504	1605
0.5	25.5	18 × 33	594	1885
1.5	26.5	18 × 39	702	2221
2.0	27.0	18 × 39	720	2277
2.5	27.5	18 × 41	738	2333
3.0	28.0	18 × 41	738	2333
3.5	28.5	18 × 41	738	2333
4.0	29.0	18 × 42	756	2389
5.0	30.0	18 × 42	756	2389
7.5	32.5	18 × 42	756	2389
10.0	35.0	18 × 44	792	2501
12.5	37.5	18 × 45	810	2551

Table 3: Finite element mesh parameters for the double-slant circumferential U-notches of γ = 45° and ρ_o =1.0 mm

l_o [mm]	L_o+l_o [mm]	No. of elements r × z	No. of elements Total	No. of nodes
0.0	25.0	18 × 28	504	1605
0.5	25.5	18 × 28	504	1605
1.0	26.0	18 × 35	630	1997
2.0	27.0	18 × 39	702	2221
2.5	27.5	18 × 41	738	2333
3.0	28.0	18 × 41	738	2333
4.0	29.0	18 × 43	774	2450
5.0	30.0	18 × 43	774	2450
7.5	32.5	18 × 43	774	2450
10.0	35.0	18 × 45	810	2557
12.5	37.5	18 × 47	846	2669

The FEM calculations were performed under the axisymmetric deformation; this deformation was given under the condition that the axial displacement at the gross section in the center of the notch pitch and the radial displacement at the central axis are zero. The increments of the axial displacement were applied at the right end of the unnotched part of $2L_o$. The magnitude of the increment was small enough to provide an elastic solution for the first few increments in each notched specimen. All of the calculations were performed using MARC K6.2 on an APOLLO workstation.

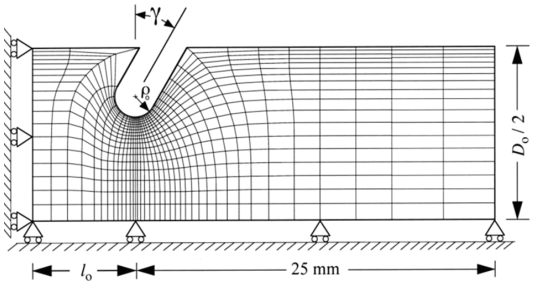

Figure 3: Finite element mesh of cylindrical bar with double-slant circumferential U- notches

5. Results and Discussion

5.1. Interference effect on the elastic new SNCF K_ε^{new}

Figure 4 shows the relation between the elastic new SNCF K_ε^{new} and half notch pitch l_o. The half notch pitch l_o = 0.0 mm means the single circumferential V-notch with the notch angle of 2γ. The elastic K_ε^{new} decreases very rapidly from the value at the half notch pitch l_o = 0.0 mm and reaches its minimum at $l_o \approx$ 0.5 mm. On further increase in l_o the elastic K_ε^{new} gradually increases and finally reaches the value of the single circumferential V-notch (l_o = 0.0 mm) at $l_o \approx$ 7.5 mm. Beyond this value of l_o the elastic K_ε^{new} is nearly constant up to l_o = 12.5 mm, the maximum half notch pitch in the FEM calculations. The elastic K_ε^{new} in the range 7.5 mm ≤ l_o ≤ 12.5 mm are nearly equal to the elastic K_ε^{new} of the circumferential V-notch (l_o = 0.0 mm). This indicates that the interference effect on the elastic K_ε^{new} is extremely strong in a small range of l_o and nearly vanishes beyond $l_o \approx$ 7.5 mm.

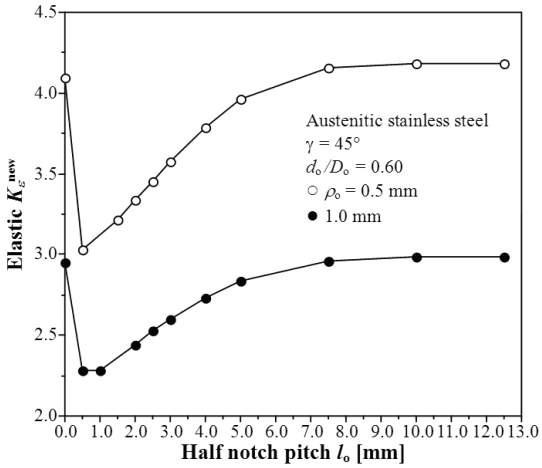

Figure 4: Effect of the half notch pitch l_o on the elastic K_ε^{new}

The variations in the maximum axial strain $(\varepsilon_z)_{max}$ and the new average axial strain $(\varepsilon_z)_{av}^{new}$ with tensile load P are shown in Fig. 5. It should be noted that plastic deformation already started at the notch root in the range $P \geq 7.5$ kN, Fig. 5. The maximum axial strain shows a strong dependence on the half notch pitch l_o in the elastic deformation, while the new average axial strain is nearly independent of l_o. The maximum axial strain at $l_o = 0.5$ mm is less than that for any other notch pitch, and hence the minimum elastic K_ε^{new} occurs at $l_o = 0.5$ mm. On the other hand, the maximum axial strain at $l_o = 12.5$ mm is greater than that at any other notch pitch and nearly equal to that at $l_o = 0.0$ mm. The maximum elastic K_ε^{new} thus occurs at $l_o = 0.0$ and 12.5 mm.

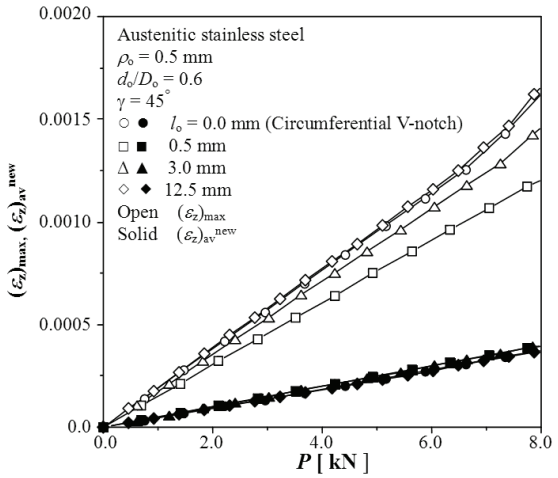

Figure 5: Effect of half notch pitch l_o on the variations in $(\varepsilon_z)_{max}$ and $(\varepsilon_z)_{av}^{new}$ with P at elastic deformation

5.2. Interference effect on the variations in K_ε^{new} with P

The variations in the new SNCF K_ε^{new} with tensile load P for $\rho_o = 0.5$ and 1.0 mm are given in Figs. 6 and 7, respectively. The results are shown for the double-slant circumferential U-notches of the slant angle $\gamma = 45°$ and of the notch radii $\rho_o = 0.5$ and 1.0 mm. The new SNCF increases from its elastic value. There is a load range where the rate of increase in the new SNCF decreases for the notch radius of 0.5 mm; this load range is independent of notch pitch. On further increase in tensile load the new SNCF rapidly increases again up to the maximum value and decreases. Approximately the same results were obtained for $l_o = 7.5$ and 10 mm.

For the notch radius of 1.0 mm the new SNCF increases from its elastic value to the peak value except for $l_o = 0.5$ to 2.5 mm. In these half notch pitches the gradual increase in the new SNCF is maintained in the load range where the peak value occurs for $l_o = 0.0$ and 3.0 to 12.5 mm. On further increase in tensile load the new SNCF rapidly increases again up to the maximum value, much greater than the peak value, and decreases after that. Approximately the same results were obtained for $l_o = 7.5$ and 10 mm.

The value of the tensile load P producing the maximum K_ε^{new} tends to increase with increasing l_o in the half notch pitch range from 0.5 to 12.5 mm. Furthermore, the value of P at the maximum K_ε^{new} of l_o=12.5 mm is approximately the same as that of l_o= 0 mm, the single circumferential V-notch.

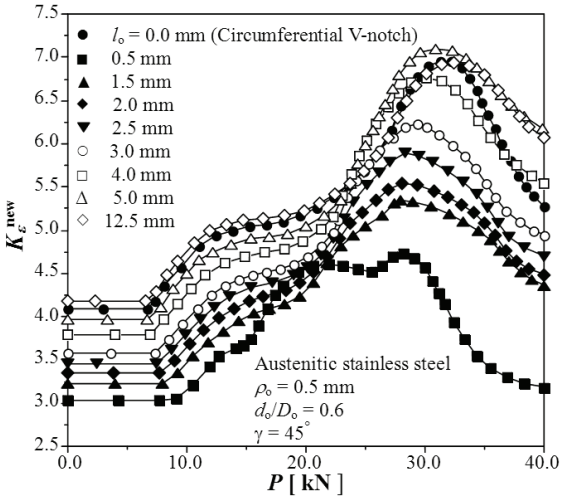

Figure 6: Effect of the half notch pitch l_o on the variations in K_ε^{new} with P for ρ_o=0.5 mm

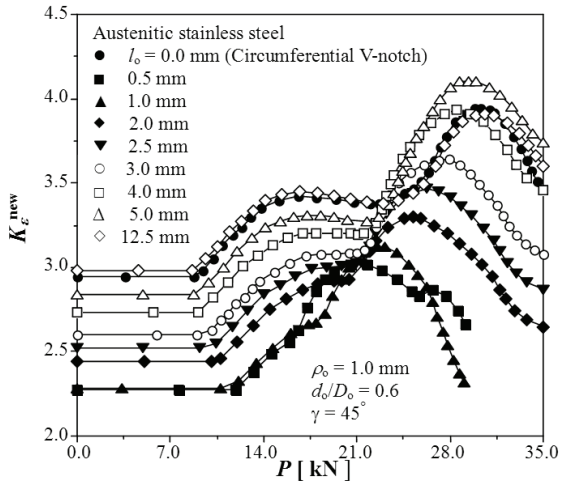

Figure 7: Effect of the half notch pitch l_o on the variations in K_ε^{new} with P for ρ_o=1.0 mm

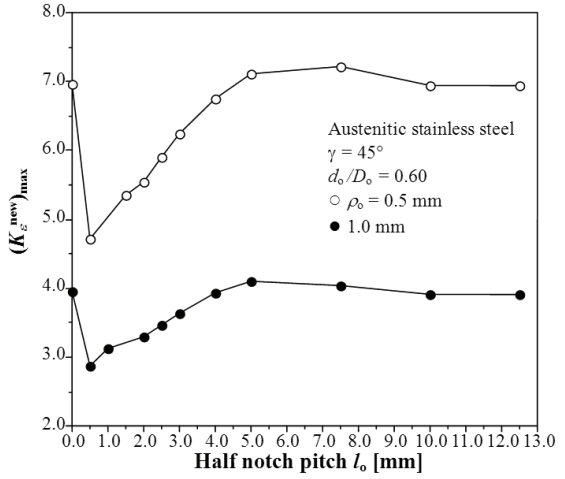

Figure 8 Effect of the half notch pitch l_o on $(K_\varepsilon^{new})_{max}$

This means that the maximum half notch pitch where the interference effect occurs on the maximum new K_ε^{new} is l_o= 12.5 mm. Figure 8 however shows that the half notch pitch where the interference effect occurs on the maximum new K_ε^{new} is much less than the half notch pitch of 12.5 mm; Fig. 8 shows the maximum new SNCF $(K_\varepsilon^{new})_{max}$ versus l_o relation for ρ_o = 0.5 and 1 mm. The relation between $(K_\varepsilon^{new})_{max}$ and l_o is remarkably similar in shape to that between the elastic K_ε^{new} and l_o. The maximum K_ε^{new} decreases very rapidly from its value at l_o= 0 mm to the minimum value at l_o= 0.5 mm. On further increase in l_o the maximum new SNCF increases and reaches the maximum value at l_o= 7.5 mm for ρ_o = 0.5 mm and at l_o = 5.0 mm for ρ_o = 1 mm. The values of the maximum K_ε^{new} of l_o = 10.0 and 12.5 mm are nearly equal to (ρ_o = 0.5 mm) or slightly less (ρ_o = 1.0 mm) than that of l_o = 0 mm, the single circumferential V-notch.

The new SNCF at l_o= 0.5 mm is the minimum value at any deformation level because the maximum axial strain of l_o = 0.5 mm is the smallest of all the notch pitches, as shown in Fig. 9. This is independent of notch radius. It should be noted that the maximum axial strain depends on l_o, while the new average axial strain is independent of l_o up to P = 25.0 kN, beyond which $(K_\varepsilon^{new})_{max}$ occurs. In the notched tension specimens, the plastic deformation is localized in a very narrow zone and spreads from notch root to the net section center. As a result, the maximum axial strain lies at the notch root [10, 13, and 14]. However, the current results indicate that this localization is prominent when the notch pitch becomes greater than 7.5 mm.

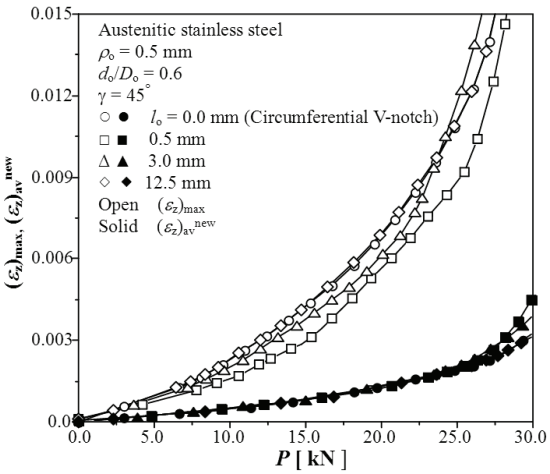

Figure 9: Effect of the half notch pitch l_o on the variation in $(\varepsilon_z)_{max}$ and $(\varepsilon_z)_{av}^{new}$ with P

This occurs because the notches with minimum pitches, i.e. $l_o \leq$ 7.5mm, produce the smaller percentage of the deformed region with large plastic strain than the notches with $l_o >$ 7.5mm do. Moreover, the plastic deformation spreads in inclined direction from the notch root to the pitch center line, as shown in Fig. 10. Therefore, the maximum axial strain for l_o= 0.5mm is the minimum and the K_ε^{new} for the minimum pitch is the smallest at any level of deformation.

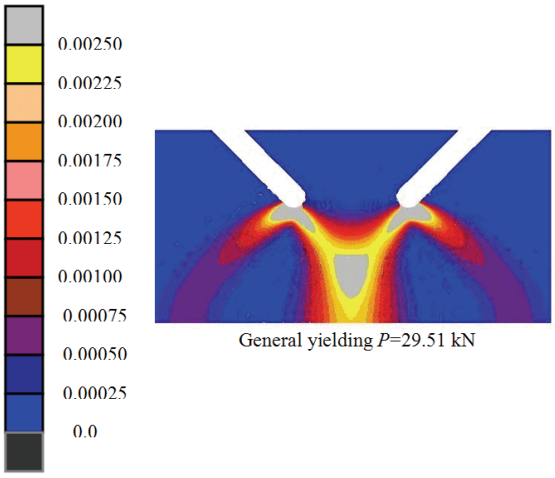

Figure 10: Distributions of the total equivalent plastic strain on the net section of double-slant circumferential U-notches with l_o=2.5 mm, ρ_o = 0.5 mm and γ =45°

6. Conclusions

The results given in Figs. 4 through 9 are of the double-slant circumferential U-notches of the slant angle γ = 45 and of two notch radii of 0.5 and 1.0 mm. The following conclusions can be drawn from the results:

1. The relation between the elastic new SNCF and half notch pitch l_o shows very rapid decrease from the value at l_o= 0 mm with increasing l_o. The elastic new SNCF becomes minimum at $l_o \approx$ 0.5 mm. On further increase in l_o the elastic new SNCF gradually increases and reaches the maximum value at $l_o \approx$ 7.5 mm. This maximum value is nearly equal to the elastic new SNCF at l_o = 0 mm. The elastic new SNCF is almost constant up to l_o = 12.5 mm for further notch pitch.
2. The relation between the maximum new SNCF in plastic deformation and l_o is remarkably similar in shape to that between the elastic new SNCF and l_o. The maximum notch pitch where the interference effect occurs on this maximum new SNCF tends to be less than the notch pitch where the interference effect occurs in the relation between the elastic new SNCF and l_o.
3. The new SNCF rapidly increases from its elastic value with increasing tensile load. It shows the peak value or the gradual increase after this rapid increase. On further increase in tensile load the new SNCF rapidly increases again to the maximum value and finally decreases. The maximum value is much greater than the peak value. Particularly, the ratio between the maximum value and the peak value of the new SNCF is varying form 1.1 to 1.75, i.e. nearly 1.1 for l_o=0.5 mm and 1.75 for l_o=12.5mm.

References

[1] W.N.Jr. Sharp, M. Ward, "Benchmark cyclic plastic notch strain measurements". Trans. ASME, J. Engng Mater. Technol. Vol. 105, 1983, 235-241.

[2] A.R. Gowhari-anaraki, S.J. Hardy, "Low cycle fatigue life predictions for hollow tubes with axially loaded axisymmetric internal projections". J. Strain Analysis, Vol. 26, 1991, 133-146.

[3] W.N.Jr. Sharp, "ASME 1993 Nadai Lecture-Elastoplastic stress and strain concentrations". Trans. ASME, J. Engng Mater. Technol., Vol. 117, 1995, 1-7.

[4] S.J. Hardy, M.K. Pipelzadeh, "An assessment of the notch stress-strain conversion rules for short flat bars with projections subjected to axial and shear loading." Journal . Strain Analysis. Vol. 31, No. 2, 1996, 91-110.

[5] Z. Zeng, A. Fatemi, "Elasto-plastic stress and strain behaviour at notch roots under monotonic and cyclic loadings". Journal Strain Analysis, Vol. 36, 2001, 287-288.

[6] G. Harkegard, T. Mann, "Neuber prediction of elastic-plastic strain concentration in notched tensile specimens under large-scale yielding". J. Strain Analysis, Vol. 38, 2003, 79-94.

[7] P. Livieri, G.. Nicoletto, "Elastoplastic strain concentration factors in finite thickness plates". J. Strain Analysis, Vol. 38, 2003, 31-36.

[8] G. Glinka, "Energy density approach to calculation of inelastic strain-stress near notches and cracks". Engng Fracture Mechanics, Vol. 22, 1985, 485-508.

[9] H.O Fuchs, R.L.Stephens, ,. Metal fatigue in engineering. New York: John Wiley and Sons; 1980.

[10] T. Majima, "Strain-concentration factor of circumferentially notched cylindrical bars under static tension". Journal Strain Analysis, Vol. 34, No. 5, 1999, 347-360.

[11] H. M. Tlilan, S. Yousuke, T. Majima, "Effect of notch depth on strain-concentration factor of notched cylindrical bars under static tension", European Journal of Mechanics A/Solids. Vol. 24 , 2005, 406-416.

[12] W.D. Pilkey. Peterson's stress concentration factors. New York: Wiley; 1997.

[13] T. Majima, "Interference effect of notches (1st report, evaluation of interference effect of notches on yield point load of double U-shaped notches by upper and lower bound theorems)". *Trans*. *Japan Soc*. *Mech*. *Engrs*., Vol. 48, No. 430, 1982, 719-728.

[14] T. Majima, K. Watanabe, "Interference effect of notches (2nd report, an experimental investigation of interference effect on strength and deformation properties of notched bars with double symmetrical u-notches)". *Trans*. *Japan Soc*. *Mech*. *Engrs*. Vol. 48, No. 433, 1982, 1186-1194.

JJMIE

Volume 1, Number 2, Dec. 2007
ISSN 1995-6665
Pages 113 - 118

Jordan Journal of Mechanical and Industrial Engineering

Viscous and Joule Heating Effects over an Isothermal Cone in Saturated Porous Media

H. M. Duwairi [a,*], Osama Abu-Zeid [a], Rebhi A. Damseh [b]

[a] Mechanical Engineering Department, Faculty of Engineering and Technology, The University of Jordan, 11942 Amman- Jordan
[b] Mechanical Engineering Department, Al-Huson University College, Al-Balqa Applied University

Abstract

In this paper, the magnetohydrodynamic mixed convection flow about an isothermal cone embedded in a saturated porous medium is considered. The Darcian model including the viscous dissipation effects in the energy equation is used. The governing equations are transformed by using a set of nonsimilarity variables and solved by using Keller box method. The entire mixed convection regime is covered by nonsimilarity parameter χ, where χ=0 corresponds to pure free convection and χ=1 corresponds to pure forced convection. Numerical results for the dimensionless velocity and temperature profiles and the local Nusselt number for various values of the mixed convection parameter χ, the cone angle parameter m, the magnetic field strength parameter H, and the modify Gebhart number Ge^* are drawn. It is found that increasing the magnetic strength decreased the heat transfer rates, while increasing the cone angle increased the heat transfer rates.

Keywords: viscous heating; Joule heating; mixed convection;

Nomenclature

Alphabetic symbols

B_y	: Magnetic field flux density
Cf_z	: Local skin friction factor
c_p	: Specific heat capacity
f	: Dimensionless stream function
g	: Gravitational acceleration
Ha	: Hartman number, $\sqrt{\sigma B_y^2 K/\rho\upsilon}$
K	: Permeability coefficient of the porous medium
m	: Cone angle parameter
q_w	: Dimensionless local surface heat flux
r	: Local radius of the cone
Ra_x	: Modified local Rayleigh number
Ge^*	: Modified Gebhart number.
k	:Thermal Conductivity
Nu_z	: Local Nusselt number, hx/k
$\overline{Nu}$	: Average Nusselt numbers, $\overline{h}L/k$
p	: Pressure
Pe_z	: Local Peclet number, $U_\infty x/\alpha$
Pr	: Prandtl number, υ/α
T	: Temperature
T_∞	: Free stream temperature
T_w	: Wall temperature
u,V	: Velocity components in x-and y-directions
U_∞	: Free stream velocity

Greek symbols

α	: Thermal diffusivity
β	: Coefficient of thermal expansion
η	: Pseudo-similarity variable
θ	: Dimensionless temperature
μ	: Dynamic viscosity
υ	: Kinematic viscosity
ρ	: Fluid density
σ	: Electrical conductivity
τ_w	: Local wall shear stress
Ψ	: Dimensional stream function
ϕ	: Half angle of the cone
ε	: Porosity
χ	: Mixed convection parameter

1. Introduction

Magnetohydrodynamic mixed convection flow of an electrically conducting fluid about different geometries is of important considerations in the thermal design of a

* Corresponding author. e-mail: duwairi@ju.edu.jo

variety of industrial equipment and also in nuclear reactors, geophysical fluid dynamics. Many articles have been published [1-9] dealing with the problem of MHD-convection heat transfer from different surfaces.

The problem of convection flow along a vertical cone has been investigated by many researchers. Merk and Prins[10] have studied the problem of laminar free convection flow along vertical cone. They found the similarity solutions for the case of an isothermal cone. Hering and Grosh [11] have obtained a number of similarity solutions for cones with prescribed wall temperatures being a power function of the distance from the apex along the generator. Further results were obtained by Hering [12] and by Roy [13], respectively, Pop and Takhar[14] have studied the compressibility effects in laminar free convection from a vertical cone, while Hossain and Paul [15] and Watanabe [16] have considered the effect of suction and injection when the cone surface is permeable. Wang [17] and Wang et al. [18] have presented results for the free convection boundary-layer flow due to a rotating cone with constant or variable surface temperature. Yih [19] studied the radiation effect on mixed convection flow over an isothermal cone embedded in a saturated porous media; the transformed nonlinear system of equations is solved using an implicit finite difference method. Increasing the cone angle increases the heat transfer rates, and the local Nusselt number is significantly increased for the large values of the radiation conduction parameters. Recently, Duwairi and Al-Kablawi [20] have studied the MHD conjugate mixed convection heat transfer from vertical hollow cylinder embedded in a saturated porous media.

In the present work, the effects of magnetic field strength are investigated on mixed convection heat transfer rates over an isothermal cone in a saturated porous medium with viscous dissipation effects included in the energy equation. The governing equations, which describe the problem, wastransformed and solved numerically using the Keller box scheme.

2. Problem Formulation

Consider a vertical isothermal cone with half angle Φ and local radius r, embedded in a saturated porous medium in presence of transverse uniform magnetic field B_y. Figure.1. shows the physical model and the coordinate system. The flow over the cone is assumed to be two-dimensional, laminar, steady and incompressible; the wall temperature of the cone T_w is higher than the ambient temperature T_∞. Assuming low velocity and porosity, the Darcy model is employed in the analysis. The properties of the fluid are assumed to be constant except the density variation in the buoyancy force term. The viscous dissipation effect is included. And the boundary layer approximations is applicable $(v << u, \partial/\partial x << \partial/\partial y)$.

The normal buoyancy force to the surface of the cone is neglected;this approximation is valid for a wide range of cone angle except near Φ=90° and in the region Φ→ 0°. With the above approximations, the governing equations based on Darcy law and the boundary conditions can be written as follows:

$$\frac{\partial(ru)}{\partial x}+\frac{\partial(rv)}{\partial y}=0 \tag{1}$$

$$H\frac{\partial u}{\partial y}=\frac{g\cos\phi\,\beta K}{\upsilon}\frac{\partial T}{\partial y} \tag{2}$$

$$u\frac{\partial T}{\partial x}+v\frac{\partial T}{\partial y}=\alpha\frac{\partial^2 T}{\partial y^2}+\frac{\sigma B_y^2}{\rho c_p}u^2+\frac{\upsilon}{Kc_p}u^2 \tag{3}$$

$$y=0 \;:\; v=0,\; T=T_w \tag{4}$$

$$y\to\infty \;:\; u=U_\infty,\; T=T_\infty \tag{5}$$

Where u, v are the velocity components along the x and y axes, g is the acceleration due to gravity, α is the thermal diffusivity, β, the coefficient of thermal expansion, K, the permeability of the porous medium, ν, the kinematic viscosity, T, the temperature, B_y is the magnetic field density in y direction, H the magnetic field parameter ($H=1+Ha^2/\varepsilon$), Ha, is the Hartman number. Where for the cone problem, $U_\infty=Bx^m$ is the velocity of the potential flow outside the boundary layer. Here , B is prescribed constant and m is the cone angle parameter. The tabulated values: Φ and m are given by Hess and Faulkner [21]. The cone angles of 15, 30, 45, 60 and 75 are discussed in this paper; therefore, m is 0.0316314, 0.1156458, 0.2450773, 0.4241237, and 0.66672777, respectively.

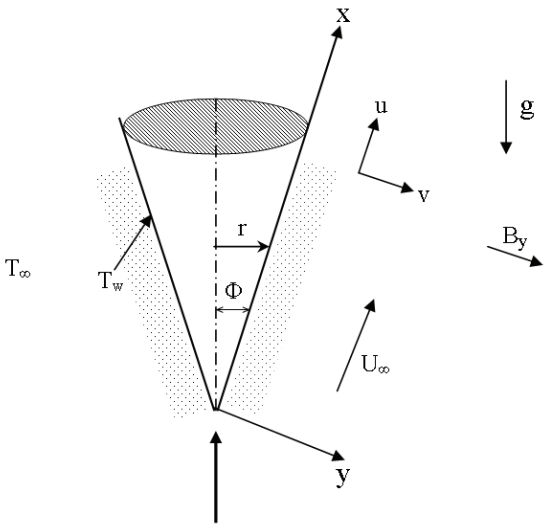

Figure. 1 physical model and coordinate system

3. Nonsimilarity Transformation

In the above system of equations and in order to satisfy the continuity equation defining the stream function as $ru=\partial\psi/\partial y$, and $rv=-\partial\psi/\partial x$ .The following dimensionless variables are introduced in the transformation:

$$\chi=\left[1+\left(\frac{Ra_x}{Pe_x}\right)^{1/2}\right]^{-1} \tag{6}$$

$$\eta = (y/x)Pe_X^{1/2}\ \chi^{-1} \tag{7}$$

$$\psi = \alpha\, r\, Pe_X^{1/2} f(\chi,\eta)\,\chi^{-1}$$
$$\theta(\chi,\eta) = \frac{T-T_\infty}{T_w-T_\infty} \tag{8}$$

And substituting equations (6), (7) and (8) into equations (1)-(5), we obtain the following transformed governing equations:

$$H\ f'' = (1-\chi)^2\,\theta' \tag{9}$$

$$\theta'' + \frac{1}{2}(3+m\chi) f\theta' + \overset{*}{Ge}_x\left[1+\varepsilon(H-1)\right](f')^2 = \frac{m\chi}{2}(1-\chi)\left[f'\frac{\partial\theta}{\partial\chi} - \theta'\frac{\partial f}{\partial\chi}\right] \tag{10}$$

The boundary conditions are:

$$\eta = 0 \ : \ f = 0\,,\ \theta = 1$$
$$\eta \to \infty :\ f' = \chi^2\,,\ \theta = 0 \tag{11}$$

In the above equations, the primes denote the differentiation with respect to η. H is the magnetic field parameter. χ the mixed convection parameter, when χ=0 corresponds to pure free convection and χ =1 corresponds to the other limit of pure forced convection. Between the two limits correspond to the mixed convection regime. Ge^* is the modified Gebhart number defined as:

$$\overset{*}{Ge}_x = g\cos\phi\beta\, x/c_p(1-\chi)^2$$
$$Ra_x = g\cos\phi\,\beta(T_w-T_\infty)K\,x/v\alpha$$
$$Pe_x = U_\infty x/\alpha$$

These are the modified local Rayleigh number and the local Peclet number. The viscous heating effects are excluded from the energy equation by setting $Ge^* = 0$, where the Joule heating effects can be excluded by setting *H=1* which represent the case of absent magnetohydrodynamic forces from the presented cone. Also, it is clear that the Joule heating effects are incorporated in the problem when viscous heating effects are important.

Some of the physical quantities of practical interest include the wall shear stress $\tau_w = \mu(\partial u/\partial y)_{Y=0}$, and the surface heat flux, $h(T_w - T_\infty) = q_w$. They are given by:

$$Nu_x = \frac{hx}{k} = \frac{q_w x}{k(T_w-T_\infty)} \tag{12}$$

$$\frac{Nu_X}{[Pe_x^{1/2} + Ra_x^{1/2}]} = -\theta(\chi,0) \tag{13}$$

$$\frac{Cf_X\,\mathrm{Pr}^{-1}\,Pe_X^2}{[Pe_x^{1/2} + Ra_x^{1/2}]^3} = 2f''(\chi,0) \tag{14}$$

4. Methods of Solution

The nonlinear partial differential equations (9-10) under the corresponding boundary conditions (11) are solved numerically using an implicit tri-diagonal finite-difference method (Cebeci and Bradshaw, 1984; Keller, 1988). In this method, any quantity g at point (χ_n, η_j) is written as g_j^n. Quantities at the midpoints of grid segments are approximated to second order as:

$$g_j^{n-1/2} = \frac{1}{2}\left(g_j^n + g_j^{n-1}\right)$$
$$g_{j-1/2}^n = \frac{1}{2}\left(g_j^n + g_{j-1}^n\right) \tag{15}$$

And the derivatives are approximated to second order as

$$\left(\frac{\partial g}{\partial\chi}\right)_j^{n-1/2} = k_n^{-1}\left(g_j^n - g_j^{n-1}\right)$$
$$(g')_{j-1/2}^n = h_j^{-1}\left(g_j^n - g_{j-1}^n\right) \tag{16}$$

Where g is any dependent variable and n and j are the node locations along χ and η directions, respectively. First the second order partial differential equation is converted in a first order by substitutions f'=s, the difference equations that are to approximate the previous equations are obtained by averaging about the midpoint (χ_n, $\eta_{j-1/2}$), and those to approximate the resulting equations by averaging about ($\chi_{n-1/2}$, $\eta_{j-1/2}$). At each line of constant χ, a system of algebraic equations is obtained. With the nonlinear terms evaluated at the previous iteration, the algebraic equations are solved iteratively. The same process is repeated for the next value of χ, and the problem is solved line by line until the desired χ value is reached. A convergence criterion based on the relative difference between the current and the previous iterations is employed. When this difference reaches 10^{-5}, the solution is assumed to have converged and the iterative process is terminated

5. Results and Discussion

The viscous heating effects, Joule heating effects and cone half angle are studied on the mixed convection heat transfer over a vertical cone embedded in a saturated porous medium.

Figure 2. Shows the dimensionless velocity and temperature profiles for various values of m. It is found that increasing the cone angle parameter m was decreased and the velocity increased heat transfer rates inside the boundary layer. This is due to change of the flow toward stagnation point flow heat transfer problem.

Figure 3. shows the dimensionless velocity and temperature profiles for various values of magnetic field parameter H. It is found that the increasing of the magnetic field strength decreased the velocity and the heat transfer rates. The magneto effect on this problem is found to retard the motion of the fluid and to heat it at the same time. Figure 4. shows the effect of the viscous dissipation on the dimensionless velocity and temperature profiles, where increasing the effect of the viscous dissipation parameter increased the velocity and decreased the heat transfer rates inside the boundary layerdue to increasing the effect of the buoyancy force and excessive heating of flow.

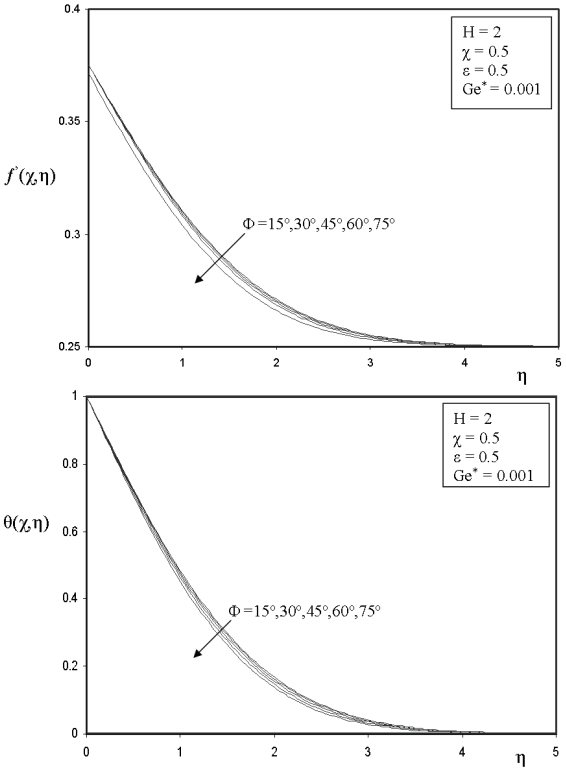

Fig. 2 Dimensionless velocity and temperature profiles at selected values of Φ

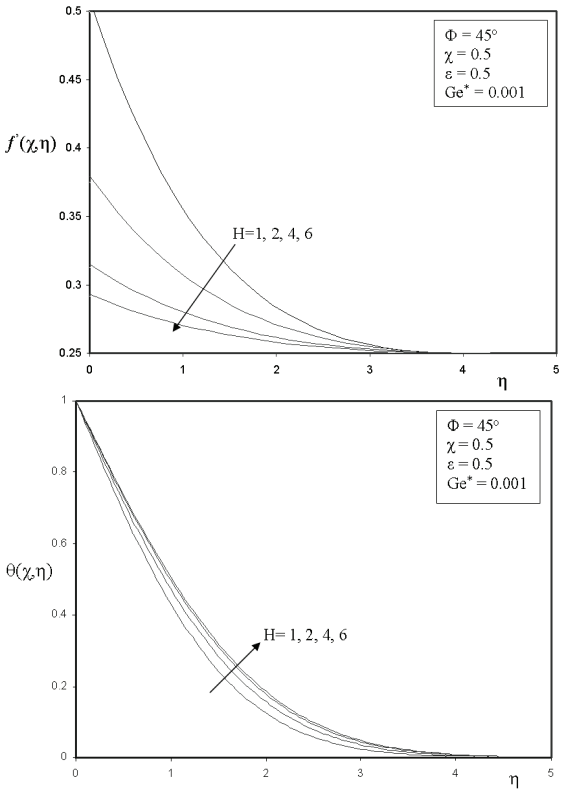

Fig. 3 Dimensionless velocity and temperature profiles at selected values of H

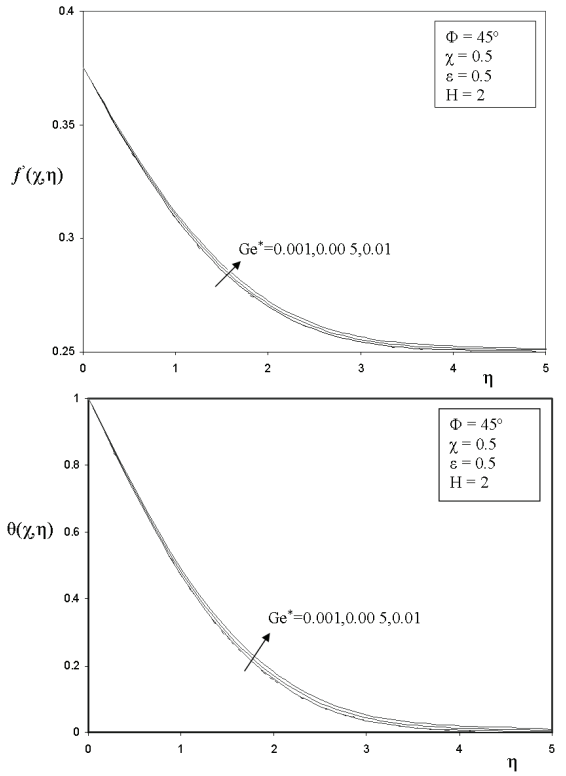

Fig. 4 Dimensionless velocity and temperature profiles at selected values of Ge*

Figure 5. shows that increasing the cone angle had increased the local Nusselt numbers. Fig. 6 shows the effect of Joule heating on the local Nusselt numbers. This behavior is due to heating the fluid and increasing the velocity inside the boundary layer. In addition, figure .7 shows the effect of modified Gebhart number of? viscous dissipation effects on the local Nusselt numbers. As shown, the increasing of the viscous parameter affects the forced flow more than free flow, and decreased the local Nusselt number and local coefficient of friction.

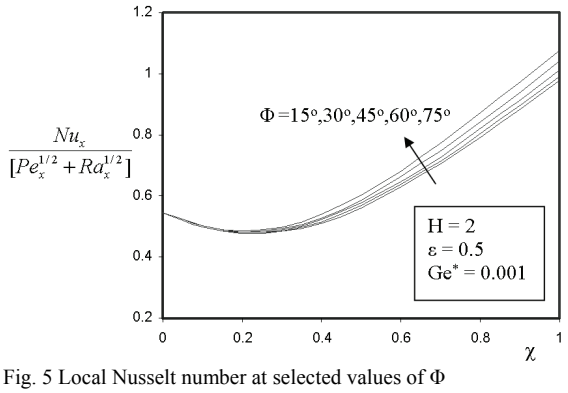

Fig. 5 Local Nusselt number at selected values of Φ

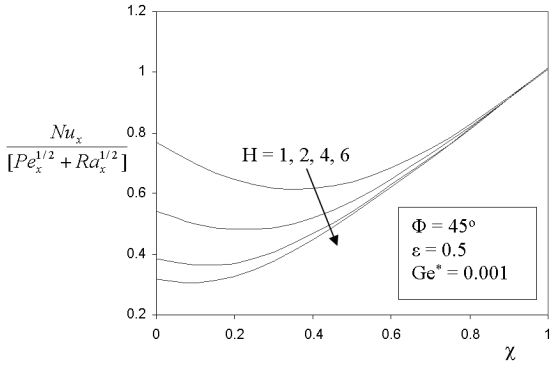

Fig. 6 Local Nusselt number at selected values of H

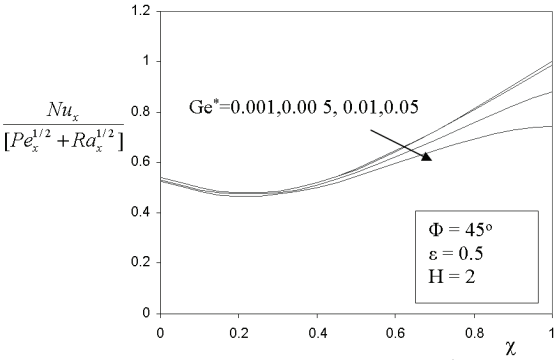

Fig. 7 Local Nusselt number at selected values of Ge^*

Table 1. shows the comparison between the $Nu_x/[Pe_x^{1/2}+Ra_x^{1/2}]$ calculated by the present method and that of the Yih (2001). For various values χ, with m=0.4241237, H=1. Iit is seen that the present results are in agreement with those obtained by Yih (2001).

Table 1. Comparison between the $Nu_x/[Pe_x^{1/2}+Ra_x^{1/2}]$ calculated by the present method and that of Yih (2001) for the case of, m=0.4241237, H=1

χ,	Present method	Yih (2001)
0	0.7683	0.7686
0.1	0.6990	0.6997
0.2	0.6488	0.6496
0.3	0.6222	0.6228
0.4	0.6218	0.6222
0.5	0.6478	0.6480
0.6	0.6974	0.6975
0.7	0.7659	0.7661
0.8	0.8487	0.8491
0.9	0.9417	0.9427
1	1.0423	1.0440

6. Conclusions

The MHD-mixed convection heat transfer problem is analyzed with viscous dissipation and Joule heating effects included in the energy equation. It is found that increasing the magnetic field strength or the joule heating effect had decreased the heat transfer rates from the surface of the vertical cone. The increasing of the cone angle parameter m enhances the heat transfer rates. Including the viscous dissipation effect in the energy equation was found to decrease the heat transfer rates.

References

[1] Aldoss, T. K., Al-Namir, M. A., Jarrah, M. A., and Al-Shaher, B. J, , "Magnetohydrodynamic mixed convection from a vertical plate embedded in a porous medium", Numerical Heat Transfer, Part A, Vol. 28, 1995, 635-645.

[2] Duwairi, H. M., Aldoss, T. K. and Jarrah, M. A., , "Nonsimilarity Solutions For Non-Darcy Mixed Convection From Horizontal Surfaces In A Porous Medium", Heat and Mass Transfer Journal, Vol. 33, 1997, 149-156.

[3] Duwairi, H. M. and Damseh, Rebhi A., "Magnetohydrodynamic Natural Convection Heat Transfer From Radiate Vertical Porous Surfaces", Heat and Mass Transfer, Vol.40, 2004, 787-792.

[4] Duwairi, H. M. and Damseh, Rebhi. A., "MHD-Buoyancy Aiding And Opposing Flows With Viscous Dissipation Effects From Radiate Vertical Surfaces", The Canadian Journal of Chemical Engineering, Vol. 823, 2004, 613-619.

[5] Duwairi, H. M. and Duwairi, R. M, , "MHD-Natural convection Heat Transfer in Unsteady Couette Flow of Gray fluids", In. J. Heat and Technology, Vol. 22, 2004, 103-107.

[6] Duwairi, H. M. and Alaraj, S,"MHD-Mixed Convection Along Radiant Vertical Cylinder", Int. Conf, of Thermal Engineering: Theory and Application, Lebanon, 2004.

[7] Duwairi, H. M, "Nonsimilarity MHD-Forced Convection Heat Transfer From Radiate Porous Constant Heat Flux Surfaces", Int. Conf. of Thermal Engineering: Theory and Application, Lebanon, 2004.

[8] Sparrow, E. M. and Cess, R. D, ," Effect of Magnetic Field on Free Convection Heat Transfer", Int. J. Heat Mass Transfer, Vol. 3, 1961, 267-274.

[9] Raptis, A. and Singh, A. K,"MHD Free Convection Flow Past an Accelerated Vertical Plate", Int. Commun. Heat Mass Transfer, Vol. 10, 1983, 313-321.

[10] Merk, H. J. and Prins, J. A, "Thermal convection in laminar boundary layer", Applied Scientific Research, Part A, Vol. 4, 1953.

[11] Hering, R. G. and Grosh, R. J, , "Laminar free convection from a non-isothermal cone", International Journal Heat Mass Transfer, Vol. 5, 1962, 1059-1068.

[12] Hering, R. G, , "Laminar free convection from a non-isothermal cone at low Prandtl numbers", International Journal Heat Mass Transfer, Vol.8, 1965, 1333-1377.

[13] Roy, S., "Free convection from a vertical cone at high Prandtl numbers", ASME J. Heat Transfer, Vol. 96, 1974, 115-117.

[14] Pop, I. and Takhar, H. S., , "Compressibility effects in laminar free convection from a vertical cone", Applied Scientific Research, Vol. 48, 1991, 71-82.

[15] Hossain, M. A. and Paul, S. C.,"Free convection from a vertical permeable circular cone with non-uniform surface temperature", Acta Mechanica, Vol. 151, 2001, 103-114.

[16] Watanabe, T., "Free convection boundary layer flow with uniform suction or injection over a cone", Acta Mechanica, Vol.87, 1991, 1-9.

[17] Wang, T. T., ," "General analysis of thermal convection heat transfer on a vertical cone",Journal of the Chinese Society of Mechanical Engineering, Vol. 12, 1991, 227-232.

[18] Wang, T., Kleinstreuer, C. and Chiang, H.,"Mixed convection from a rotating cone with variable surface temperature", Numerical Heat Transfer, Part A, Vol. 25, 1994, 75-83.

[19] Yih, K. A., ,"Radiation effect on mixed convection over an isothermal cone in porous media", Heat and Mass Transfer, Vol. 37, 2001, 53-57.

[20] Duwairi, H. M. and Al-Kabalwi, Y., "MHD-Conjugate mixed convection heat transfer over a vertical hollow cylinder embedded in a porous medium", International Journal. Heat and Technology, in press.

[21] Hess, JL. and Faulkner, S., ," Accurate values of the exponent governing potential flow about semi-infinite cone", AIAA J, Vol. 3, 1965, 767.

[22] Cebeci, T. and Bradshaw, P., "Physical and Computational Aspects of Convective Heat Transfer", Springer, New York. 1984.

[23] Keller, H. B., "Numerical Methods in Boundary Layer Theory", Annual Review of Fluid Mechanics, Vol. 10, 1988, 793-796.

المملكة الأردنية الهاشمية

الجامعة الهاشمية

المجلة الأردنية
للهندسة الميكانيكية والصناعية

JJMIE

مجلة علمية عالمية محكمة

http://jjmie.hu.edu.jo/

ISSN 1995-6665

المجلة الأردنية للهندسة الميكانيكية والصناعية

مجلة علمية عالمية محكمة

المجلة الأردنية للهندسة الميكانيكية والصناعية: مجلة علمية عالمية محكمة أسستها اللجنة العليا للبحث العلمي، وزارة التعليم العالي والبحث العلمي، الأردن، وتصدر عن عمادة البحث العلمي والدراسات العليا، الجامعة الهاشمية، الزرقاء، الأردن.

ترسل البحوث إلى العنوان التالي:

رئيس تحرير المجلة الأردنية للهندسة الميكانيكية والصناعية

عمادة البحث العلمي والدراسات العليا

الجامعة الهاشمية

الزرقاء - الأردن

هاتف : 3903333 5 00962 فرعي 4147

Email: jjmie@hu.edu.jo

Website: www.jjmie.hu.edu.jo